

**MITRAL VALVE FORCE BALANCE: A QUANTITATIVE  
ASSESSMENT OF ANNULAR AND SUBVALVULAR FORCES**

A Dissertation  
Presented to  
The Academic Faculty

by

Andrew W. Siefert

In Partial Fulfillment  
of the Requirements for the Degree  
Doctor in Philosophy in the  
School of Bioengineering

Georgia Institute of Technology  
May 2014

**COPYRIGHT © 2014 BY ANDREW W. SIEFERT**

**MITRAL VALVE FORCE BALANCE: A QUANTITATIVE  
ASSESSMENT OF ANNULAR AND SUBVALVULAR FORCES**

Approved by:

Dr. Ajit P. Yoganathan, Advisor  
Department of Biomedical Engineering  
*Georgia Institute of Technology*

Dr. Rudolph "Rudy" Gleason  
Department of Biomedical Engineering  
*Georgia Institute of Technology*

Dr. Joseph H. Gorman, III  
School of Medicine  
*University of Pennsylvania*

Dr. Steven F. Bolling  
Department of Cardiac Surgery  
*University of Michigan*

Dr. J. Brandon Dixon  
Department of Mechanical Engineering  
*Georgia Institute of Technology*

Dr. Sten L. Nielsen  
Aarhus University Hospital  
*University of Aarhus*

Date Approved: April 1, 2014

For Hard Work, Dedication, Andrea, My Parents, Dillon, Stan, Chris, Ian, and Sam

# TABLE OF CONTENTS

	Page
LIST OF TABLES	xi
LIST OF FIGURES	xv
LIST OF ABBREVIATIONS	xxii
SUMMARY	xxiii
 <u>CHAPTER</u>	
1 INTRODUCTION	1
2 BACKGROUND	5
2.1 Mitral Valve Structure and Function	5
2.1.1 The Mitral Annulus	6
2.1.2 The Mitral Leaflets	8
2.1.3 Mitral Valve Suspension System	9
2.1.4 The Mitral Valve's Intimate Relationship	12
2.2 Ischemic Mitral Regurgitation	13
2.2.1 Geometric and Functional Effects of an Inferior Left Ventricular Infarction	14
2.2.2 Current Trends and Operative Strategies for Ischemic Mitral Regurgitation	15
2.3 Suboptimal Surgical Outcomes in Ischemic Mitral Regurgitation	19
2.3.1 Structural Failure of Minimally Invasive Devices	19
2.3.2 Annuloplasty Ring Dehiscence	19
2.3.3 Recurrent Mitral Regurgitation Following Undersized Mitral Annuloplasty	20

2.4	Recent Investigations Contributing to the Improvement of Suboptimal Surgical Outcomes in Ischemic Mitral Regurgitation	21
2.4.1.	What Forces May Act On Annular Based Mitral Valve Devices?	21
2.4.2.	What Causes Annuloplasty Ring Dehiscence?	23
2.4.3.	Can Repair Induced Mitral Leaflet Tethering be Predicted Preoperatively?	24
3	OBJECTIVE AND SPECIFIC AIMS	28
4	MATERIALS	32
4.1	Specific Aim 1 Materials	32
4.1.1	Mitral Annular Force Transducer	32
4.1.2	Mitral Annular Force Transducer Calibration Apparatus	33
4.1.3	Healthy and Ischemic Mitral Regurgitation Ovine Model	35
4.2	Specific Aim 2 Materials	35
4.2.1	Healthy Ovine Model	35
4.2.2	Mitral Annuloplasty Ring Stress Transducer	35
4.2.3	Mitral Annuloplasty Ring Suture Force Transducer	36
4.2.4	Commercially Available Mitral Annuloplasty Rings	37
4.3	Specific Aim 3 Materials	38
4.3.1	Healthy and Ischemic Mitral Regurgitation Ovine Model	38
4.3.2	Sonomicrometry Array Localization	38
4.3.3	Ovine Mitral Valves for <i>In Vitro</i> Simulation	39
4.3.4	Georgia Tech Left Heart Simulator	39
4.3.5	Chordae Tendineae Force Transducers	40
4.3.6.	Stereo-Photogrammetry	41
4.3.7	Echocardiography	43

5	METHODS	44
5.1	Specific Aim 1 Methods	44
5.1.1	Transducer Spring Element Design: Healthy Animals	44
5.1.2	Transducer Spring Element Design: Ischemic Mitral Regurgitation Animals	48
5.1.3	Transducer Function	50
5.1.4	Transducer Fabrication	51
5.1.5	Transducer Calibration	56
5.1.6	Assessing Transducer Accuracy and Precision	56
5.1.7	Assessing Measurement Errors	56
5.1.8	Experimental Protocol	57
5.1.9	Data Acquisition	59
5.1.10	Data Processing and Experimental Endpoints	59
5.1.11	Statistical Analysis	60
5.2	Specific Aim 2 Methods	60
5.2.1	Annuloplasty Ring Stress Transducer	60
5.2.1.1	Ring Stress Transducer Design	60
5.2.1.2	Ring Stress Transducer Fabrication	61
5.2.1.3	Experimental Protocol	66
5.2.1.4	Data Acquisition	68
5.2.1.5	Data Analysis and Experimental Endpoints	68
5.2.2	Annuloplasty Ring Suture Force Transducer	69
5.2.2.1	Suture Force Transducer Design	69
5.2.2.2	Suture Force Transducer Fabrication	71
5.2.2.3	Suture Force Transducer Calibration	74
5.2.2.4	Assessing Transducer Accuracy and Precision	74

5.2.2.5 Instrumenting the Annuloplasty Ring with the Suture Transducers	75
5.2.2.6 Experimental Protocol	76
5.2.2.7 Data Acquisition	78
5.2.2.8 Data Processing and Experimental Endpoints	78
5.3 Specific Aim 3 Methods	79
5.3.1 Assessing the Accuracy of the Georgia Tech Left Heart Simulator	79
5.3.1.1 Experimental Protocol	79
5.3.1.2 Mapping the Ovine Mitral Valve Geometry	80
5.3.1.3 <i>In Vitro</i> Experimental Protocol	81
5.3.1.4 Quantifying Anterior Leaflet Strain <i>In Vivo</i> and <i>In Vitro</i> .	83
5.3.1.5 Data Processing	84
5.3.1.6 Statistical Analysis and Experimental Endpoints	84
5.3.2 Evaluating the Effect of Undersized Annuloplasty on Subvalvular Tethering	84
5.3.2.1 Chordae Tendineae Selection and Instrumentation	84
5.3.2.2 Simulating Undersized Mitral Annuloplasty	85
5.3.2.3 Data Processing	87
5.3.2.4 Statistical Analysis and Experimental Endpoints	88
6 RESULTS	89
6.1 Introduction to the Results	89
6.2 Specific Aim 1 Results	89
6.2.1 Accuracy and Precision of the Calibration Apparatus	90
6.2.2 Transducer Calibration, Accuracy, and Precision	91

6.2.3 Effect of Loading on Transducer Measurement Arm Cross-Talk	92
6.2.4 Effect of Transmitral Flow on the Force Transducer Measurements	92
6.2.5 Animal and Left Heart Hemodynamic Characteristics	93
6.2.6 Cyclic Annular Force Characteristics	94
6.2.7 Change in Annular Forces with Increasing Afterload: Healthy Animals	96
6.2.8 Change in Annular Forces with Increasing Afterload: Ischemic Mitral Regurgitation Animals	99
6.2.9 Change in Annular Forces with Increasing Afterload: Healthy versus Ischemic Mitral Regurgitation Animals	100
6.2.10 Rate of Change of Force during Isovolumetric Contraction: Healthy versus Ischemic Mitral Regurgitation Animals	101
6.3 Specific Aim 2 Results	103
6.3.1 Annuloplasty Ring Stress Pilot Study	103
6.3.1.1 Animal Characteristics and Ring Transducer Implantation	103
6.3.1.2 Ring Stresses at Implantation	104
6.3.1.3 Ring Stresses throughout the Cardiac Cycle	105
6.3.2 Annuloplasty Ring Suture Forces	107
6.3.2.1 Transducer Calibration, Accuracy, and Precision	107
6.3.2.2 Baseline and Elevated Animal Characteristics	109
6.3.2.3 Cyclic Suture Force Characteristics	111
6.3.2.4 Effect of Ring-Annulus Sizing on Cyclic Suture Forces	112
6.3.2.5 Effect of Ring-Annulus Sizing and Suture Position on Cyclic Suture Forces	113
6.3.2.6 Variation of Suture Forces by Annuloplasty Ring Region	116



6.4 Specific Aim 3 Results	117
6.4.1 Part A: <i>In Vitro</i> Mitral Valve Simulator Mimics Systolic Valvular Function of Healthy and Chronic Ischemic Mitral Regurgitation Ovine Model	117
6.4.1.1 Animal Characteristics	117
6.4.1.2 A2-P2 Leaflet Coaptation	118
6.4.1.3 Mitral Regurgitation	119
6.4.1.4 Anterior Leaflet Mechanics	120
6.4.2 Part B: Effect of Annuloplasty on Subvalvular Tethering	121
6.4.2.1 Mitral Regurgitation	122
6.4.2.2 A2-P2 Leaflet Coaptation Length	122
6.4.2.3 Chordal Tethering from the Posteromedial Papillary Muscle	123
6.4.2.4 Chordal Tethering from the Anterolateral Papillary Muscle	125
6.4.2.5 Chordal Tethering Forces Summed by Papillary Muscle	125
7 DISCUSSION	127
7.1 Introduction to the Discussion	127
7.2 Specific Aim 1	128
7.2.1 Discussion	128
7.2.2 Clinical Implications	134
7.3 Specific Aim 2	135
7.3.1 Annuloplasty Ring Stress Transducer	135
7.3.2 Annuloplasty Ring Suture Forces	137
7.3.3 Clinical Implications	141
7.4 Specific Aim 3	142

7.4.1 Assessing the Accuracy of the In Vitro Mitral Valve Simulator	142
7.4.2 Effect of Ischemic Mitral Regurgitation and Annuloplasty on Chordal-Leaflet Tethering	145
7.4.3 Clinical Implications	150
8 CONCLUSIONS AND FUTURE WORK	152
8.1 Specific Aim 1	152
8.1.1 Conclusions	152
8.1.2 Future Work	153
8.2 Specific Aim 2	154
8.2.1 Conclusions	154
8.2.2 Future Work	154
8.3 Specific Aim 3	155
8.3.1 Conclusions	155
8.3.1.1 Part A	155
8.3.1.2 Part B	156
8.3.2 Future Work	156
9 FUNDING SOURCES	158
9.1 Acknowledgement of Funding Sources	158
APPENDIX A: Specific Aim 1 Data	160
APPENDIX B: Specific Aim 2 Data	165
APPENDIX C: Specific Aim 3 (Part A) Data	168
APPENDIX D: Specific Aim 3 (Part B) Data	172
APPENDIX E: Catalog of Thesis Data Storage	176
APPENDIX F: Catalog of Publication and Conference Data Storage	180
REFERENCES	186

## LIST OF TABLES

		Page
Table 4-1	Materials used for the manufacturing of the mitral annular force transducer.	33
Table 4-2	Materials used for the manufacturing of the ring stress transducer.	36
Table 4-3	Materials used to manufacture the mitral annuloplasty ring suture force transducers.	37
Table 5-1	Material properties of Somos 18420.	46
Table 5-2	Material properties of MicroFine Green Resin.	49
Table 6-1	Baseline characteristics of the ovine subjects.	94
Table 6-2	Characteristics of the ovine subjects at elevated levels of left ventricular pressure.	94
Table 6-3	Peak rate of change for septal-lateral and transverse forces during isovolumetric contraction for the control and chronic IMR animals, significance is reported to the baseline values at 90 mmHg peak LVP within each group and direction: * p<0.01, † p<0.005, and ‡ p<.001.	102
Table 6-4	10-cycle ensemble averaged stresses at each annuloplasty ring location and direction expressed as a mean ± 1 standard deviation in MPa (positive values indicate tension while negative values indicate compression).	107
Table 6-5	Baseline characteristics of the healthy ovine animals.	110
Table 6-6	Characteristics of the ovine subjects at elevated levels of left ventricular pressure.	111
Table 6-7	Average percent increase in cyclic suture forces with an undersized ring.	115
Table 6-8	Baseline characteristics of the ovine subjects; Note mitral annular area was measured at peak left ventricular pressure.	117
Table 6-9	A2-P2 coaptation characteristics between the animal and simulated valves; * denotes a p<0.05 significant difference between the chronic IMR and control conditions simulated in vitro.	119

Table 6-10	Normalized strain rate ( $d(\epsilon)/d(LVP)$ ); * denotes a $p < 0.05$ and † denotes a $p < 0.01$ significant difference between the chronic IMR and control simulated conditions.	121
Table 6-11	Effect of the evaluated conditions on mitral regurgitation volume (MRV) and A2-P2 coaptation length (CL); asterisks (*) and dagger (†) denote significant differences of $p < 0.001$ relative to the healthy control condition and ischemic mitral regurgitation condition, respectively.	122
Table 6-12	Effect of the evaluated conditions on anterior strut (AS) and posterior intermediary (PI) chordal forces [N] (mean $\pm$ standard error) originating from the posteromedial (PM) and anterolateral (AL) papillary muscles; asterisks (*) and dagger (†) denote significant differences ( $p < 0.05$ ) relative to the healthy control condition and ischemic mitral regurgitation condition, respectively.	123
Table 6-13	Effect of the evaluated conditions on strut and intermediary chordal forces [N] summed by papillary muscle; asterisks (*) and dagger (†) denote significant differences ( $p < 0.05$ ) relative to the healthy control condition and ischemic mitral regurgitation condition, respectively.	126
Table A-1	Septal-lateral forces [N] for each of the healthy animals at each target level of peak left ventricular pressure.	160
Table A-2	Septal-lateral force rate [N/s] during isovolumetric contraction for each of the healthy animals at each target level of peak left ventricular pressure.	160
Table A-3	Transverse forces [N] for each of the healthy animals at each target level of peak left ventricular pressure.	161
Table A-4	Transverse force rate [N/s] during isovolumetric contraction for each of the healthy animals at each target level of peak left ventricular pressure.	161
Table A-5	Mean left ventricular pressure for each of the healthy animals at each target level of peak left ventricular pressure.	161
Table A-6	Mean heart rate for each of the healthy animals at each target level of peak left ventricular pressure.	162
Table A-7	Septal-lateral forces [N] for each of the IMR animals at each target level of peak left ventricular pressure.	162

Table A-8	Septal-lateral force rate [N/s] during isovolumetric contraction for each of the IMR animals at each target level of peak left ventricular pressure.	162
Table A-9	Transverse forces [N] for each of the IMR animals at each target level of peak left ventricular pressure.	163
Table A-10	Transverse force rate [N/s] during isovolumetric contraction for each of the IMR animals at each target level of peak left ventricular pressure.	163
Table A-11	Mean LVP for each of the IMR animals at each target level of peak left ventricular pressure.	163
Table A-12	Mean heart rate for each of the IMR animals at each target level of peak left ventricular pressure.	164
Table B-1	Baseline characteristics of the healthy ovine animals.	165
Table B-2	Mean left ventricular pressure and heart rate for 10 consecutive cardiac cycles at the target left ventricular pressure for the healthy ovine animals.	165
Table B-3	Mean suture forces [N] measured for cardiac cycles reaching a peak left ventricular pressure of 100 mmHg.	166
Table B-4	Mean suture forces [N] measured for cardiac cycles reaching a peak left ventricular pressure of 125 mmHg.	166
Table B-5	Mean suture forces [N] measured for cardiac cycles reaching a peak left ventricular pressure of 150 mmHg.	167
Table C-1	Healthy animal characteristics.	168
Table C-2	Healthy Animal A2-P2 leaflet coaptation characteristics.	168
Table C-3	Healthy Animal Anterior A2 Leaflet Strain and Strain Rate Normalized by $d(LVP)/dt$ in the radial and circumferential leaflet directions.	169
Table C-4	Ischemic mitral regurgitation animal characteristics.	169
Table C-5	Ischemic Mitral Regurgitation Animal A2-P2 leaflet coaptation characteristics.	169
Table C-6	Ischemic Mitral Regurgitation Animal Anterior A2 Leaflet Strain and Strain Rate Normalized by $d(LVP)/dt$ in the radial and circumferential leaflet directions.	170

Table C-7	Results of simulating healthy animal mitral valve geometry: A2-P2 leaflet coaptation characteristics.	170
Table C-8	Results of simulating healthy animal mitral valve geometry: Anterior A2 Leaflet Strain and Strain Rate Normalized by $d(LVP)/dt$ in the radial and circumferential leaflet directions.	170
Table C-9	Results of simulating ischemic mitral regurgitation animal mitral valve geometry: A2-P2 leaflet coaptation characteristics.	171
Table C-10	Results of simulating ischemic mitral regurgitation animal mitral valve geometry: Anterior A2 Leaflet Strain and Strain Rate Normalized by $d(LVP)/dt$ in the radial and circumferential leaflet directions.	171
Table D-1	Mitral regurgitation [mL] for each of the experiments and conditions.	172
Table D-2	Coaptation length [cm] for each of the experiments and conditions.	173
Table D-3	Cyclic force [N] for the anterior leaflet strut chord originating from the posteromedial papillary muscle for each of the experiments and conditions.	173
Table D-4	Cyclic force [N] for the posterior leaflet intermediary chord originating from the posteromedial papillary muscle for each of the experiments and conditions.	174
Table D-5	Cyclic force [N] for the anterior leaflet strut chord originating from the anterolateral papillary muscle for each of the experiments and conditions.	174
Table D-6	Cyclic force [N] for the posterior leaflet intermediary chord originating from the anterolateral papillary muscle for each of the experiments and conditions.	175

## LIST OF FIGURES

		Page
Figure 2-1	Left: Anatomic representation of the mitral valve and left ventricle (modified from [1]); Right: En-face view of the mitral leaflets with anatomical nomenclature (modified from [1]).	5
Figure 2-2	Left: Schematic representation of the relative location of the mitral annulus (modified from [39]); Right: Representative image of the mitral annular saddle shape that occurs during ventricular contraction (modified from [40]).	7
Figure 2-3	Rough, clear, and basal leaflet zones of the anterior and posterior mitral leaflets (modified from [39]).	9
Figure 2-4	Morphologic classification of papillary muscle type (modified from [1]).	10
Figure 2-5	An excised mitral valve with the types and locations of the chordae tendineae identified.	11
Figure 2-6	Thinning and remodeling of post-infarction LV result in papillary muscle displacement and annular dilatation that is characteristic of an inferior myocardial infarction and mitral regurgitation (modified from [56]).	13
Figure 2-7	Example of an asymmetrically directed regurgitation jet from an inferior left ventricular infarction.	15
Figure 2-8	Undersized mitral valve annuloplasty (modified from [1]).	16
Figure 2-9	Left: Mitral valve replacement using a bileaflet mechanical heart valve; Right: Mitral valve replacement using a bovine pericardium valve (modified from [117]).	17
Figure 2-10	Examples of different percutaneous MV devices that include (A) the Monarc device for indirect annuloplasty, (B) the Mitralign device for direct annuloplasty, (C) the CardiAQ prosthesis for MV replacement, and (D) the Mitraclip for edge-to-edge leaflet approximation (images modified from [7]).	18
Figure 2-11	Annuloplasty ring dehiscence echocardiographic images.	20

Figure 2-12	(A) Normal mitral valve geometry; (B) Illustration of the annular dilatation and leaflet tethering associated with ischemic mitral regurgitation; (C) With a severely dilated left ventricle, undersized mitral annuloplasty results in a mono-leaflet valve and exacerbation of posterior leaflet tethering.	21
Figure 2-13	Left: Majority of experimental studies have sought to quantify the forces acting in-plane with the mitral valve annulus; Center: Hasenkam et al. [75] adhered strain gage rosettes to Edwards-Duromedics mitral valves to quantify planar forces; Right: Shandas et al. [76] used 2D deformations of stented prosthetic MVs measured by echo as boundary conditions in a finite element model.	22
Figure 2-14	Left: Ring pull out test experimental set-up; Right: Results of the tests for the indicated annuloplasty rings and ring suturing procedure where minor and major decrease correspond to momentary drops in force during the tensile test which correspond to select ring sutures failing (modified from [78]).	24
Figure 2-15	Example progression of data flow for patient-specific surgical planning using in silico modeling.	26
Figure 2-16	Images from recently published in silico mitral valve models showing the simplifications in modeling the complex chordae tendineae (images modified from [98, 97, 102]).	26
Figure 4-1	Bi-axial calibration apparatus with a schematic representation of what forces are applied to the device, forces are applied via a spring-piston system such that spring compression elicits a force on the transducer.	34
Figure 4-2	A. Acrylic housing, B. Bolt, C. Piston, D. Precision compression spring, E. Pusher which is in contact with the force transducer.	34
Figure 4-3	Sonocrystal array localization for a chronic IMR animal to (Left) the mitral annulus and leaflets and (Right) the papillary muscles.	38
Figure 4-4	Schematic of the Georgia Tech Left Heart Simulator with components identified.	40
Figure 4-5	Left: Chordal force transducer, Right: Attachment to the chordae to the strut and intermediary chordae of a mitral valve mounted to the mitral annulus as viewed from the apical aspect.	41
Figure 4-6	Central A2 cusp of the anterior leaflet is marked with tissue dye then tracked throughout the cardiac cycle to quantify anterior leaflet strain.	42



Figure 5-1	Left: Spring element of the designed annular force transducer with selected highlights: (A) through holes for suturing the device to the mitral valve annulus, (B) anterior transducer arm, (C) central bridge area designed to both minimize transmitral blood flow obstruction and provide structural support, (D) location of strain gage to measure transverse force, (E) location of strain gage to measure anterolateral force, and (F) lateral transducer arm, (G) anterior commissure measurement arm, and (H) posterior commissure measurement arm; Right: Orientation of mitral valve with respect to the orientation of the transducer.	45
Figure 5-2	Left: Top-view of the transducer with a load of 13.9 N placed in the anterolateral and transverse directions with the color green indicating a peak strain of approximately 1.8%; Right: Bottom view depicting the same loading conditions.	47
Figure 5-3	Top-view of the acute animal spring element with dimensions noted.	47
Figure 5-4	Left: Plastic deformation of the transverse and lateral measurement arms; Right: out-of-plane plastic deformation occurring in the anterior and posterior commissural measurement arms.	48
Figure 5-5	Top-view of the chronic animal spring element with dimensions noted.	49
Figure 5-6	Left: Top-view of the chronic animal transducer spring element's FEA stress results when subjected to a 13.9 N force in the anterolateral and transverse directions as well as a 6 N force applied on the lateral measurement arm towards the anterior commissure arm; Right: Bottom-view of the same deformation; deformation scales are increased to display displaced positions.	50
Figure 5-7	Left: The strain gage is trimmed to dimensions just outside the grid area allowing the gage to fit of each of the spring element's measurement sections; Center: PCT-2M Gage Installation tape is laid over the gage and peeled upwards removing the gage from the cutting surface; Right: Strain gages adhered to the anterior measurement arm.	52
Figure 5-8	Left: top view of the transducer with wires harnessed to the geometry's surface using 3-0 suture; Right: isometric view of the transducer after wires have been connected and harnessed.	54
Figure 5-9	Left: Strain gage coated with epoxy (Step 9); Center: strain gages coated with nitrile rubber (Step 10); Right: application of 3145 silicone with the measurement arm cushions in place (Step 12).	55

Figure 5-10	Transducer implanted in the mitral annulus of a healthy ovine animal.	58
Figure 5-11	Anatomical directions and relative dimensions of the annuloplasty ring stress transducer's titanium core.	61
Figure 5-12	Image of the strain gages and lead wire terminal ready for strain gage positioning.	62
Figure 5-13	(A) Anatomical directions, (B) Image of the titanium annuloplasty ring core with bonded strain gages and lead wire terminals tinned, and (C) Planar orientation of the mounted strain gages with labels indicating their measurement direction.	64
Figure 5-14	Left: Half-bridge configuration with strain gage, lead wire terminal, and wires shown (Note: Blue wire is actually white on the actual transducer); Right: Wired half-bridges.	65
Figure 5-15	Left: Transducer's strain gages and lead wire terminals are coated in Loctite® M-31CL™ Hysol® Medical Device Epoxy (Step 11); Right: Following harnessing the transducer's wires (Step 12) , the entire transducer is dip-coated in synthetic rubber (Step 13).	65
Figure 5-16	A. Ten 2-0 sutures are placed through the suture cuff of the annuloplasty ring transducer for implantation, B. While on cardiopulmonary bypass the transducer is implanted to the mitral annulus, C. Post-experimentation, the left atrium is removed and the transducer was inspected for firm anchoring to the mitral annulus.	68
Figure 5-17	(A) Schematic of transducer with (a) mounting holes for ring mounting, (b) mattress suture passages, (c) strain gage for force measurement, and (d) exiting wires. (B) Completed transducer. (C) Schematic of implanted ring with suture induced transducer deformation and force measurement. (D) Device implantation. (E) Implanted transducer imaged using fluoroscopy.	70
Figure 5-18	Left: Strain gage alignment (Strain gage is not adhered to the surface of the transducer spring element); Right: Strain gage is adhered to the spring element.	72
Figure 5-19	Tinned solder nodes on a strain gage; Center: Wired strain gage; Right: Strain gage surface coating with epoxy.	73
Figure 5-20	Method used to secure a suture transducer to the annuloplasty ring.	76
Figure 5-21	Photograph of a size 24 Physio™ ring instrumented with 10 suture force transducers.	76

Figure 5-22	Left: Geometric map of sonomicrometry crystals localized to the A2 anterior leaflet and mitral annulus; AC: Anterior Commissure, PC: Posterior Commissure; Right: in-vivo image of crystals localized to the mitral annulus and anterior leaflet with directions of strain shown (See Figure 4-3 for crystals localized to the papillary muscles).	80
Figure 5-23	A. Schematic representation of the surgeon's view of the mitral valve with the A2-P2 echocardiography measurements of leaflet coaptation identified; B. Direct linear transformation was used to calculate the radial and circumferential anterior leaflet strain using two high-speed cameras tracking nine fiduciary leaflet markers.	83
Figure 5-24	Schematic representation of securing a chordal force transducer to a selected chordae tendineae.	85
Figure 5-25	Summary of experimental conditions progressing from control to ischemic mitral regurgitation (IMR), oversized mitral annuloplasty, true-sized mitral annuloplasty, and undersized mitral annuloplasty (UMA). (Please note images are not drawn to scale).	87
Figure 6-1	Left: Mean force of 10 independent trials with a 95% confidence interval half-rotation bolt increments; Right: Table displaying the values and intervals at each bolt rotation.	91
Figure 6-2	Comparison of measured to true forces for the septal-lateral direction of a representative calibrated transducer.	92
Figure 6-3	A. 3D Doppler echocardiographic image of the transducer mounted within the Georgia Tech Left Heart Simulator's static mitral annulus; B. 2D Doppler echocardiographic image of the transducer (FT) within the sheep subject, the left ventricle (LV), left atrium (LA), and mitral valve (MV) are labeled; C: Transducer within the simulator displaying similar flow patterns and magnitudes to that experienced in-vivo.	93
Figure 6-4	Representative unfiltered forces from both a control (top) and chronic IMR (bottom) animal are plotted with time and LVP	95
Figure 6-5	A. Doppler echocardiographic image of mitral inflow from the Left Atrium (LA) to the Left Ventricle (LV) in absence of the annular Force Transducer (FT); B. Implanted transducer increases mitral inflow velocity.	96
Figure 6-6	The mean change in septal-lateral force throughout the cardiac cycle increased significantly from baseline to each level of peak left ventricular pressure.	97

Figure 6-7	The mean change in transverse force throughout the cardiac cycle increased significantly from baseline to each level of peak left ventricular pressure.	98
Figure 6-8	Comparison of each directional force at increasing levels of peak left ventricular pressure.	99
Figure 6-9	Top: The measured change in septal-lateral force throughout the cardiac cycle was observed to be significantly greater within the control animals at each level of peak left ventricular pressure; Bottom: No significant differences in the change in transverse force throughout the cardiac cycle was observed between the animal groups and left ventricular pressure levels.	101
Figure 6-10	A. Ten 2-0 sutures are placed through the suture cuff of the annuloplasty ring transducer for implantation, B. While on cardiopulmonary bypass the transducer is implanted to the mitral annulus, C. Post-experimentation, the left atrium is removed and the transducer was inspected for firm anchoring to the mitral annulus.	104
Figure 6-11	Annuloplasty ring stresses measured after implanting the ring to the mitral annulus in the flaccid cardioplegic heart (all stresses are expressed in MPa) with arrows indicating compression (arrows pointing towards the ring) or tension (arrows pointing away from the ring) at each measurement location.	105
Figure 6-12	Left: Two consecutive representative cardiac cycles of the apical-basal and planar ring stresses plotted with left ventricular pressure and electrocardiography; Right: pictorial representations of the ring with arrows indicating compressive stresses (arrows pointing towards the ring) or tensile stresses (arrows pointing away from the ring) at each measurement location at peak left ventricular pressure.	106
Figure 6-13	Representative calibration curves for the 10 suture force transducers attached to a size 24 Physio <sup>TM</sup> ring.	108
Figure 6-14	Representative comparison of measured to true forces for the transducers whose calibration curves are graphed in Figure 6-13.	109
Figure 6-15	Two representative cardiac cycles of measured suture forces with the corresponding left ventricular pressure trace.	112
Figure 6-16	Suture forces averaged by ring-annulus sizing.	113

Figure 6-17	Top: Undersized annuloplasty cyclic suture forces expressed as a mean $\pm$ 1 standard deviation for each ring position; Bottom: True-sized annuloplasty cyclic suture forces expressed as a mean $\pm$ 1 standard deviation for each ring position.	114
Figure 6-18	Suture forces by ring region and ring-annulus sizing at each level of left ventricular pressure.	116
Figure 6-19	Chordal forces from the posteromedial papillary muscle (PMPM) and anterolateral papillary muscle (ALPM) were normalized to the forces observed during the healthy control condition to demonstrate relative changes in cyclic chordal tethering with ischemic mitral regurgitation (IMR) and increasing degrees of annular under sizing.	124
Figure 7-1	Overall trends for force magnitude by suture position at an LVP of 125 mmHg.	138
Figure 7-2	Example iterative scheme for improving modeling of idealized chordal structures and geometry using the presented in vitro data.	147

## LIST OF ABBREVIATIONS

AHCWR	Annular-Height-to-Commissural-Width Ratio
ALPM	Anterolateral Papillary Muscle
CL	Coaptation Length
IMR	Ischemic Mitral Regurgitation
LV	Left Ventricle
MR	Mitral Regurgitation
MRV	Mitral Regurgitation Volume
MV	Mitral Valve
PM	Papillary Muscle
PMPM	Posteromedial Papillary Muscle
UMA	Undersized Mitral Annuloplasty

## SUMMARY

Ischemic mitral regurgitation (IMR) occurs when the heart's mitral valve is rendered incompetent by post-infarction left ventricular remodeling and three-dimensional alterations in mitral valve geometry. These alterations include papillary muscle displacement and annular dilatation, which ultimately lead to restricted leaflet motion and mitral regurgitation. While the severity of this disease can vary, IMR typically presents with significant comorbidities yielding the cessation of regurgitation as being necessary but not sufficient to improve patient outcomes. For these reasons among others, an optimal IMR surgical repair has yet to be established. Finding an optimal surgical strategy has included the development of novel implantable devices and techniques for both open-chest and percutaneous approaches. Despite published successes, post-operative device and repair induced complications have been documented. These include but are not limited to device fracture in pre-clinical trials, annuloplasty ring dehiscence, and post-operative chordal-leaflet tethering. From any of these adverse events recurrent regurgitation can ensue, leading to impaired left ventricular function, worsened patient health and mortality. A common thread to these outcomes is the presence or imbalance of mechanical forces acting on implanted devices, on annuloplasty ring mattress sutures, and in the mitral valve's chordae tendineae. Little or no knowledge exists for the magnitude of these forces or their variations with left heart function under healthy and IMR conditions. Understanding the relative magnitudes and variation of these forces will significantly aid in the development of more robust devices and contribute to improved knowledge of IMR surgical procedures and techniques. To this end, three specific aims were evaluated. In specific aim 1, a novel transducer was developed to measure the

radially directed forces that may act on devices implanted to the mitral annulus. In an ovine model, radial forces were found to statistically increase with left ventricular pressure and were reduced in the setting of IMR. In specific aim 2, the suture forces required to constrain true-sized and undersized annuloplasty rings to the mitral annulus of healthy ovine subjects was evaluated. Suture forces were observed to be larger on the anterior aspect of the rings and were elevated with annular undersizing. In specific aim 3, an *in vitro* simulator's ability to mimic healthy and IMR ovine mitral valve function was evaluated. After understanding the accuracy of the model, the *in vitro* IMR model was used to evaluate the progressive effects of annuloplasty undersizing on strut and intermediary chordal tethering. Compared to the IMR condition, increasing levels of undersizing annuloplasty significantly reduced regurgitation, increased coaptation, reduced posteromedial papillary muscle strut chordal forces, and reduced intermediary chordal forces from the anterolateral papillary muscle. Considered together, the generated data and knowledge will contribute to the development of more durable devices and techniques to assess the growing and significant clinical burden known as IMR.



# CHAPTER 1

## INTRODUCTION

From early anatomical studies we've learned the human heart consists of two pumps in series; with the right heart pumping blood to the lungs and the left ejecting blood to the systemic circulation. Both of these pumps consist of an atrium and ventricle and are separated by unique one-way valves. Separating the left atrium and ventricle is the mitral valve. The sole purpose of the mitral valve is simple. It aims to maintain unidirectional flow from the left atrium to the ventricle while preventing the backflow of blood during ventricular contraction. Despite its simple purpose, the anatomy that allows for its healthy function is complex.

The healthy function of the mitral valve is made possible by four anatomical structures known as the mitral annulus, leaflets, chordae tendineae, and papillary muscles. The mitral annulus is a discontinuous band of connective tissue lying in the fibrous junction and left ventricle of the heart [1,2]. Due to its unique location, left ventricular contraction decreases the mitral annular area and by extension the space for which the leaflets must occlude. Hinging at the annulus are the anterior and posterior leaflets. Although they differ in size and geometry, each leaflet occupies a similar surface area during leaflet closure [1]. The mitral leaflets interact with the left ventricle via the chordae tendineae and papillary muscles. These subvalvular structures aid in bringing the leaflets into apposition and providing cross-ventricular support [2]. Based on this anatomy, it is clear that the mitral valve is both structurally and functionally part of the

fibrous junction and left ventricle of the heart. For these reasons, alterations in any of these structures contribute to and affect valve function [2].

Changes in mitral valve function may be most notably manifested in ischemic mitral regurgitation. This disease is characterized by post-infarction left ventricular remodeling and three-dimensional alterations in mitral valve geometry. These geometric alterations include papillary muscle displacement and annular dilatation which ultimately lead to restricted leaflet motion and mitral regurgitation [2]. Recent studies estimate the prevalence of ischemic mitral regurgitation within the United States to be approximately 3 million patients [3]. Beyond its wide prevalence, post-myocardial infarction patients have been found to exhibit 1-year mortality rates of 52% with severe IMR, 22% for mild to moderate IMR, and 11% for no IMR [4].

While the severity of this disease can vary, ischemic mitral regurgitation typically presents with significant comorbidities yielding the cessation of regurgitation as being necessary but not sufficient to improve patient outcomes. For these reasons among others, an optimal surgical repair has yet to be established. The most common surgical strategies have included undersized mitral valve annuloplasty with a complete rigid ring and mitral valve replacement with and without coronary artery bypass grafting [5]. The routine use of these strategies however has been recently challenged by the growing number of patients who are elderly or present with significant comorbidities deemed too high-risk for these procedures [6]. This trend, paired with a rising desire for less invasive approaches, has led to the development of minimally invasive and percutaneous surgical techniques for ischemic mitral regurgitation [7]. While these techniques exhibit potential for treating a large number of patients, many challenges remain in demonstrating

equivalent or improved clinical therapeutic benefits compared to optimally performed mitral annuloplasty or valve replacement [8].

In seeking out an optimal ischemic mitral regurgitation surgical strategy, novel implantable devices for both open-chest and percutaneous approaches have been developed [4,7]. Despite published success, post-operative device and repair induced complications have been demonstrated. These include but are not limited to device fracture in pre-clinical trials [7,9,10], annuloplasty ring mattress suture dehiscence [11-22], and post-operative chordal-leaflet tethering [23-29]. From any of these adverse events recurrent mitral regurgitation can ensue, leading to impaired left ventricular function, worsened patient health and mortality [4]. A common thread to these outcomes is the presence or imbalance of mechanical forces acting on implanted devices, on mitral annular mattress sutures, and in the MV's chordae tendineae. At current, no knowledge exists for the magnitude of these forces or their variation with left heart function.

Understanding the relative magnitude and variation of these forces will significantly aid the development of more robust devices, improve knowledge for device implantation, and contribute to methods designed to predict or reduce postoperative chordal-leaflet tethering. The overall objective of the present research therefore is to determine the forces that exist at the mitral annular and subvalvular levels under normal, IMR, and repair conditions. This objective is assessed by three specific aims that include (i) Quantifying the contractile mitral annular forces that may contribute to device fracture, (ii) Quantify the suture forces required to constrain true-sized and undersized annuloplasty rings to the ovine mitral valve annulus, and (iii) Evaluate the effects of mitral valve annuloplasty on chordal-leaflet tethering forces.

To independently analyze the variables of interest, *in vitro* and *in vivo* animal experiments are conducted. This hybrid approach has a clear advantage over clinical based studies by independently controlling parameters that are of importance to mitral valve mechanics and function. These experiments will provide detailed quantitative information on function and mechanics in the normal, IMR and repaired mitral valve. Qualitative and quantitative information from these experiments may provide a basis or guide which may lead to improved knowledge and results for both open-chest and minimally invasive mitral valve interventions.

## CHAPTER 2

### BACKGROUND

#### 2.1 Mitral Valve Structure and Function

The mitral valve (MV) is a complex bileaflet valve lying between the heart's left atrium and left ventricle (LV). Its purpose is to maintain unidirectional flow from the atrium to the ventricle while preventing the backflow of blood (regurgitation) during ventricular ejection. This critical function is accomplished via four anatomical structures that include the mitral annulus, leaflets, chordae tendineae, and papillary muscles (Figure 2-1). The unique geometric arrangement of these structures within the left atrium, fibrous skeleton, and left ventricle of the heart facilitates healthy MV function.

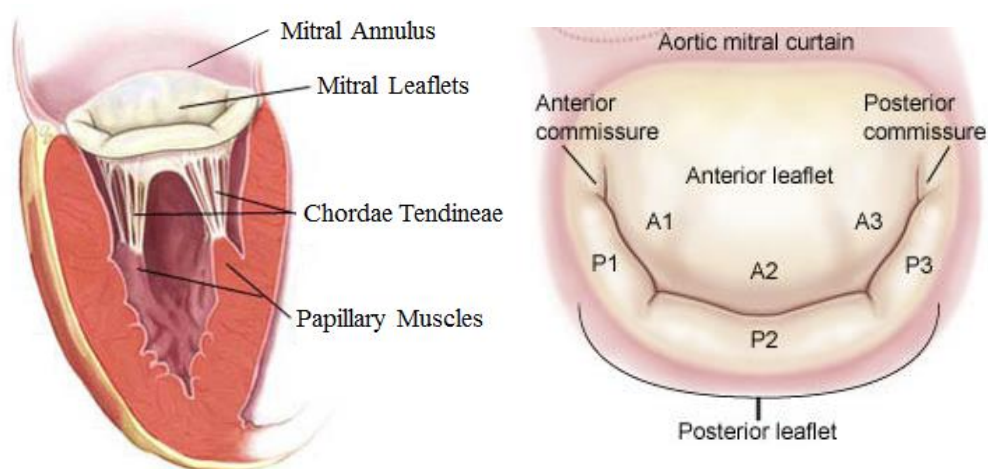


**Figure 2-1 Left: Anatomic representation of the mitral valve and left ventricle (modified from [1]); Right: En-face view of the mitral leaflets with anatomical nomenclature (modified from [1]).**

### **2.1.1 The Mitral Annulus**

Of the mitral valve's anatomical structures, the mitral annulus is a discontinuous band of connective tissue existing within the atrioventricular junction of the left heart. The annulus is not visible from the atrium and is deeper and 2 mm external to the hinge of the mitral leaflets (Figure 2-2) [1]. Due to the proximity of the annulus to the dynamic LV and aortic root, the shape and size of the mitral annulus changes throughout the cardiac cycle.

The three-dimensional shape of the mitral annulus changes throughout the cardiac cycle [30-37]. During ventricular diastole the annulus is approximately planar while during ventricular contraction the annulus conforms to the shape of a hyperbolic parabola or annular saddle [30-34]. Two complimenting theories have been proposed to explain the mechanism by which the annulus systolically conforms to the saddle-shaped geometry. In the first, unequal apical-basal translation of the mitral annulus during LV contraction (due to aortic root tethering) causes annular folding across the intercommissural axis [35]. In the second, expansion of the aortic root during systolic LV contraction displaces the anterior annulus laterally, which folds the anterior and lateral portions of the mitral annulus across the intercommissural axis [36,37].

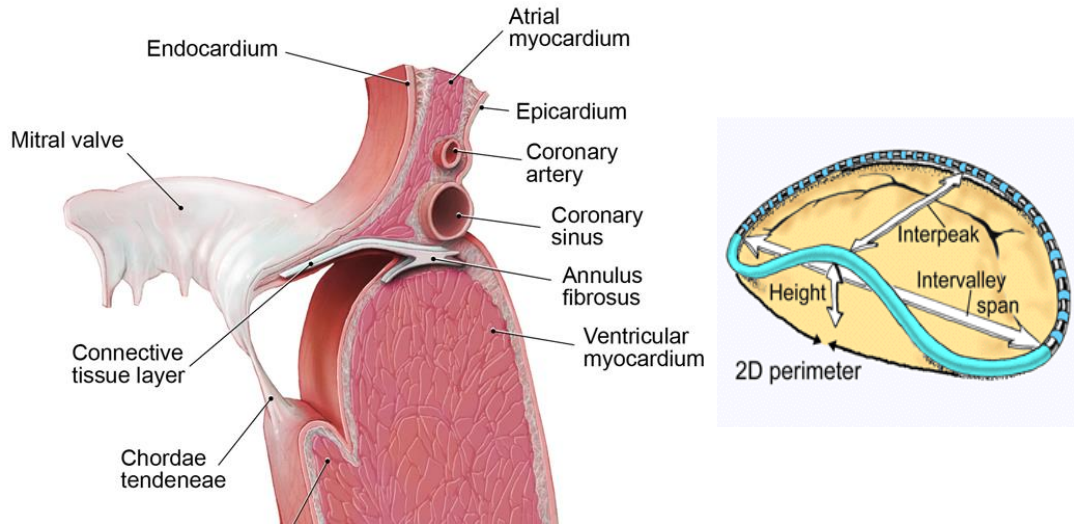


**Figure 2-2 Left: Schematic representation of the relative location of the mitral annulus (modified from [39]); Right: Representative image of the mitral annular saddle shape that occurs during ventricular contraction (modified from [40]).**

The shape of the annular saddle is quantified by measuring the annular height (perpendicular distance between the lowest (most apical) and highest (most basal) two points on the annulus) and by quantifying the Annular-Height-to-Commissural-Width-Ratio (AHCWR) (Figure 2-2). In reference to Figure 2-2, the AHCWR can be calculated by dividing the annular height by the intervalley span (commissural width). In healthy humans, the annular height has been demonstrated to range from 0.6 mm to 1.4 cm with an AHCWR approaching 20 to 30% [32,38]. In ovine animals, the AHCWR has been reported to range from 12 to 15% [33,41]. The presence of an annular saddle has been demonstrated to exhibit mechanical advantages to both the leaflets and chordae tendineae. Numerical and experimental studies have shown the presence of an annular saddle to reduce stress in the mitral leaflets and reduce tethering in the chordae tendineae [42-45].

In addition to conforming to the shape of a saddle, the mitral annulus reduces its effective orifice area during ventricular contraction. This action effectively decreases the area for which the mitral leaflets must occlude during leaflet closure. In healthy humans, the mitral annulus can systolically reduce its area and circumference by approximately  $26 \pm 3 \%$  and  $13 \pm 3 \%$  respectively [30]. In a healthy ovine model, the mitral annular area and circumference reduces by approximately 15% and 9% [46,47].

### **2.1.2 The Mitral Leaflets**

Hinging at the annulus are the anterior and posterior mitral leaflets (Figure 2-1 and 2-3). Although they differ in size and shape, with the anterior leaflet extending more radially and the posterior leaflet extending more circumferentially, each leaflet occupies a similar surface area of the valve [1]. The total surface area of both MV leaflets is approximately twice that of the MV orifice [1]. This geometric relationship provides redundancy during leaflet closure and in part provides a protective mechanism against mitral regurgitation.

When considered in isolation, both leaflets can be divided into three regions known as the base (closest to mitral annulus), belly (central) and free edge (distal to the mitral annulus) (Figure 2-3). Due to numerous chordal insertions, the free edge of the leaflets is thicker, has an irregular texture, and is identified as the rough zone. Conversely, the clear zone lies between the line of coaptation and the MA, has minimal CT attachment, is thin, regular in texture, and is approximately translucent.



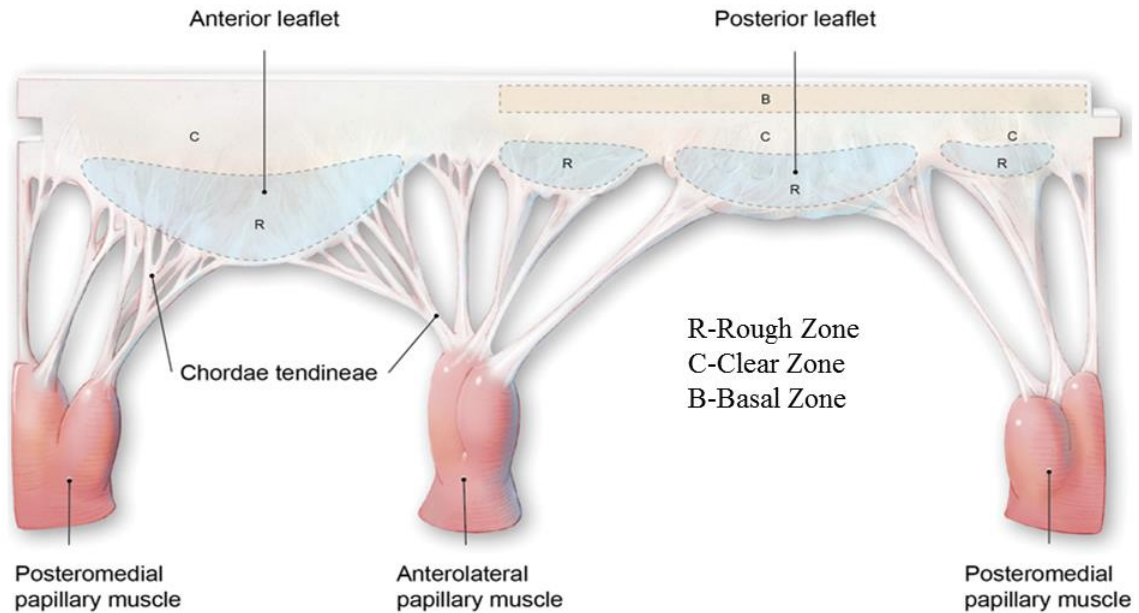


**Figure 2-3 Rough, clear, and basal leaflet zones of the anterior and posterior mitral leaflets (modified from [39]).**

Compared to the anterior leaflet, the posterior leaflet is deeply scalloped by two indentations. These indentations morphologically separate the posterior leaflet into 3 distinct sections and are sequentially numbered from the anterior to posterior commissural direction. These three posterior leaflet sections are known as the anterior (P1, smallest in size), middle (P2, largest in size) and posterior (P3) scallops. The regions of the anterior leaflet geometrically opposing the posterior leaflet are similarly denoted as A1, A2 and A3.

### **2.1.3 Mitral Valve Suspension System**

The leaflets communicate with the LV through the suspension system of the mitral valve. This system consists of two papillary muscles that extend upwards from the LV endocardium, with chordae tendineae fanning outwards from each papillary muscle tip to

the free edge, belly, and base of the mitral leaflets (Figure 2-1 and 2-3). Together, these structures perform the dual function of maintaining valvular competence and ventricular geometry by providing cross-ventricular support [2].

Two groups of papillary muscles are attached to the LV free wall and are identified based on their relative anatomical position (anterolateral and posteromedial). Morphological variability exists for papillary muscles which can be characterized into 5 distinct groups (Figure 2-4). These groups include (Type 1) single bulky head, (Type 2) multiple heads, (Type 3) narrow head, (Type 4) arch-shaped head, and (Type 5) short but wide head [1].

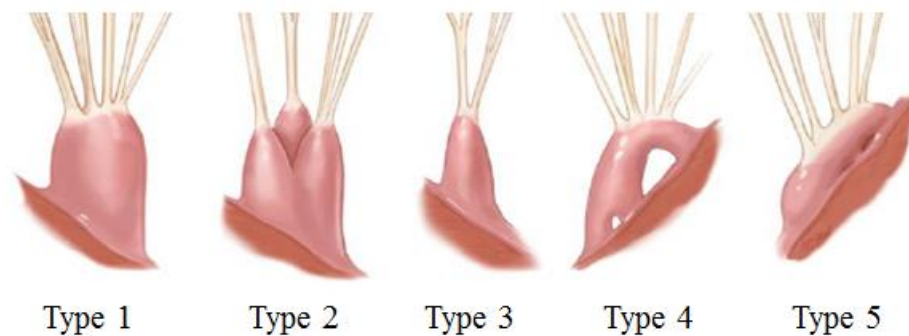


**Figure 2-4 Morphologic classification of papillary muscle type (modified from [1]).**

Given the papillary muscles are functional extensions of the LV; it is not surprising these structures exhibit contractile properties. The papillary muscles have been experimentally shown to shorten by as much as 2-5 mm during LV contraction [48,49]. Despite their downward contraction, the papillary muscle tips maintain a near constant distance with the annulus throughout the cardiac cycle [50]. This phenomenon is due to the systolic apical-basal shortening of the left ventricle which effectively maintains

the distance between the papillary muscles and LV base. Based on these dynamics, leading researchers have hypothesized the papillary muscles to act as mitral valve shock absorbers and aid in preventing leaflet prolapse throughout the cardiac cycle [50].

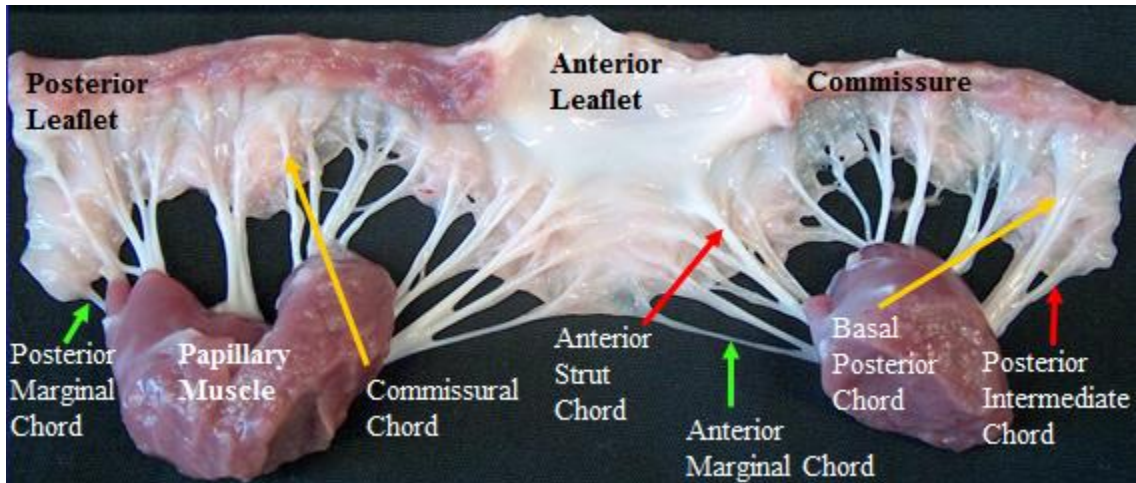


**Figure 2-5 An excised mitral valve with the types and locations of the chordae tendineae identified.**

Connecting the papillary muscles to the mitral leaflets is the chordae tendineae. In general, three types of chordae are recognized and are characterized by where and to which leaflet they attach (Figure 2-5) [51]. Primary (also referred to in literature as marginal) chordae are attached uniformly via bifurcations or trifurcations to the free edge of both the anterior and posterior leaflets. Two types of secondary chordae exist. Anterior strut chordae insert into the belly of the anterior leaflet while posterior intermediate chordae insert into the belly of the posterior leaflet. Tertiary (also referred in literature as basal) attach to the base of the anterior leaflet, base of the posterior leaflet, or directly into the mitral annulus. Commissural chordae insert to the leaflet commissures and can originate from either of the papillary muscles. Anatomically, marginal chordae are

typically thinner than basal chordae, while strut chordae are the thickest in both human and ovine valves [51].

Considered in isolation, the chordae tendineae experience counteracting tensile loads from the apically contracting papillary muscles and basally directed pressure forces acting on the valve leaflets. The magnitude of tensile loading experienced by each chord is dependent on chordal type, systolic transmitral pressure, and the total leaflet area exposed to the transmitral pressure gradient. As leaflet exposure area is directly related to mitral valve geometry, chordal loading is also related to the annular and subvalvular mitral valve geometry. Since the relationships between chordal structure, size, leaflet insertion, and mitral valve geometry are uniquely complex, many *in vitro* and *in vivo* investigations have focused on identifying the role and function of the chordae. The most complete description of chordal mechanics and function in both healthy and functional disease has been described by Rabbah and colleagues [51].

#### **2.1.4 The Mitral Valve's Intimate Relationship**

Considered together, the mitral annulus, leaflets, chordae tendineae, and papillary muscles are elegantly complex structures that facilitate unidirectional flow and valve closure. Due to their anatomical arrangement, the mitral valve is both structurally and functionally part of the left atrium, fibrous skeleton, and LV of the heart. For these reasons, gross geometric alterations in these structures can result in mitral valve dysfunction and incompetence [2].

## 2.2. Ischemic Mitral Regurgitation

Changes in mitral valve geometry and function may be most notably manifested in Ischemic Mitral Regurgitation (IMR). IMR can be defined as Mitral Regurgitation (MR) occurring as a result of chronic myocardial ischemia in the absence of any structural damage to the mitral leaflets, chordae tendineae, or papillary muscles [52,53]. This disease results from post-infarction LV remodeling with subsequent papillary muscle displacement, annular dilatation, leaflet tethering, and malcoaptation (Figure 2-6) [54,55].

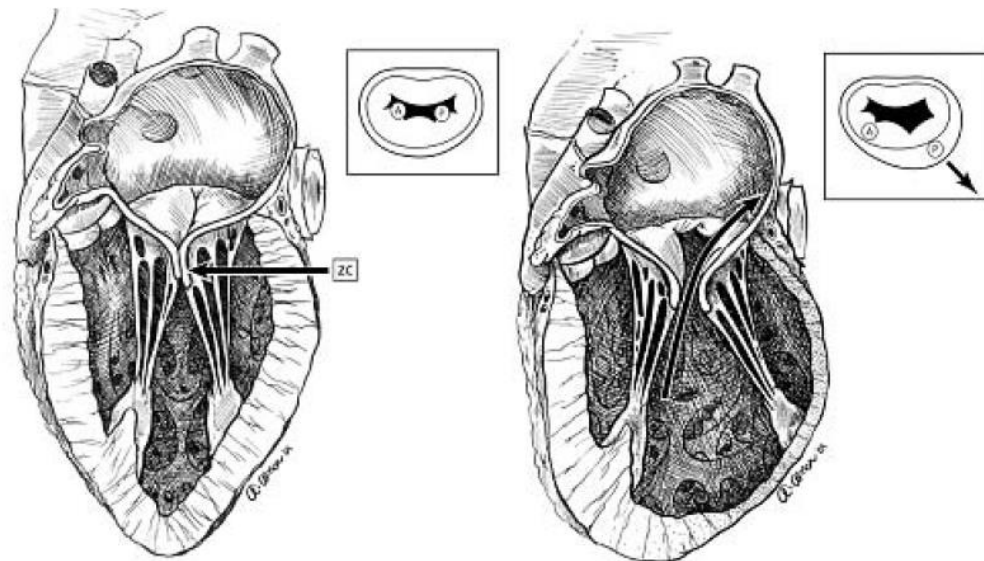


**Figure 2-6 Thinning and remodeling of post-infarction LV result in papillary muscle displacement and annular dilatation that is characteristic of an inferior myocardial infarction and mitral regurgitation (modified from [56]).**

Clinical studies have demonstrated that IMR is more likely to occur after a posteroinferior rather than an anterolateral LV infarction [53,57]. A report by Gillinov et al. involving nearly 500 patients treated over 13 years at the Cleveland Clinic confirmed the clinical importance of infarct location and size on the development of IMR [58]. In

this study, 73% of patients had posterior wall motion abnormalities and 63% had inferior wall motion abnormalities. Virtually all were found by echocardiography to have evidence of posterior and/or inferior myocardial infarctions. While infarctions in locations other than the inferior side occurred, they were less common and likely represent the diffuse nature of coronary atherosclerosis that is present in most IMR patients [54].

Recent studies estimate the prevalence of IMR within the United States to be approximately 1.6 to 2.8 million patients [4]. Beyond its wide prevalence, IMR has been found to significantly impact patient prognosis. Post-myocardial infarction patients have been found to exhibit 1-year mortality rates of 52% with severe MR, 22% for mild to moderate IMR, and 11% for no IMR [4]. The presence of patient comorbidities can compound IMR's effect, yielding the cessation of MR as being necessary but not sufficient to improve patient outcomes. If left untreated, the clinical consequence of severe IMR is excess morbidity and mortality [59]. While infarcts vary widely in age, size, and location; several studies have identified the effects of inferior myocardial infarctions on ventricular dilatation and geometric MV distortion.

### **2.2.1 Geometric and Functional Effects of an Inferior Left Ventricular Infarction**

In the setting of an inferior chronic LV myocardial infarction, the mitral annulus and papillary muscles are displaced asymmetrically (Figure 2-6) [1,2,4,31,41,48,54]. The annulus characteristically dilates towards the posteroinferior direction by as much as 125-200% of the subject's healthy annular area [31,33,41,48]. The posteromedial papillary muscle commonly distends more than the anterolateral papillary muscle as dictated by the

pattern of LV infarction and dilatation [53,57,58]. In combination, these geometric distortions result in asymmetric leaflet tethering and asymmetrically directed regurgitation jets (Figure 2-7). More centrally directed MR jets can additionally occur depending on the pattern of MV geometric tethering. While vector distances between the mitral annulus and the papillary muscles have been reported in clinical studies [27,60,61], the most complete geometric information for how the mitral-LV apparatus changes, albeit in one presentation of an inferior myocardial infarction, has been reported by animal studies [55,62,63].



**Figure 2-7 Example of an asymmetrically directed regurgitation jet from an inferior left ventricular infarction.**

### **2.2.2 Current Trends and Operative Strategies for Ischemic Mitral Regurgitation**

No optimal medical treatment or therapy exists for IMR patients. Current surgical strategies include mitral valve repair, replacement, and minimally invasive/percutaneous mitral valve repair [4,5]. Today, the preferred surgical treatment is undersized mitral annuloplasty (UMA). In this procedure, the mitral annulus is constrained to the shape and

size of an undersized complete rigid annuloplasty ring (Figure 2-8) [64]. This technique forces the mitral leaflets into apposition in order to compensate for excessive subvalvular mitral leaflet tethering. This procedure has been demonstrated to be successful for the majority of IMR patients by restoring leaflet coaptation, reducing or eliminating MR, and promoting reverse LV remodeling [23-25].

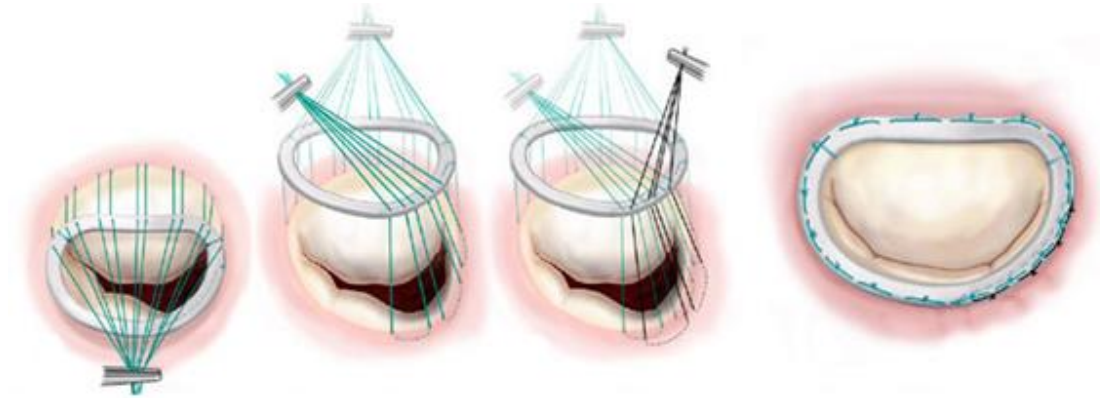


**Figure 2-8 Undersized mitral valve annuloplasty (modified from [1]).**

When MV repair is not feasible, mitral valve replacement is considered as a secondary option. In this procedure, a mechanical or tissue heart valve is implanted in the mitral annulus to replace native mitral valve function (Figure 2-9). While historically considered as a less effective option for IMR patients, a recent clinical trial has aimed to compare the clinical outcomes of mitral annuloplasty and mitral valve replacement in patients with severe IMR [5]. Preliminary data has demonstrated no significant difference between patient groups in LV reverse remodeling or one year survival. Replacement was demonstrated to provide a more durable correction of mitral regurgitation, but there was no significant between-group difference in clinical outcomes. This clinical study is



currently ongoing whose results may significantly influence the future operative care of severe IMR patients.

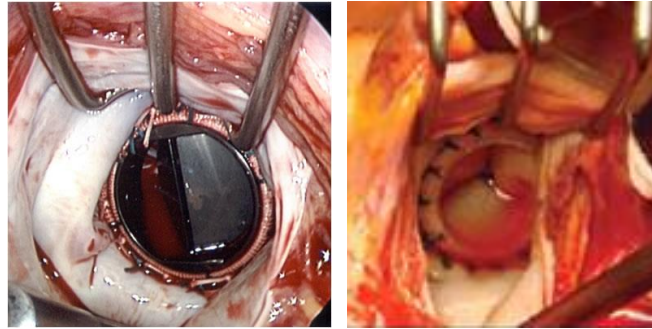


**Figure 2-9 Left: Mitral valve replacement using a bileaflet mechanical heart valve; Right: Mitral valve replacement using a bovine pericardium valve (modified from [117]).**

A significant challenge in IMR is treating patients who are elderly and are presented with significant comorbidities. These characteristics represent a large and growing patient population who are considered by many as too high-risk for open-heart surgery [6-9]. This trend, paired with a rising desire for less invasive approaches, has led to the development of minimally invasive and percutaneous surgery for IMR. The devices used in these approaches can be broadly characterized into designs that aim to repair mitral valve function by performing direct annuloplasty, indirect annuloplasty, or leaflet clipping (Figure 2-10) [7,9,10, 64-72]. Additional technologies dedicated to directly replacing the MV are in development but are not yet commercially available (Figure 2-10) [7,9,10]. While these techniques exhibit potential for treating a large number of patients, the relative effectiveness of these therapies remains under active exploration.

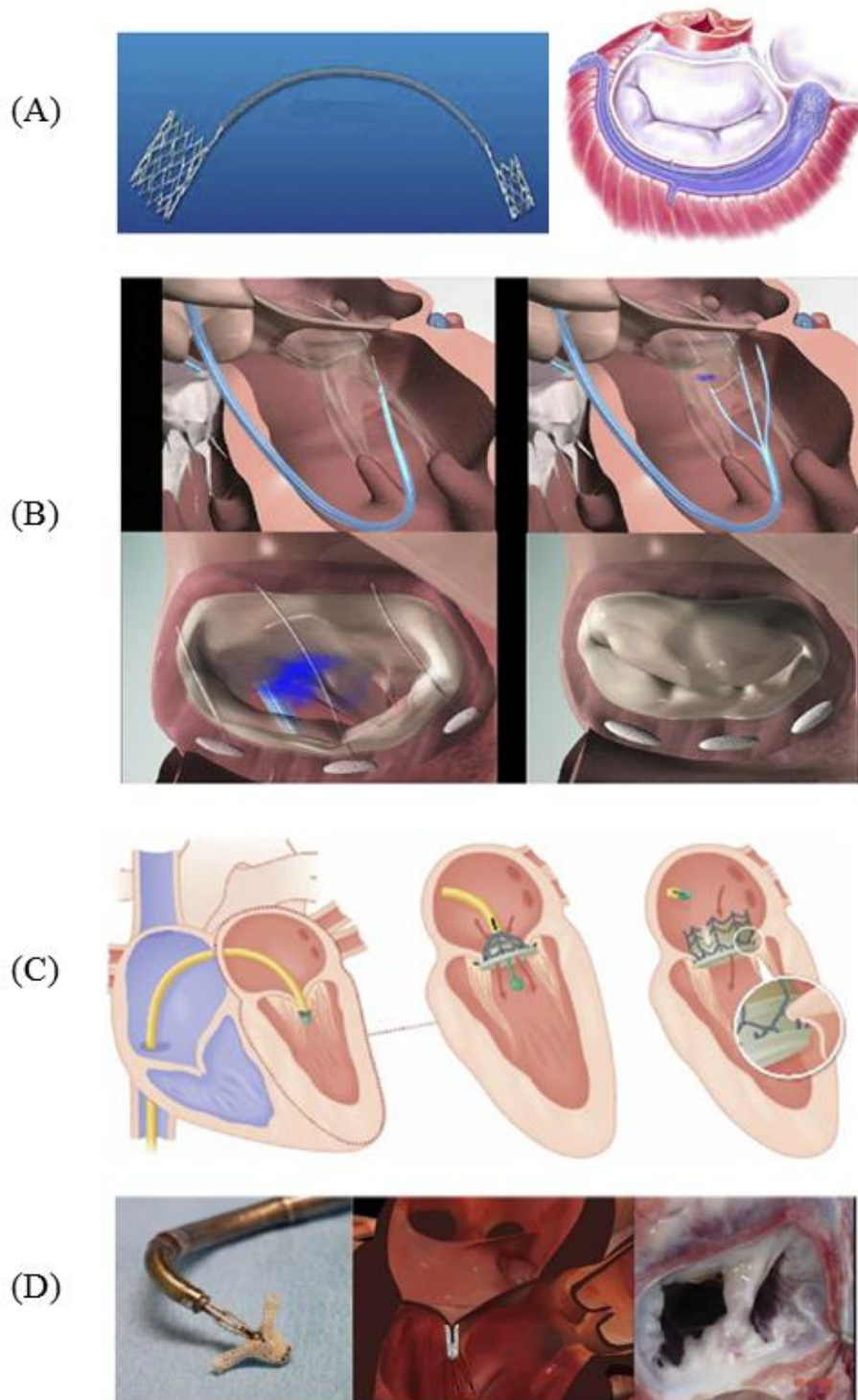


**Figure 2-10** Examples of different percutaneous MV devices that include (A) the Monarc device for indirect annuloplasty, (B) the Mitralign device for direct annuloplasty, (C) the CardiAQ prosthesis for MV replacement, and (D) the Mitraclip for edge-to-edge leaflet approximation (images modified from [7]).

## **2.3 Suboptimal Surgical Outcomes in Ischemic Mitral Regurgitation**

### **2.3.1 Structural Failure of Minimally Invasive Devices**

A key to demonstrating equivalent or improved clinical therapeutic benefits for minimally invasive and percutaneous IMR devices is the development of designs that not only facilitate delivery but reduce IMR. While reductions in regurgitation have been demonstrated in preclinical studies, concerns have been raised regarding the safety of annular based devices [7,8,9,10,73]. In specific, these devices are structurally smaller, more flexible, and may be less durable than comparably rigid replacement valves or rigid undersized complete annuloplasty rings. As a result, these devices may experience greater structural deformations and as such may be more prone to strain related material failure. For these reasons, it is not surprising that both clinical and preclinical annular device failures have been reported [7,9,10]. The number of these failures is likely much greater given the pressures within the discipline to reserve reporting to positive results.

### **2.3.2. Annuloplasty Ring Dehiscence**

The preferred reconstructive surgery for IMR is undersized complete rigid ring annuloplasty. While effective in the majority of patients, postoperative complications can lead to short-term repair failure [74]. One increasingly acknowledged short-term failure is annuloplasty ring dehiscence [11-22]. In IMR, ring dehiscence commonly occurs along the posterior annulus [11-18] with select cases resulting in complete separation of the ring from the annulus (Figure 2-11) [19,20]. While these failures are often attributed to surgical technique, no studies have identified whether suture failure, knot failure, or annular tissue tearing is the primary cause of dehiscence. Identifying and understanding

these mechanisms may significantly improve patient-ring selection, ring design, and surgical implantation.

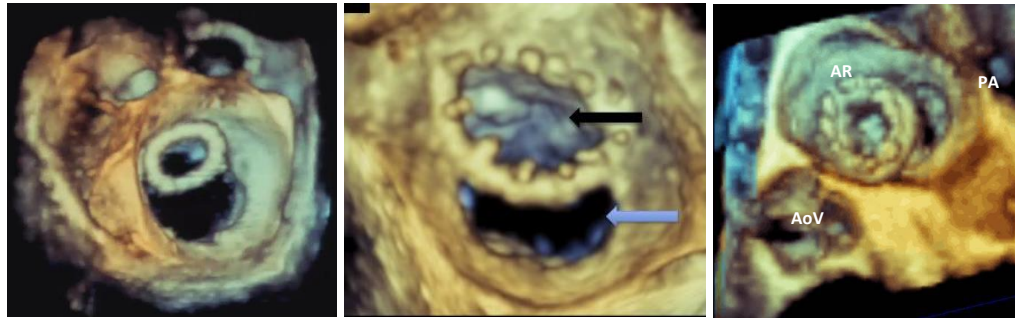


**Figure 2-11 Annuloplasty ring dehiscence echocardiographic images.**

### **2.3.3. Recurrent Mitral Regurgitation Following Undersized Mitral Annuloplasty**

While effective in the majority of cases, approximately 10-15% of patients who present with a severely distended left ventricle and undergo undersize mitral annuloplasty suffer from recurrent severe regurgitation, have low rates of reverse LV remodeling, and exhibit poor survival [23-29]. In these patients, implantation of an undersized ring can hoist the posterior annulus anteriorly without displacing the anterior annulus fixed at the aortic root (Figure 2-12). This result augments posterior leaflet tethering by increasing the distance between the papillary muscle tips and posterior annulus. In the setting of progressive LV dilatation, both mitral leaflets can become further tethered leading to restrictive leaflet motion and recurrent mitral regurgitation [26-29].

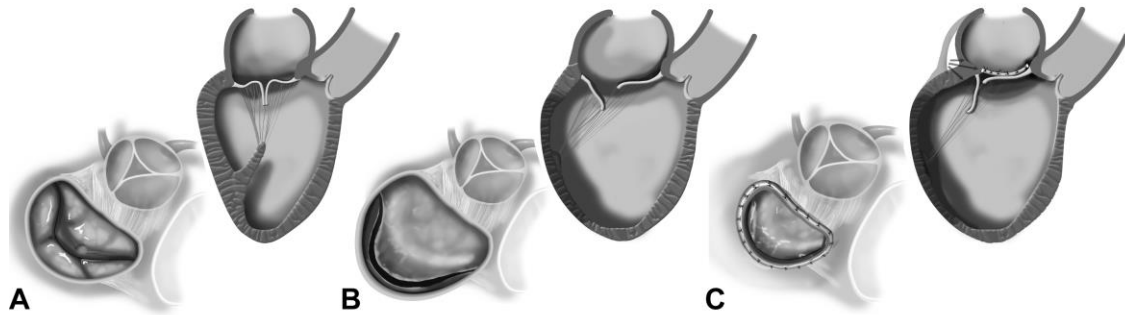


**Figure 2-12 (A) Normal mitral valve geometry; (B) Illustration of the annular dilatation and leaflet tethering associated with ischemic mitral regurgitation; (C) With a severely dilated left ventricle, undersized mitral annuloplasty can result in a mono-leaflet valve and exacerbation of posterior leaflet tethering.**

## **2.4 Recent Investigations Contributing to the Improvement of Suboptimal Surgical Outcomes in Ischemic Mitral Regurgitation**

### **2.4.1 What Forces May Act On Annular Based Mitral Valve Devices?**

Despite parallel advances in engineering and medical image technology, only limited information is available for the forces and deformations experienced by devices implanted to the mitral annulus. The majority of studies seeking to measure mitral annular forces have focused on quantifying cyclic planar compression (Figure 2-13). In 1994, Hasenkam and colleagues were the first to describe the forces generated by the myocardium on 29 mm Edwards-Duromedics mitral valves [75]. Within seven healthy porcine subjects, a maximum in-plane force of 6-8 N was observed to act in a direction 30° clockwise from the transverse annular diameter.

Later in 2001, Shandas et al. used 3D ultrasound to measure the deformation of St. Jude Medical Biocor® stented prosthetic MVs in two healthy porcine subjects (Figure

2-13) [76]. Measured ring deformations were used as boundary conditions for finite element analysis, which estimated the maximum septal-lateral force to fall between 4.4 and 13.9 N. This large range of peak force is likely due to the limited number of experimental subjects (n=2) and limitations of using 3D intravascular ultrasound to map 2D deformations of the stented valves for finite element modeling.

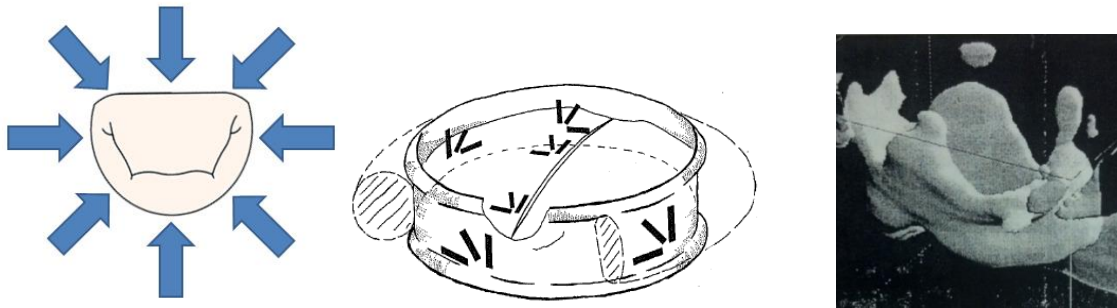


**Figure 2-13 Left: Majority of experimental studies have sought to quantify the forces acting in-plane with the mitral valve annulus; Center: Hasenkam et al. [75] adhered strain gage rosettes to Edwards-Duromedics mitral valves to quantify planar forces; Right: Shandas et al. [76] used 2D deformations of stented prosthetic MVs measured by echo as boundary conditions in a finite element model.**

Each of these studies was pioneering in estimating the radially-directed forces that the myocardium can generate on implanted prostheses. However, the combined results of these studies were unable to identify a common direction of maximal force or quantitatively compare the magnitude of these forces with other radial directions. Moreover, each study provided a large range of forces whose rate, correlation with left ventricular pressure, and change with hypertensive and disease conditions remains unknown.

Determining these unknowns are critical for the design and evaluation of minimally invasive and transcatheter devices. As many of these devices are directionally

heterogeneous, evaluating directional differences in force with increasing ventricular afterload can inform worst-case loading conditions. Determining the rate change of these forces during ventricular contraction will additionally inform device testing and the use of device materials with rate or time dependent material properties. The ability to quantify these endpoints in the presence of an inferior left ventricular infarction will additionally and significantly contribute to the development of minimally invasive and percutaneous IMR devices.

#### **2.4.2. What Causes Annuloplasty Ring Dehiscence?**

No studies have identified whether suture failure, knot failure, or annular tissue tearing is the primary cause of annuloplasty ring dehiscence [11-22]. To the author's knowledge, only two studies have evaluated suture failure in ring annuloplasty. In a study evaluating the safety of annuloplasty rings for magnetic resonance imaging, annuloplasty ring-tissue tear out forces were evaluated. Among patients with varying MV disease, single sutures were shown to tear from MV annular tissue with a mean force of  $6.0 \pm 4.5$  N [77]. In the second study, Physio<sup>TM</sup> annuloplasty rings were implanted in explanted ovine hearts. With the heart anchored, the ring was pulled upward in a tensile test to evaluate the total force required to tear a ring from the annulus (Figure 2-14) [78]. Results demonstrated the rings to tear from the annular tissue at approximately  $140 \pm 33$  N (~12 N per suture).

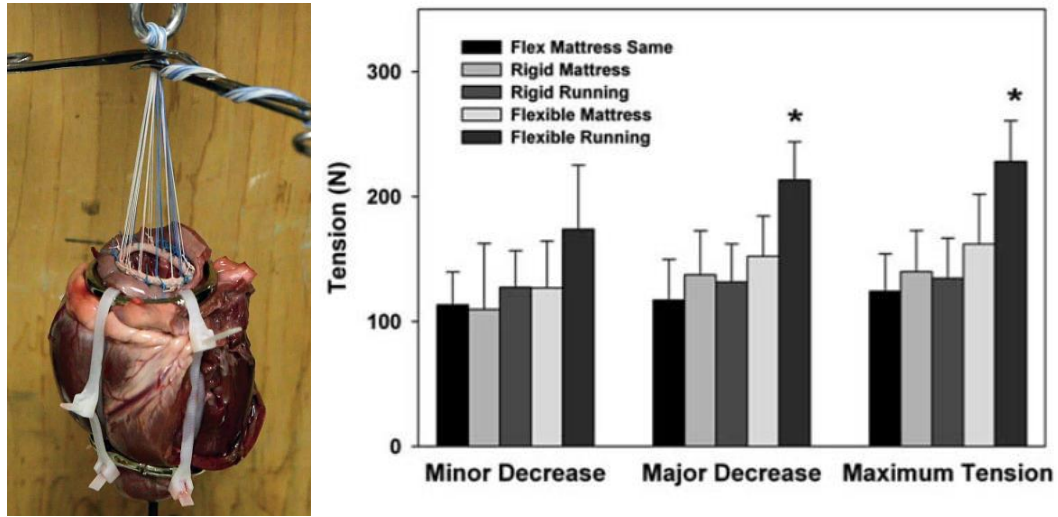


**Figure 2-14 Left: Ring pull out test experimental set-up; Right: Results of the tests for the indicated annuloplasty rings and ring suturing procedure where minor and major decrease correspond to momentary drops in force during the tensile test which correspond to select ring sutures failing (modified from [78]).**

Each of these studies has provided preliminary insight to the forces required to pull rings from the annulus but were unable to identify the mechanisms of ring dehiscence. The inability to identify the mechanisms has contributed to large uncertainty for the conditions under which it is most likely to occur. One route towards addressing this challenge is to measure suture forces at ring implantation and during cyclic contraction of the heart. Quantifying these forces and comparing them to the forces associated with suture failure or tissue tearing will significantly contribute to our clinical understanding of dehiscence. Moreover, these data will aid in developing new ring designs and surgical approaches to reduce its occurrence.

### **2.4.3. Can Repair Induced Mitral Leaflet Tethering be Predicted Preoperatively?**

Repair failure after undersized annuloplasty results from progressive LV dilatation, leaflet tethering, and LV dysfunction implicating a mal-distribution of annular and



subvalvular stresses as a probable mechanism [26,28,51]. In these patients, the severely or progressively displacing papillary muscles hinder undersized annuloplasty's ability to sustain coaptation and urges the use of adjunct procedures to directly address subvalvular tethering [26-29]. While adjunct procedures have demonstrated effectiveness [64, 79-86], several issues impede our ability to optimally treat these patients.

A primary issue relates to identifying patients who will benefit from sole undersized mitral annuloplasty [87]. While several ventricular- and leaflet-based measures have been demonstrated to significantly correlate with patient outcomes [24,87-91], no metrics directly quantify the geometric papillary muscle distortions that give allowance or alternatively impede the compensatory effects of undersized annuloplasty. A secondary issue is the need to understand the geometric mechanisms and limits of adjunct procedures to assess their suitability for maintaining coaptation with severe or progressive papillary muscle displacement. The ability to directly assess these issues will aid in identifying patients who may benefit from a given treatment while additionally contributing to the improvement and individualization of treatment modalities [87].

Matching the best IMR surgical procedure to a given patient mitral valve geometry may soon be possible with *in silico* mitral valve models (Figure 2-15). These models hold significant potential for preoperative surgical planning, assessing repair complexity, and accelerating training for surgical techniques. These models began as idealized mitral leaflets and have grown to incorporate anisotropic nonlinear material properties, *in vivo* tissue architecture, structural representation of the subvalvular apparatus, and the LV [92-101]. While significant technological advances have been made, many challenges remain for these virtual mitral valve models.

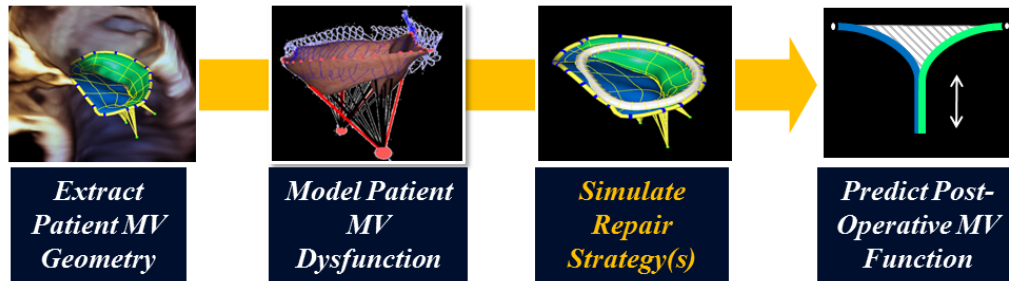


**Figure 2-15 Example progression of data flow for patient-specific surgical planning using *in silico* modeling.**

One of the most significant challenges is modeling the complex architecture and function of the mitral valve’s chordae tendineae. Current standard-of-care echocardiography is unable to spatially resolve detailed chordal architecture requiring mitral valve models to employ idealized chordal distributions (Figure 2-16) [92-100, 102]. These idealized chordal geometries can differ greatly from native valves and have been demonstrated to impact mitral valve simulation results [95,101]. Compounding this uncertainty is the lack of experimental data providing boundary conditions for how the tethering of the chordae may change from IMR to UMA. Addressing both challenges is critical for improving IMR surgical planning tools and advancing their predictive capabilities.

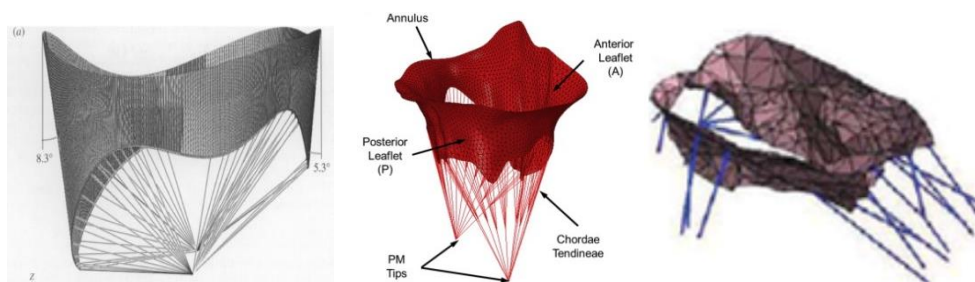


**Figure 2-16 Images from recently published *in silico* mitral valve models showing the simplifications in modeling the complex chordae tendineae (images modified from [98, 97, 102]).**

One step towards improving mitral valve modeling therefore is to define boundary conditions that describe the changes in chordal-leaflet tethering that occur with the mitral's primary load bearing chordae in IMR and undersized annuloplasty. While select *in vitro* and large animal studies have quantified chordal forces [51], no studies have quantified chordal tethering during the sequential transition from a healthy to IMR and annuloplasty conditions. The ability to quantify chordal forces in these conditions will therefore enhance computational model development and move steps closer to predicting post-operative mitral valve function.

## CHAPTER 3

### OBJECTIVE AND SPECIFIC AIMS

Ischemic mitral regurgitation occurs when the heart's mitral valve is rendered incompetent by post-infarction left ventricular remodeling and three-dimensional alterations in mitral valve geometry [2]. These alterations include papillary muscle displacement and annular dilatation, which ultimately lead to restricted leaflet motion and mitral regurgitation [54,55]. While the severity of this disease can vary, IMR typically presents with significant comorbidities yielding the cessation of regurgitation as being necessary but not sufficient to improve patient outcomes. For these reasons among others, an optimal IMR surgical repair has yet to be established [4,5]. Finding an optimal surgical strategy has included the development of novel implantable devices and techniques for both open-chest, percutaneous, and transcatheter approaches. Despite published successes, post-operative device and repair induced complications have been documented. These include but are not limited to device fracture in pre-clinical trials [7,9,10], annuloplasty ring mattress suture dehiscence [11-22], and post-operative chordal-leaflet tethering [23-29]. From any of these adverse events recurrent regurgitation can ensue, leading to impaired left ventricular function, worsened patient health, and mortality [4]. A common thread to these outcomes is the presence or imbalance of mechanical forces acting on implanted devices, on mitral annular mattress sutures, and in the mitral valve's chordae tendineae. Little or no knowledge exists for the magnitude of these forces or their variations with left heart function under healthy and

IMR conditions [51]. Understanding the relative magnitude and variation of these forces will significantly aid the development of more robust devices, improve knowledge for device implantation, and contribute to methods designed to predict or reduce postoperative chordal-leaflet tethering. To this end, the **central hypothesis** of this study is: *Determining the forces that exist at the annular and subvalvular levels under normal, IMR, and repair conditions will allow for the development of more durable IMR devices and repairs.* To this end, the following specific aims have been formulated.

**Specific Aim 1:** *Quantify the contractile mitral annular forces that may contribute to device failure.*

Radial forces resulting from mitral annular contraction are currently unknown. Determining these forces will help define the appropriate and relevant boundary conditions for the development and testing of robust mitral valve devices. For this purpose, novel strain gage based transducers will be developed and implanted in normal and chronic IMR Dorsett hybrid sheep. Cyclic forces will be measured in the septal-lateral and transverse annular directions at baseline and elevated levels of left ventricular pressure. These analyses will provide key insight to the forces that exist within the annulus and their correlation with the condition and function of the native heart.

**Specific Aim 2:** *Quantify the suture forces required to constrain true-sized and undersized annuloplasty rings to the ovine mitral valve annulus.*

While ring suture dehiscence is often attributed to surgical technique, no studies have identified whether suture, suture knot, or tissue tearing is the primary mechanism of

clinical ring dehiscence [11-22,77,78]. Moreover, no data exist for whether patient-ring selection contributes to excessive ring suture forces. These factors in combination have contributed to large uncertainty for what causes suture dehiscence and under what conditions suture forces may be exacerbated. Mattress suture force transducers will be developed and fixated to Carpentier-Edwards Physio™ annuloplasty rings. Instrumented undersized and true-sized annuloplasty rings will be implanted in eight ovine animals. Suture forces will be measured at both baseline and elevated levels of left ventricular pressure. These results will demonstrate how suture forces vary with ring-annular sizing, ring position, and annular region. The results of this aim will provide insight to the mechanisms by which suture dehiscence may occur in the clinic.

***Specific Aim 3: Evaluate the effects of mitral valve annuloplasty on chordal-leaflet tethering forces.***

Quantifying tethering among all strut chordae in the sequential transition from IMR to varying degrees of undersized annuloplasty within patients or animal models is not feasible. *In vitro* models may be a potential solution however the ability of these models to mimic healthy and IMR mitral valve function has not been assessed. In part A of this aim, an *in vitro* mitral valve simulator's ability to mimic the systolic leaflet coaptation, regurgitation, and leaflet mechanics of a healthy and IMR ovine animals will be evaluated. In part B of this aim, the *in vitro* simulator will be used to quantify the isolated effects of IMR, oversized, true-sized, and undersized mitral annuloplasty on leaflet coaptation, mitral regurgitation, and tethering forces of the anterior strut and posterior intermediary chordae tendineae from both the anterolateral and posteromedial papillary

muscles. These data will provide key insights into how chordal tethering patterns can change from IMR to annuloplasty. These data will aid the further development of methods designed to predict or reduce postoperative chordal-leaflet tethering.

## **CHAPTER 4**

### **MATERIALS**

#### **4.1 Specific Aim 1 Materials**

##### **4.1.1 Mitral Annular Force Transducer**

The mitral annular force transducer was manufactured using 19 materials from five suppliers. These items are listed in Table 4-1. Several materials may be substituted for others that exhibit similar purpose. These materials include items 5, 6, 11,12, 14, 18, and 19.



**Table 4-1 Materials used for the manufacturing of the mitral annular force transducer.**

<b>No.</b>	<b>Item</b>	<b>Supplier</b>
<b>1</b>	Rapid Prototyped Spring element (MicroFine Green)	Fineline Prototyping (Raleigh, NC)
<b>2</b>	Loctite® M-31CL™ Hysol® Medical Device Epoxy	Ellsworth Adhesives (Germantown, WI)
<b>3</b>	M-Prep Conditioner A	
<b>4</b>	M-Prep Neutralizer 5A	
<b>5</b>	Cotton Applicators	
<b>6</b>	Gauze sponge	
<b>7</b>	EA-031DE-350 resistance strain gages	
<b>8</b>	M-Bond 200 Adhesive	
<b>9</b>	M-Bond 200 Catalyst	
<b>10</b>	PCT-2M Gage Installation Tape	Vishay Micro-Measurements (Wendell, NC)
<b>11</b>	M5S-1 Mark V soldering station	
<b>12</b>	361A-20R solder	
<b>13</b>	336-FTE three stranded wire	
<b>14</b>	M-Line Rosin Solvent	
<b>15</b>	M-Coat B Nitrile Rubber	
<b>16</b>	3140 RTV Silicone Rubber	
<b>17</b>	3145 RTV Silicone Rubber	
<b>18</b>	0.005” High Purity Silicone Rubber Sheet	McMaster-Carr (Atlanta, GA)
<b>19</b>	1/8” wire heat shrink	ACK Electronics (Atlanta, GA)

#### **4.1.2 Mitral Annular Force Transducer Calibration Apparatus**

To facilitate mitral annular force transducer calibration, a well-defined calibration apparatus was developed (Figure 4-1). The apparatus had the ability to impose septal-lateral and transverse forces either independently or in concert. Loading of each transducer within the apparatus is accomplished through the use of bolt-piston-spring-pusher assembly located in the septal-lateral and transverse and loading mechanisms. This mechanism is shown in detail in Figure 4-2. Based on previous studies, each

transducer was calibrated from 0 to 8.4 N (in 1.2 N increments) while submerged in a 37°C water bath to mimic the physiologic temperature of the ovine subjects [75,76]. Loading can be completed in 0.6 N increments by turning the driving screw one-half rotation. At each increment, an ultra-precision spring (Gardner Spring GCO300-022-0688, 0.30 x 0.022 x 0.688, McMaster Carr, Atlanta, GA) is compressed applying a force to the pusher in contact with the transducer.

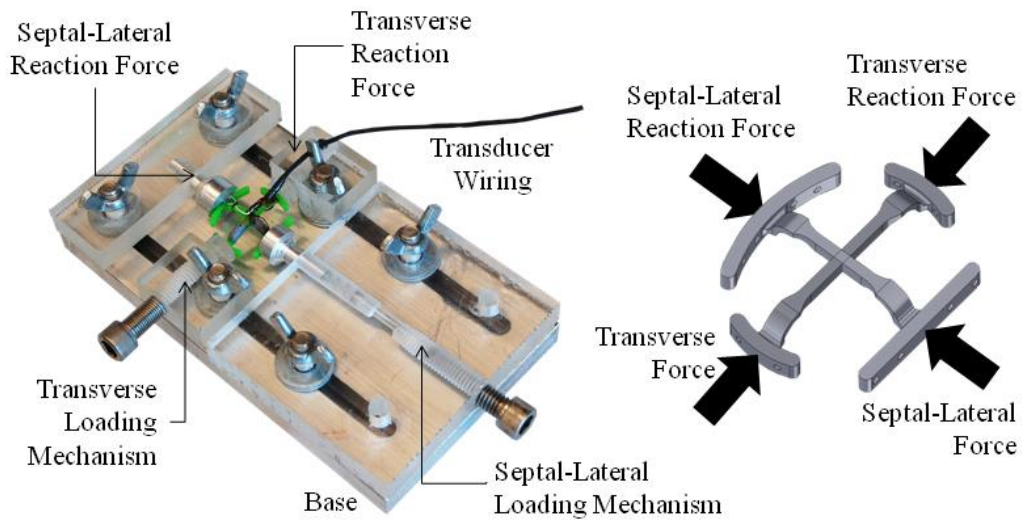


**Figure 4-1 Bi-axial calibration apparatus with a schematic representation of what forces are applied to the device, forces are applied via a spring-piston system such that spring compression elicits a force on the transducer.**

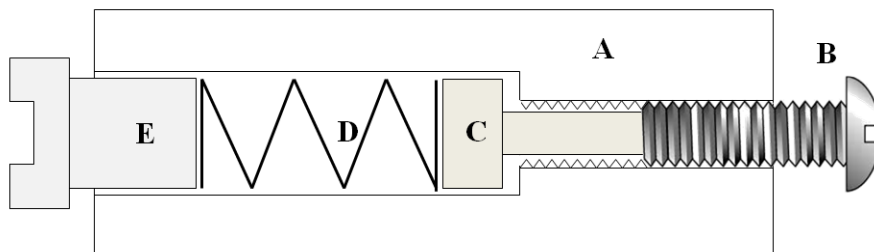


**Figure 4-2 (A) Acrylic housing, (B) Bolt, (C) Piston, (D) Precision compression spring, (E) Pusher which is in contact with the force transducer.**

### **4.1.3 Healthy and Ischemic Mitral Regurgitation Ovine Model**

The animals used in this work received care in compliance with the protocols approved by the Institutional Animal Care and Use Committee at the University of Pennsylvania in accordance with the guidelines for humane care (National Institutes of Health Publication 85-23, revised 1996).

A healthy and chronic IMR ovine model was utilized for these studies. Animals randomized to the chronic IMR group received an inferior LV infarction to produce progressive chronic IMR. This model has been extensively studied and mimics a common clinical presentation of an inferior myocardial infarction described in humans [33,41,48]. In short, this LV infarction is achieved through a sterile left lateral thoracotomy. In this procedure, snares are placed to occlude the proximal second and third obtuse marginal branches of the circumflex coronary artery. Following infarction the thoracotomy is closed and IMR allowed to progress for a 6 to 8 week period prior to carrying out the experimental protocol.

## **4.2 Specific Aim 2 Materials**

### **4.2.1 Healthy Ovine Model**

The ovine model used in this Aim is identical to that described in Section 4.1.3.

### **4.2.2 Mitral Annuloplasty Ring Stress Transducer**

A mitral annuloplasty ring stress transducer was manufactured using 18 materials from six suppliers. These items are listed in Table 4-2. Several materials may be substituted for

others that exhibit similar purpose. These materials include items 2, 5, 6, 11-13, 16 and 17.

**Table 4-2 Materials used for the manufacturing of the ring stress transducer.**

<b>No.</b>	<b>Item</b>	<b>Supplier</b>
1	Titanium (6-AL 4V) for the Annuloplasty Ring Core	McMaster-Carr (Atlanta, GA)
2	Loctite® M-31CL™ Hysol® Medical Device Epoxy	Ellsworth Adhesives (Germantown, WI)
3	M-Prep Conditioner A	
4	M-Prep Neutralizer 5A	
5	Cotton Applicators	
6	Gauze sponge	
7	EA-031DE-350 resistance strain gages	
8	M-Bond 43	
9	PCT-2M Gage Installation Tape	Vishay Micro-Measurements (Wendell, NC)
10	M5S-1 Mark V soldering station	
11	361A-20R solder	
12	CEG 25C Bond Terminals	
13	336-FTE three stranded wire	
14	M-Line Rosin Solvent	
15	M-Coat B Nitrile Rubber	
16	1/4" wire heat shrink	ACK Electronics (Atlanta, GA)
17	Plasti Dip (Liquid Rubber)	Home Depot (Atlanta, GA)
18	611 Double Velour Cardiovascular Fabric	C.R. Bard (Murray Hill, NJ)

#### **4.2.3 Mitral Annuloplasty Ring Suture Force Transducer**

The mitral annuloplasty ring suture force transducer was manufactured using 17 materials from four suppliers. These items are listed in Table 4-3.

**Table 4-3 Materials used to manufacture the mitral annuloplasty ring suture force transducers.**

<b>No.</b>	<b>Item</b>	<b>Supplier</b>
1	Rapid Prototyped Spring element (316L Stainless Steel)	Fineline Prototyping (Raleigh, NC)
2	Loctite® M-31CL™ Hysol® Medical Device Epoxy	Ellsworth Adhesives (Germantown, WI)
3	M-Prep Conditioner A	
4	M-Prep Neutralizer 5A	
5	Cotton Applicators	
6	Gauze sponge	
7	EA-13-062TZ-350/E strain gages	
8	M-Bond 200 Adhesive	
9	M-Bond 200 Catalyst	Vishay Micro-Measurements (Wendell, NC)
10	PCT-2M Gage Installation Tape	
11	M5S-1 Mark V soldering station	
12	361A-20R solder	
13	CEG 25C Bond Terminals	
14	336-FTE three stranded wire	
15	M-Line Rosin Solvent	
16	M-Coat B Nitrile Rubber	
17	1/8" wire heat shrink	ACK Electronics (Atlanta, GA)

#### **4.2.4 Commercially Available Mitral Annuloplasty Rings**

Size 24-30 Carpentier-Edwards Physio™ rings (Edwards Lifesciences, Irvine, CA) were used for the suture force transducer studies.

## 4.3 Specific Aim 3 Materials

### 4.3.1 Healthy and Ischemic Mitral Regurgitation Ovine Model

The healthy and chronic IMR ovine model used in this Aim is identical to that described in Section 4.1.3.

### 4.3.2 Sonomicrometry Array Localization

Sonomicrometry was used to map the annular and subvalvular geometry of both healthy and chronic IMR ovine animals (Figure 4-3). Using published techniques, 2 mm hemispherical piezoelectric transducers (Sonometrics, London, Ontario) were localized to the mitral annulus (N=12), A2 anterior mitral leaflet (N=5), and papillary muscle tips (N=2) [33,41,48]. Each transducer was connected to a Series 5001 Digital Sonomicrometer (Sonometrics, London, Ontario). During each experimental study, the distance between sonometric transducers was measured at 200 Hz.



**Figure 4-3 Sonocrystal array localization for a chronic IMR animal to (Left) the mitral annulus and leaflets and (Right) the papillary muscles.**

### **4.3.3 Ovine Mitral Valves for *In Vitro* Simulation**

Fresh ovine hearts were obtained and MVs excised preserving their annular and subvalvular anatomy. MVs were selected for experimentation based on their anterior leaflet height, type I or II PMs, and with all leaflet chordae inserting directly into each PM. Part A of Specific Aim 3 (3A) utilized MVs with an anterior leaflet height of 18-19 mm while part B of Specific Aim 3 (3B) utilized MVs with anterior leaflet height of 20-25 mm. Upon mounting each valve within the Georgia Tech Left Heart Simulator, all experimental conditions are consistently completed within 12 hours from initial excision.

### **4.3.4 Georgia Tech Left Heart Simulator**

*In vitro* simulation of MV function was conducted in the extensively studied Georgia Tech Left Heart Simulator [103-113]. This closed-loop simulator allows for precise control of annular and subvalvular MV geometry at physiological left heart hemodynamic conditions (Figure 4-4). Excised ovine MVs were sutured to an adjustable annulus, designed to allow dilatation and to create an annular saddle shape. Two prosthetic annuli were used in this work. In aim 3A, the constructed annulus could dilate from a 6.5 cm<sup>2</sup> D-shaped orifice to 13 cm<sup>2</sup> and flatten from a maximum annular-height-to-commissural-width ratio of 20%. In Aim 3B, the constructed annulus could asymmetrically dilate to 9.8 cm<sup>2</sup> and conform to the shape of a size 26, 30, and 34 Physio<sup>TM</sup> annuloplasty ring. For each study, PM positions were controlled by two mechanically adjustable positioning rods capable of adjustment to varying positions in the apical, lateral, and posterior directions at a resolution of  $\pm 0.25$  mm. Transmitral flow was measured using an electromagnetic probe (accuracy  $\pm 0.05$  L/min) (Carolina Medical

Electronics, FM501D, East Bend, NC) mounted upstream of the atrium. Transmitral pressure was monitored with transducers (accuracy  $\pm 1$  mmHg) mounted in the atrium and ventricle (Validyne DC-40, Northridge, CA).

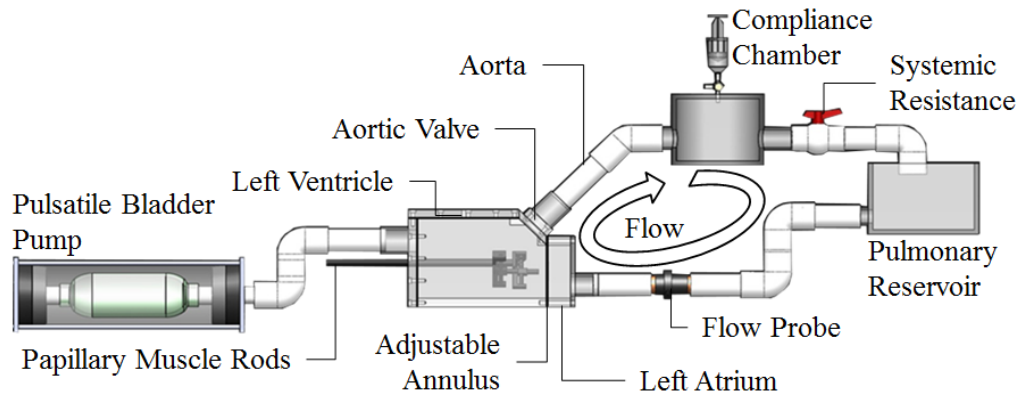


**Figure 4-4 Schematic of the Georgia Tech Left Heart simulator with components identified.**

#### 4.3.5 Chordae Tendineae Force Transducers

Miniature c-shaped force transducers have been used previously to quantify tethering forces of the MV's chordae tendineae (Figure 4-5) [104-108]. These transducers are strain gage based, manufactured, tested, and calibrated before and after each experiment within our laboratory. During calibration, the linear regression coefficient of the relationship between the calibrated load and transducer voltage output is between 0.98-1.00. The relative difference between measured and true values (accuracy) after calibration is less than 2% with a minimum measurable tension of approximately 0.01 N. Prior to each experiment, these transducers are sutured directly to selected chordae without altering the chordae's native length. Once a transducer is sutured to a chord, the section of chordae located between the transducer's measurement arms is transected such that all tensile loading of the chord is transferred to the transducer. Further details of instrumenting the chordae with these transducers can be found in the Methods Chapter.



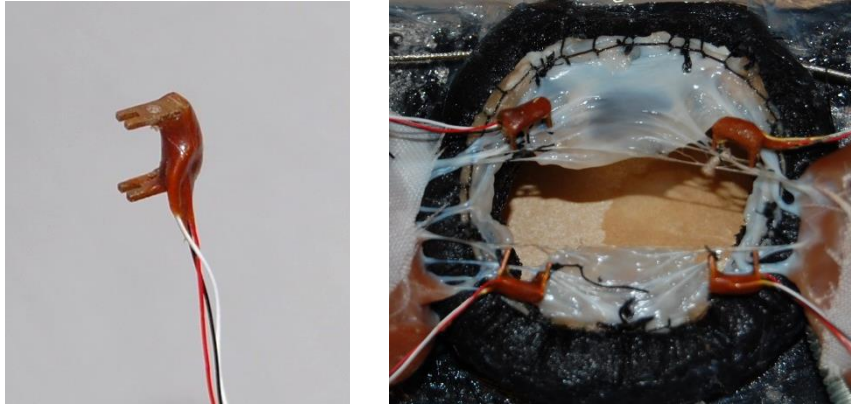


**Figure 4-5 Left: Chordal force transducer, Right: Attachment to the chordae to the strut and intermediary chordae of a mitral valve mounted to the mitral annulus as viewed from the apical aspect.**

#### **4.3.6 Stereo-Photogrammetry**

Dual camera stereo-photogrammetry has been successfully used in previous studies to measure *in vitro* MV leaflet strains [113-115]. In this method, tissue dye (Thermo Scientific, Waltham, MA) is used to mark the A2 cusp with a 3x3 rectangular dot array (Figure 4.6). Each leaflet marker is separated by approximately 1.5 mm and is 0.5 mm in diameter. These fiduciary markers are tracked throughout the cardiac cycle using two synchronized high-speed cameras (Basler Corp, Exton, PA) with Nikon macro lenses (105mm, f2.8; Nikon, Melville, NY) at 250 Hz. After calibration, acquired images are imported to a custom MATLAB program (See Appendix E) to calculate radial and circumferential anterior mitral leaflet strains.

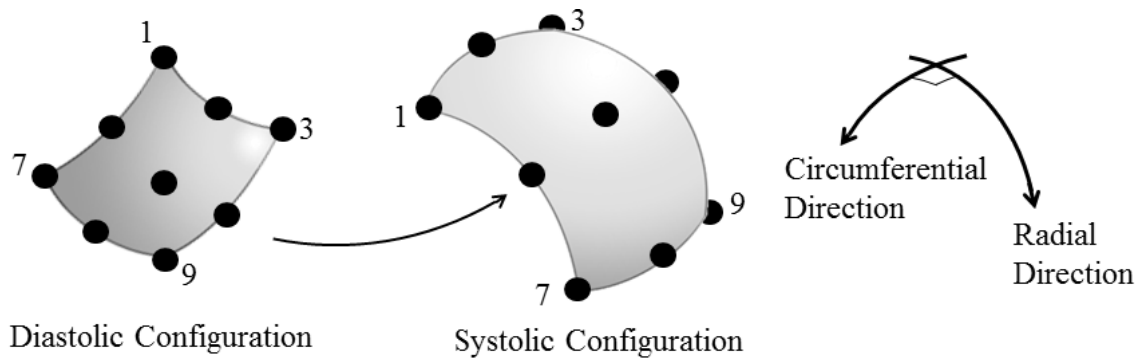


**Figure 4-6 Central A2 cusp of the anterior leaflet is marked with tissue dye then tracked throughout the cardiac cycle to quantify anterior leaflet strain.**

For image calibration, a 10 mm steel cube was positioned within the volume occupied by the MV leaflets such that each high-speed camera could image 7 of the cube's corners. These calibration images were digitized within a custom MATLAB program (See Appendix E) (Mathworks, Natick, MA). Using the cube calibration images and those recorded during each experiment, direct linear transformation was used to calculate the 4D coordinates of each leaflet marker [116]. These coordinates were exported into a custom MATLAB program (See Appendix E) utilizing biquintic finite element interpolation to fit a surface to the recorded marker coordinates. Generated surfaces were used to determine the average radial and circumferential strains of the anterior leaflet at peak systolic closure [113-115]. Based on the magnification of the high-speed cameras, pixel size, and calibration cube, the 3D leaflet marker coordinates was determined to an accuracy of  $\pm 68 \mu\text{m}$ . This accuracy is in good agreement with previous investigations [113-115].

### **4.3.7 Echocardiography**

All echocardiography imaging (*in vitro* and *in vivo*) was completed with an x7-2 probe and Phillips ie-33 Matrix machine (Phillips, Andover, MA). All images were analyzed using the Phillips QLab 9.0 software package.

## **CHAPTER 5**

### **EXPERIMENTAL METHODS AND PROTOCOLS**

#### **5.1 Specific Aim 1 Methods**

##### **5.1.1 Transducer Spring Element Design: Healthy Animals**

The spring element for the healthy animal mitral annular force transducer possesses several key attributes to allow the identified forces to be measured. The spring element consisted of 4 measurement arms that extend from a central point of intersection labeled as section C in Figure 5-1. For this spring element, strain gages are mounted to the top and bottom of locations D and E to measure forces in the anterolateral and transverse directions. Two strain gages were used at each location in case one failed during experimentation. Sections E and D were designed with a slight curvature to amplify surface deformation during loading; thus improving the signal to noise ratio for the strain gages mounted to those areas. The spring element contained 4 holes (1 mm diameter) (label A in Figure 5.1) for device annular suturing in sections B and F. Two device-annular suture holes were designed in Sections H and G.

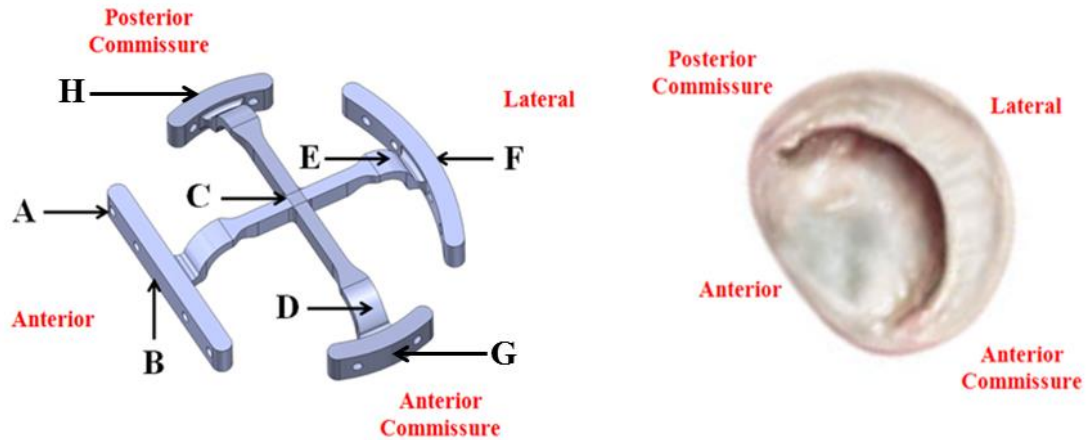


**Figure 5-1 Left: Spring element of the designed annular force transducer with selected highlights: (A) through holes for suturing the device to the mitral valve annulus, (B) anterior transducer arm, (C) central bridge area designed to both minimize transmitral blood flow obstruction and provide structural support, (D) location of strain gage to measure transverse force, (E) location of strain gage to measure anterolateral force, and (F) lateral transducer arm, (G) anterior commissure measurement arm, and (H) posterior commissure measurement arm; Right: Orientation of mitral valve with respect to the orientation of the transducer.**

During implantation, mattress sutures are passed through the annulus then through each hole in the transducer. This method of implantation is described later in Section 5.1.8. To minimize obstruction to transmitral flow, the central bridge area was optimized to maximize structural strength and prevent mitral stenosis. This was achieved by utilizing the maximum radial forces reported by Hasenkam and Shandas (8 to 13.9 N) as boundary conditions for a Finite Element Analysis (FEA) model in the SolidWorks 2010 program (Waltham, MA) [75,76]. Optimization of the bridge geometry was driven by the spring element's ability to (i) be rapid prototyped, (ii) maintain linear elastic deformation under the estimated forces, and (iii) deform at the selected strain gage application sites within the range of  $\pm 3\%$  strain.

To identify material candidates that fit the aforementioned criteria, a literature survey was performed and Somos 18420 was found to be a strong candidate for the

spring element's material. Material properties for it are listed in Table 5-1. This material is resin based and commercially available for rapid prototyping. Its material properties combined with dimensional iterations to the central bridge allowed the spring element to satisfy each of the aforementioned constraints. During the literature survey, it was found this material had been utilized in another study evaluating apical-basal forces of the mitral annulus within a porcine model [118,119]. In this study, the material proved to have adequate biocompatibility under acute conditions, possibly due to the reported material's low water adsorption characteristics.

**Table 5-1 Material properties of Somos 18420.**

Tensile Strength [MPa]	Tensile Modulus [GPa]	Poisson's Ratio	Flexural Strength [MPa]	Flexural Modulus [GPa]	Water Adsorption [%]	Glass Transition Temperature [deg F]
42.2-43.8	2.19-2.31	0.43-0.45	66.7-70.5	1.99-2.13	0.68	140

Using this material and iterating the spring element's design, the amount of mitral flow area obstructed by the central bridge area was 19%. These results are based on a mitral valve annular size equal to the outer circumference of the spring element. An FEA simulation that applied a 13.9 N load on both the anterolateral and transverse directions is pictured in Figure 5-2. Results showed strain gage areas on the atrial facing side reached a peak strain of approximately 1.8%.

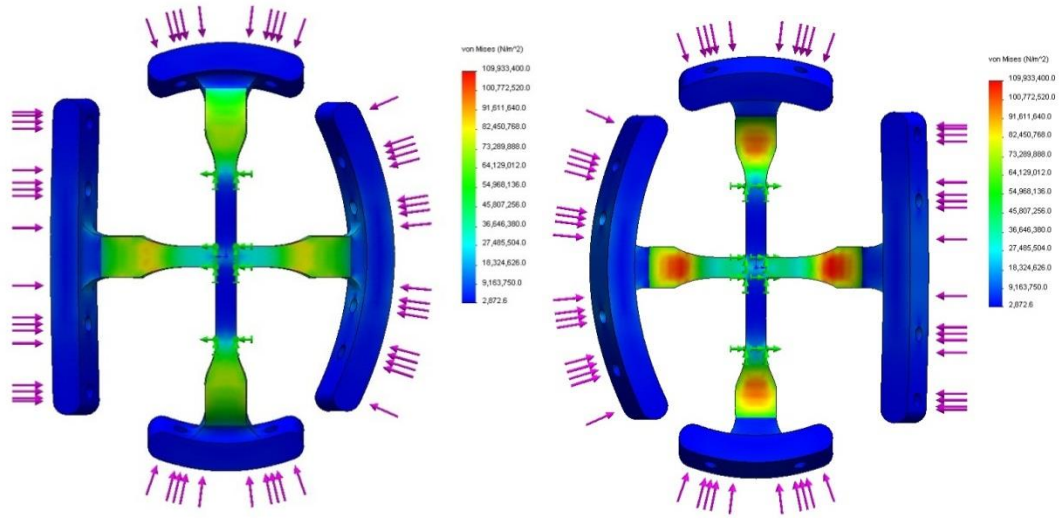


**Figure 5-2 Left: Top-view of the transducer with a load of 13.9 N placed in the anterolateral and transverse directions with the color green indicating a peak strain of approximately 1.8%; Right: Bottom view depicting the same loading conditions.**

The final criteria satisfied in the design of the normal annular force transducer spring element was allowing for several sizes to be manufactured. This allowed more flexibility in transducer-annular sizing for implantation. Three sizes were designed, each differing in major dimensions shown in Figure 5-3.

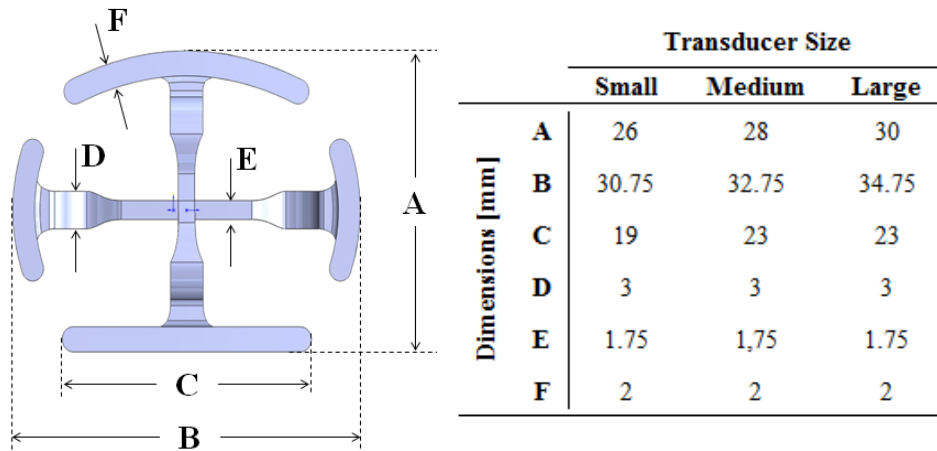


**Figure 5-3 Top-view of the acute animal spring element with dimensions noted.**

### 5.1.2 Transducer Spring Element Design: Ischemic Mitral Regurgitation Animals

A mitral annular force transducer spring element was specifically designed for the chronic IMR animals. This was necessary to counteract unforeseen loads acting on the transducer that for the first chronic IMR animal resulted in excessive transducer deformation (Figure 5-4). Post experiment, plastic deformation was found to be localized to the lateral and anterior commissure measurement arms. From observation, the deformation appeared to originate from a bending moment on the lateral measurement arm in the annular plane towards the anterior commissure. Some out of plane deformation was additionally observed in the anterior and posterior commissural arms.

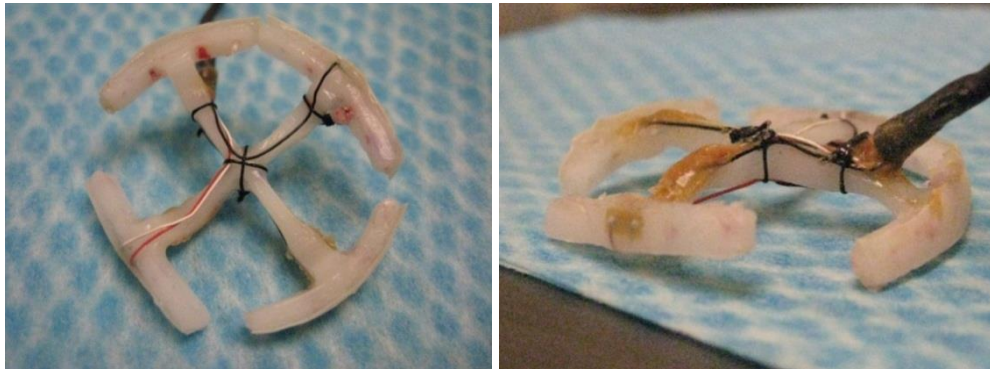


**Figure 5-4 Left: Plastic deformation of the transverse and lateral measurement arms; Right: out-of-plane plastic deformation occurring in the anterior and posterior commissural measurement arms.**

To assess the excessive deformation, a more robust design was created and is pictured in Figure 5-5. The design possessed several differences from the healthy animal transducer spring element that included: (i) a different material (MicroFine Green Resin), (ii) an increase in the radius of curvature in each measurement arm, and an (iii) increase in the overall thickness and width of each measurement arm. Material properties of MicroFine Green are listed in Table 5-2. MicroFine Green has very similar material



properties to that of Somos18420; however, MicroFine Green enables the production of parts with the finest features and tightest tolerances ( $\pm 0.002''$ ) available in industry. Thus, the material may act more as a homogeneous material rather than a layered rapid prototyped part. In the future, the use of a molded spring element may further improve element performance.

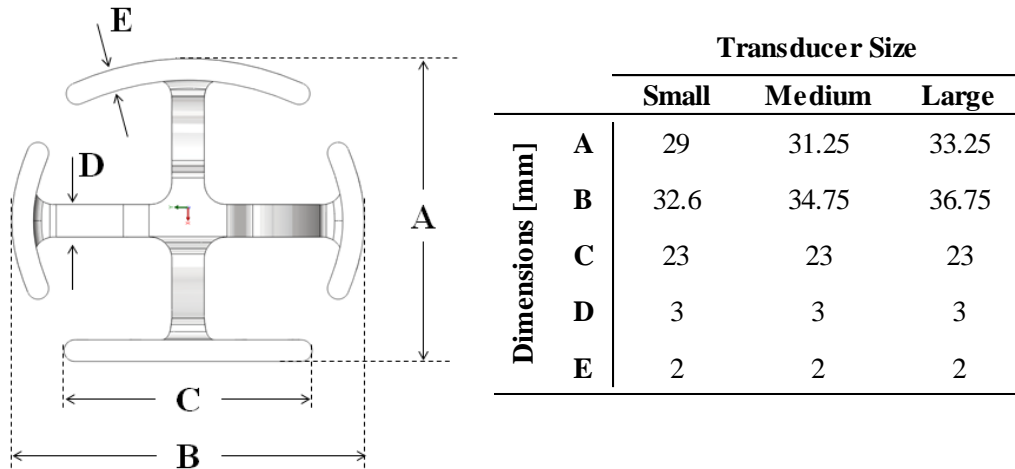


**Figure 5-5 Top-view of the chronic animal spring element with dimensions noted.**

**Table 5-2 Material properties of MicroFine Green resin.**

Tensile Strength [Mpa]	Tensile Modulus [Gpa]	Flexural Strength [Mpa]	Flexural Modulus [Gpa]	Water Adsorption [%]
44.9	2.1	74.3	2.2	0.7

Unlike the normal transducer parent geometries, the chronic IMR transducer geometry was only fabricated in the medium size. To test the design's ability to withstand known forces and a bending moment estimated to be responsible for the previous transducer's plastic deformation, FEA was utilized. In Figure 5-6, the FEA images represent the distribution of stress in the measurement arms when a load of 13.9 N is

applied in the anterolateral and transverse directions. Additionally, a 6 N bending moment is applied on the lateral measurement arm. Results of this analysis show a peak strain of 1.8% (shown in red) occurring on the posterior facing wall of the lateral measurement leg and a peak strain of 0.9% at the designated strain gage locations.

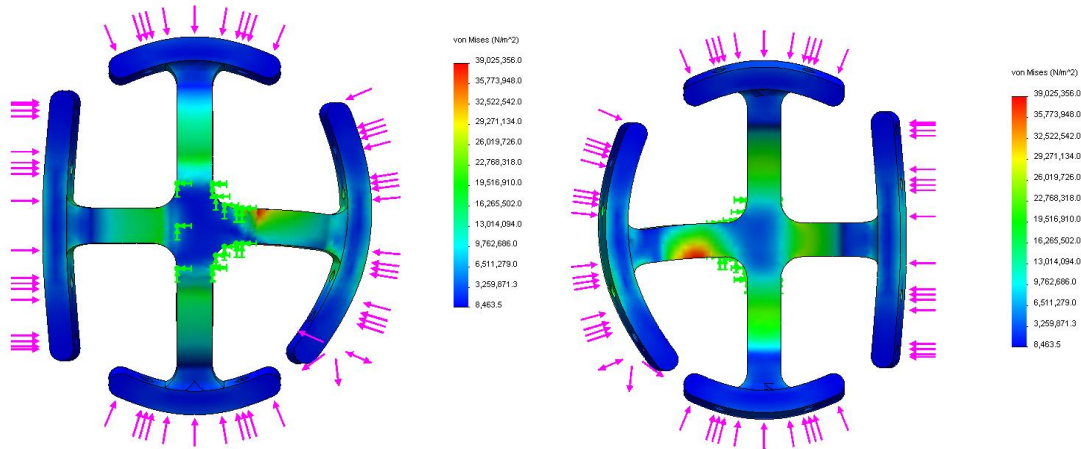


**Figure 5-6 Left: Top-view of the chronic animal transducer spring element’s FEA stress results when subjected to a 13.9 N force in the anterolateral and transverse directions as well as a 6 N force applied on the lateral measurement arm towards the anterior commissure arm; Right: Bottom-view of the same deformation; deformation scales are increased to display displaced positions.**

### 5.1.3 Transducer Function

The annular force transducers were designed to be strain gage based. These types of transducers are utilized in a wide span of applications, but all operate under a common principle [120]. Strain gages are adhered to a spring element which is designed to deform linear elastically when a range of expected forces is applied. Since the strain gages are adhered to the surface, they deform with the spring element which results in a change in the gage’s electrical output. Through calibration, changes in the electrical output of each gage can be correlated to a known force; thus allowing the transducer to be placed in the intended operating environment and measure the desired force. Accuracy and precision of

these devices is typically high but application specific [120]. Specifications of 0.03% or less are not uncommon in contemporary precision load cells.

#### **5.1.4 Transducer Fabrication**

The healthy and chronic IMR mitral annular force transducers were fabricated using 19 items (See Materials Section) and 13 steps. The steps to fabricate these devices were as follows:

**Step 1: Surface Coat.** One thin coat (<0.5 mm) of Loctite® M-31CLTM Hysol® Medical Device Epoxy Adhesive was applied to the spring element's surface. This coat was used to provide a smooth surface for strain gage application. A secondary result of this coat is a slight increase in material stiffness. During the epoxy's application, lateral suture holes located in each measurement arm were avoided to prevent hole occlusion. Following application, the adhesive layer was allowed to cure for 24 hours at room temperature. If suture passages are found occluded, a suture needle was heated under a flame and then passed through each hole to clear away excess epoxy.

**Step 2: Strain Gage Preparation.** Each strain gage was placed onto a glass surface and trimmed of excess material using a standard razor blade (Figure 5-7). This material was removed for two reasons: (i) for the strain gage to fit the geometric constraints of the spring element and (ii) to allow extra area around the gage for ample application of protective coatings.

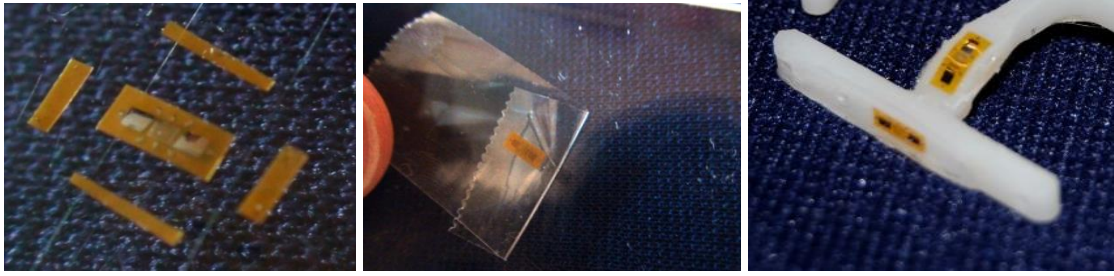


**Figure 5-7** Left: The strain gage is trimmed to dimensions just outside the grid area allowing the gage to fit of each of the spring element's measurement sections; Center: PCT-2M Gage Installation tape is laid over the gage and peeled upwards removing the gage from the cutting surface; Right: Strain gages adhered to the anterior measurement arm.

**Step 3:** Surface Conditioning and Neutralizing. M-Prep Conditioner A was applied repeatedly to the surface of the spring element (at the areas where strain gages are to be bonded) using a cotton tipped applicator. Application was ceased once the tip of the applicator was no longer discolored by the scrubbing. Applying the conditioner aided in cleaning the spring element's surface and removing dirt and other impurities. When clean, the surface was dried by wiping through the cleansed area with a single slow stroke of a gauze sponge. Next, the conditioned surface was neutralized via M-Prep Neutralizer 5A to bring the spring element's surface to a bonding pH of 7.0 to 7.5. This was completed by applying the neutralizer to the cleaned surface with a clean cotton-tipped applicator. The surface was then dried by wiping through the area with a gauze sponge.

**Step 4:** Strain Gage Alignment. With the grid and solder nodes facing upward on the glass surface, PCT-2M Gage Installation tape was laid over each gage (Figure 5-7). One edge of the tape was peeled upwards removing the gage from the work surface. Next, the

tape was placed on the designated area of the spring element making sure to align the gage along the desired measurement axis.

**Step 5: Strain Gage Adhesion.** Once a gage was aligned in its designated position, the installation tape was peeled halfway from the spring element exposing the bottom side of the strain gage. A thin coat of M-Bond 200 Catalyst was applied to the bottom of the gage. Immediately following application, one drop (approximately 0.1 mL) of M-Bond 200 was applied to the area beneath the gage. Using a finger or soft tool, the tape and corresponding strain gage was pressed to the geometry's surface applying firm pressure to the gage area. Pressure was maintained over the gage area for 5 minutes. After this period, the installation tape was peeled from the spring element leaving the strain gage adhered to the spring element's surface.

**Step 6: Tin Strain Gage Tabs.** PCT-2M Gage Installation tape was laid over each gage grid to protect from excess solder. After covering, each connection tab of the strain gage was tinned (Tinning refers to depositing solder to the strain gage solder tabs).

**Step 7: Wire Connection.** Three 336-FTE three stranded wires were cut into 6' segments. At one end of the wire, approximately 1" of the braided wire was unwound for soldering to the strain gages. After each wire was soldered to its respective strain gage, the wires were harnessed to the top of the transducer using 3-0 silk suture pictured in the left and right of Figure 5-8.

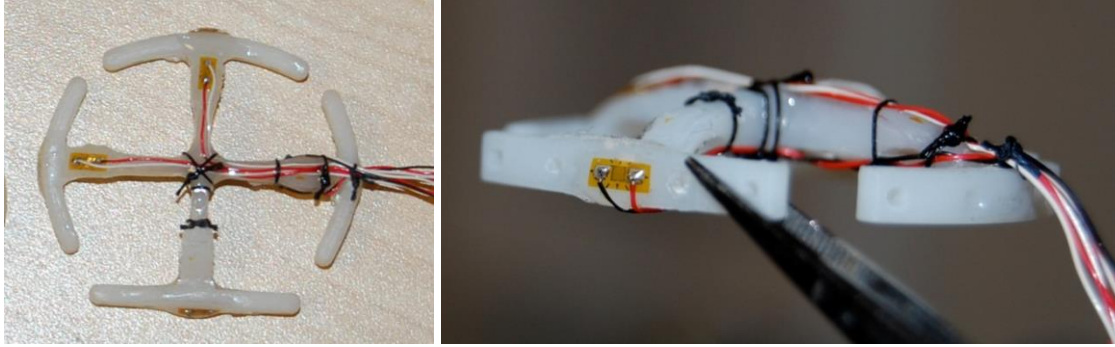


**Figure 5-8** Left: top view of the transducer with wires harnessed to the geometry's surface using 3-0 suture; Right: isometric view of the transducer after wires have been connected and harnessed.

**Step 8:** Rosin Removal. M-Line Rosin Solvent was used to remove excess rosin from the soldered areas of each strain gage. The solvent was lightly brushed across each gage then wiped dry with a clean cotton applicator.

**Step 9:** Strain Gage Surface Coating. Loctite® M-31CL™ Hysol® Medical Device Epoxy was applied in a thin coat (<0.5 mm) over each strain gage and solder nodes. Adhesive was allowed to cure for 24 hours. After the curing period, passages for suture on the measurement arms were checked and cleared of excess epoxy.

**Step 10:** Coating for Moisture Protection. One layer (<0.5 mm) of nitrile rubber was applied over each strain gage, solder nodes, and proximal wire. After 45 minutes of curing, the gage areas were checked for visible gaps (Center image of Figure 5-9). Any gaps found were re-layered and allowed an additional 45 minutes to cure.

**Step 11:** Exit wire harness. All wires leaving the transducer were placed within a 1/8" inner diameter heat shrink tube. A heat gun was used to shrink the tube onto the wire.

3140 RTV Silicone Rubber was used to seal the gap between the heat shrink and transducer to prevent blood from entering the wire harness during experimentation.

**Step 12: Measurement Arm Cushion.** To prevent annular irritation and/or tearing during implantation, a thin 3140 RTV Silicone Rubber layer was applied to the lateral faces of each measurement arm (Center and right image in Figure 5-9). On top of this layer, a High Purity Silicone Rubber Sheet (0.005” thickness) was placed to provide a uniform and flat surface.



**Figure 5-9 Left: Strain gage coated with epoxy (Step 9); Center: strain gages coated with nitrile rubber (Step 10); Right: application of 3145 silicone with the measurement arm cushions in place (Step 12).**

**Step 13: Additional Moisture and Mechanical Protection.** Dow Corning 3145 Silicone Adhesive was applied over each of the gages over the nitrile rubber coating. A thin coat (<1 mm) was applied and allowed to cure for 48 hours. Note: some experimental images do not picture this coating because this step was not introduced until 4 animal studies had been completed (normal animals 1 & 2 and chronic IMR animals 1 & 2).

### **5.1.5 Transducer Calibration**

To enable the measurement of planar mitral annular forces, the electrical outputs of the strain gages adhered to the transducer spring element were calibrated within a well-defined calibration apparatus (Figure 4-1). The calibration apparatus possessed the ability to impose septal-lateral and transverse forces either independently or in concert. During calibration, the septal-lateral loading mechanism was used to calibrate both the septal-lateral and transverse measurement arms. Based on previous studies, each transducer was calibrated from 0 to 8.4 N (in 1.2 N increments) for 7 independent runs while submerged in a 37°C water bath to mimic the physiologic temperature of the ovine subjects.

### **5.1.6 Assessing Transducer Accuracy and Precision**

The accuracy and precision of the transducer was assessed. After calibration, the resulting calibration value was used to test the transducer. The transducer was repositioned in the calibration apparatus and was loaded from 0 to 8.5 N in both measuring directions for 6 independent trials. During these trials, the measured and true force was compared and the 95% confidence interval determined.

### **5.1.7 Assessing Measurement Errors**

To evaluate the presence of measurement arm cross-talk, the device was secured within the calibration apparatus and tested at various combinations of radial forces. To test the relative contribution of annular shearing, the device was held and shear moment applied to each measurement arm. During ventricular diastole, the mitral valve opens and flow is allowed to both passively and actively enter the left ventricle. When the transducer is



implanted, flow must pass around the transducer's cross-members to fill the left ventricle. This diastolic flow has the potential to impart a force on the transducer affecting the magnitude of forces measured. Since these forces cannot be isolated during ovine experimentation, the transducer is implanted to a static mitral annulus within the Georgia Tech Left Heart Simulator. To match the peak transmitral diastolic flow rates in-vivo, the transducer forces were assessed at the following steady flow rates: 0, 5, 10 (sheep), 15 (human), 20, and 30 L/min.

### **5.1.8 Experimental Protocol**

Healthy and chronic IMR ovine animals (N=13) were intubated, anesthetized, and ventilated with isoflurane (1.5% to 2%) and oxygen. Surface electrocardiogram and arterial blood pressure was monitored. Cardiopulmonary bypass was initiated. After establishment of bypass, a left atriotomy was performed. Eight 2-0 Ethibond Exel Polyester sutures (Ethicon, Piscataway, NJ) were passed through the mitral annulus in positions corresponding to suture passages within the transducer's measurement arms. These sutures were secured through these passages and consistently resulted in firmly securing the device to the mitral annulus. Visual inspection was used to verify transducer placement and orientation within the mitral annulus (Figure 5-10).

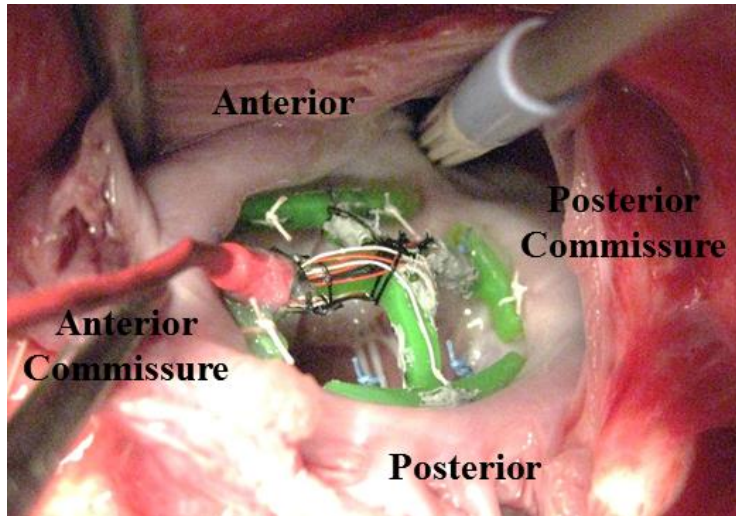


**Figure 5-10 Transducer implanted in the mitral annulus of a healthy ovine animal.**

Following separation from cardiopulmonary bypass, epicardial echocardiography was completed. A high-fidelity pressure transducer (SPR-3505; Millar Instruments, Houston, TX) was passed percutaneously into the LV through the femoral artery for continuous measurement of LV Pressure (LVP). Surface electrocardiogram, LVP, and arterial pressure (Hewlett-Packard 78534C monitor; Hewlett-Packard Inc, Santa Clara, CA) were monitored continuously. Upon establishing baseline hemodynamics (90 mmHg peak LVP, 4.0 L/min cardiac output), forces resulting from mitral annular contraction were measured within the post-cardioplegic heart.

To understand the effects of variations in peak LVP, forces were recorded in 1 minute intervals for cardiac cycles with peak LVP of 125, 150, 175, and 200 mmHg. Elevated levels of LVP were achieved via intravenous injection of norepinephrine. After successful measurement of all endpoints, animals were euthanized with 1 g thiopental and 80 mEq potassium-chloride. Hearts were explanted and opened to verify placement and firm anchoring of the device to the mitral annulus.

### **5.1.9 Data Acquisition**

Mitral annular forces were continuously acquired using a compact Data Acquisition System (cDAQ 9174) and strain gauge bridge module (NI 9237; National Instruments). LVP was measured from the Millar pressure catheter's control unit using an analog voltage module (NI 9215; National Instruments). Forces and LVP were continuously monitored and recorded in 1 minute intervals using a custom-built LabVIEW program (National Instruments) at 1613 Hz. This rate was sufficient for force measurement as well as for the determination of the peak rate increase of force with time ( $dF/dt$ ) during isovolumetric contraction.

### **5.1.10 Data Processing and Experimental Endpoints**

All acquired data were processed offline using a custom Matlab program (See Appendix E) (Mathworks, Natick, MA). Force data corresponding to ten consecutive cardiac cycles reaching a peak LVP of 90, 125, 150, 175, and 200 mmHg were isolated for analyses. From these cyclic data sets, septal-lateral and transverse forces were computed as the change from their minimum diastolic value to maximum systolic value. The peak rate change of force ( $dF/dt$ ) with time during isovolumetric contraction was additionally determined. The computed cyclic forces and  $dF/dt$  were averaged over the 10 consecutive cardiac cycles and are presented in Appendix A. This analysis was repeated for each animal and peak level of LVP. All results are reported as a mean  $\pm$  1 standard deviation.

### **5.1.11 Statistical Analysis**

Measured forces and rates of force change with time were checked for normality using the Anderson-Darling test. Changes in force and  $dF/dt$  with increasing levels of afterload within both the control and chronic IMR group were tested using repeated measures analysis of variance (ANOVA). If a significant effect was revealed, a Dunnett's post hoc was used to determine if forces measured at elevated levels of LVP were statistically greater than those measured at baseline conditions. To determine if differences in force and  $dF/dt$  existed between the healthy and chronic IMR group, a between groups repeated measures ANOVA test was used. If a significant difference was revealed, a conservative Bonferroni post hoc test was used to determine at which levels of ventricular afterload the differences exist. All statistical tests were completed using Minitab 16 (Minitab Inc, State College, PA).

## **5.2 Specific Aim 2 Methods**

### **5.2.1 Annuloplasty Ring Stress Transducer**

#### 5.2.1.1 Ring Stress Transducer Design

A novel transducer was developed to measure in- and out-of-plane bending stresses endured by an annuloplasty ring from implantation and cyclic contraction of the mitral annulus. Similar to the shape of the native annulus, the ring's core was designed to possess a kidney-shaped profile and was fabricated from 6-AL 4V titanium. This lower modulus alloy provided potential long-term biocompatibility and an excellent linear-elastic element for strain gage measurements. The ring's outer dimensions were based on

mitral annular sizes measured in a healthy ovine model (Figure 5-10) [41], while the ring's thickness was constrained to the dimensions of the miniature strain gages to be adhered to the ring's surface (EA-031DE-350, Vishay Micro-Measurements, Malvern, PA) (Figure 5-11). These gages have a measurable range of  $\pm 3\%$  strain and minimum measurable value of approximately 0.1 microstrain.

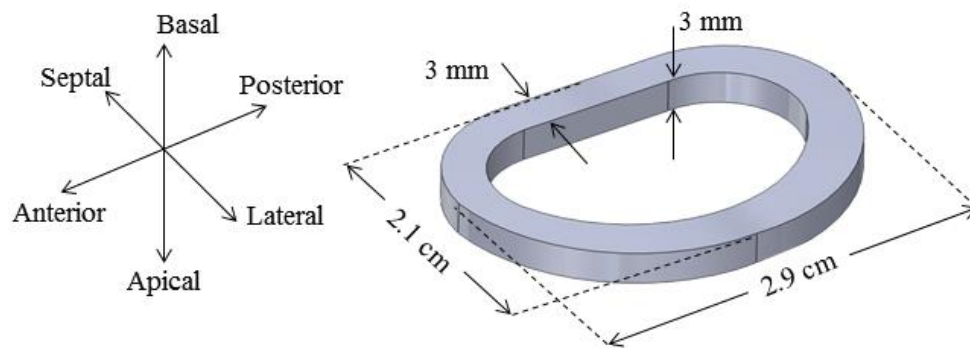


**Figure 5-11 Anatomical directions and relative dimensions of the annuloplasty ring stress transducer's titanium core.**

#### 5.2.1.2 Ring Stress Transducer Fabrication

The materials required to fabricate the annuloplasty ring stress transducer can be reviewed in Table 4-2. Using the specified materials, the ring stress transducers were fabricated as follows:

**Step 1: Surface Preparation:** The surface of the titanium ring was degreased using CSM-2 Degreaser. Degreaser was wiped from the ring's surface using gauze sponges until no discoloration of the sponges was observed. Following degreasing, the ring surface was wetted with M-Prep Conditioner A and subsequently sanded (400 grit). Following

sanding, the surface was washed with more M-Prep Conditioner A and then wiped dry with a gauze sponge. When dry, liberal amounts of M-Prep Neutralizer 5A was applied to the spring element. The surface of the spring element was scrubbed with a cotton-tipped applicator until no discoloration of the applicator was observed. At this point, physical handling of the spring element was minimized such that the neutralized surface was not contaminated with particulate or grease from fingers or objects (tweezers, hemostats, etc.).

**Step 2: Strain Gage Preparation.** 16 strain gages were prepared to construct 8 half-bridge circuits. Each half-bridge consisted of 2 strain gages and 1 lead wire terminal. For each half-bridge, 2 strain gages were removed via tweezers from their packaging and laid on a clean glass surface. Excess gage material was removed. One lead wire terminal was trimmed, cut in half, and laid on the cutting surface. With the strain gages and lead wire terminal arranged as pictured in Figure 5-12, PCT-2M Gage Installation tape was laid over each of the strain gages in preparation for strain gage positioning on the ring's surface.



**Figure 5-12 Image of the strain gages and lead wire terminal ready for strain gage positioning.**

**Step 3: Strain Gage Positioning.** A pen was used to mark the assigned position of each strain gage to be adhered to the titanium ring. These locations included the septal, lateral, and commissural ring segments on both the in-plane and out-of-plane surfaces of the ring. Single strain gages (without the lead wire terminal) were chosen to be placed on the ring's outer and top surfaces. This was done to minimize the number of wires near the ring's outer suture cuff. Once the positions were chosen, one edge of the tape covering the strain gage was peeled upwards removing the gage from the work surface. Next, the tape was placed on the designated area of the ring making sure to align the gage along the desired measurement axis. This was completed for each of the strain gage locations.

**Step 4: Strain Gage Adhesion.** Once each gage was aligned in their designated position, the installation tape was peeled halfway from the spring element exposing the bottom side of the strain gage. The exposed backing of the strain gage (and/or lead wire terminal) was coated with a thin layer of M-Bond 43-B. The adhesive applicator was not allowed to touch the tape mastic. The adhesive on the gage backing was allowed to air-dry, by solvent evaporation, for 30 minutes at room temperature.

Following the evaporation phase, the gage/terminal assembly was returned to its original position over the penned positioning mark (Step 4). A thick silicone gum pad and a metal backup plate (GT-14) was placed over the gage/terminal areas and clamped using spring clamps. The clamped gage/specimens were then placed into a cool oven whose temperature was raised to 375 °F. Once reaching this ultimate temperature, the ring with bonded strain gages were allowed to cure for 2 hours. Upon completion of the curing cycle, the oven temperature was allowed to drop to 250 °F before removing the ring.

**Step 5:** Tin Strain Gage Solder Tabs and Lead Wire Terminals. PCT-2M Gage Installation tape was laid over each gage grid to protect from excess solder. After covering, each connection tab of the strain gage and lead wire was tinned as pictured in Figure 5-13.

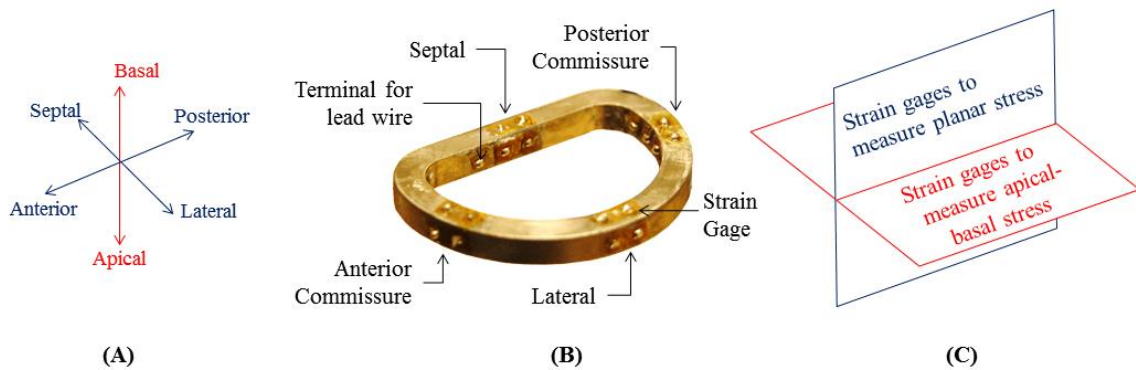


**Figure 5-13 (A) Anatomical directions, (B) Image of the titanium annuloplasty ring core with bonded strain gages and lead wire terminals tinned, and (C) Planar orientation of the mounted strain gages with labels indicating their measurement direction.**

**Step 6:** Half Bridge Strain Gage Wire Connection. Three 336-FTE three stranded wires were cut into 6' segments. At one end of the wire, approximately 1" of the braided wire was unwound for soldering to the strain gages. The wiring diagram and finished wired transducer are pictured in Figure 5-14.



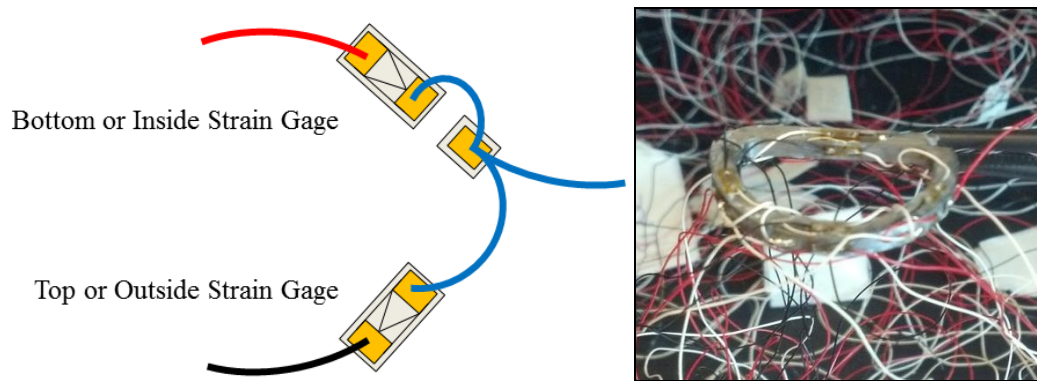


**Figure 5-14 Left: Half-bridge configuration with strain gage, lead wire terminal, and wires shown (Note: Blue wire is actually white on the actual transducer); Right: Wired half-bridges.**

**Step 7: Rosin Removal.** M-Line Rosin Solvent was used to remove excess rosin from the soldered areas of each strain gage. The solvent was lightly brushed across each gage then was wiped dry with a clean cotton applicator.

**Step 8: Strain Gage Surface Coating.** Loctite® M-31CLTM Hysol® Medical Device Epoxy was applied in a thin coat (<0.5 mm) over each strain gage and solder nodes. The adhesive was allowed to cure for 24 hours (Figure 5-15).



**Figure 5-15 Left: Transducer's strain gages and lead wire terminals are coated in Loctite® M-31CLTM Hysol® Medical Device Epoxy (Step 8); Right: Following harnessing the transducer's wires (Step 12) , the entire transducer is dip-coated in synthetic rubber (Step 10).**

**Step 9: Wire Harnessing.** All of the strain gage wires were harnessed and then fed through 1.5 m segments of wire heat shrink at each of the rings trigonal segments. Following wire harnessing, the wire heat shrink was heated and shrunk to sheathed wires.

**Step 10: Coating for Moisture Protection.** The ring was coated with synthetic rubber (Figure 5-15) to provide a secondary moisture barrier and an anchoring material for the suture cuff (Plasti Dip, Performix, Blaine, MN).

**Step 11: Suture Cuff Fabrication.** To complete the suture cuff, cardiovascular polyester fabric (thickness  $0.61 \pm 0.10$  mm) (611 Double Velour Fabric, C.R. Bard, Murray Hill, NJ) was tightly sewn around the ring to allow for implantation similar to commercial annuloplasty rings (Figure 5-16). After fabrication, the ring exhibited a  $6.9 \text{ cm}^2$  outer area, 2.6 cm septal-lateral dimension, 3.3 cm transverse diameter, and thickness of 0.7 cm. While the outer dimensions of the ring were comparable to a size 32 mm Carpentier-Edwards Physio ring, the inner orifice area was  $1.6 \text{ cm}^2$ .

#### 5.2.1.3 Experimental Protocol

One Dorsett Hybrid sheep (45 kg) was intubated, anesthetized, and ventilated with isofluorane (1.5% to 2%) and oxygen. Surface electrocardiogram and arterial blood pressure was monitored. After establishment of cardiopulmonary bypass, a left atriotomy was performed. Ten 2-0 Ethibond Exel Polyester sutures (Ethicon, Piscataway, NJ) were placed in the subjects mitral annulus and through the cuff of the instrumented

annuloplasty ring (Figure 5-16A). Prior to lowering and securing the ring into the mitral annulus, each of the ring's strain gage bridges was zeroed. The annular sutures were secured to the ring in the following order: left fibrous trigone, right fibrous trigone, then each remaining suture proceeding clockwise from the left fibrous trigone (Figure 5-16B). After implantation, the strains imparted on the ring by the flaccid mitral annulus were recorded.

Following atrial closure, degassing, and separation from cardiopulmonary bypass; continuous wave Doppler echocardiography was completed (Phillips ie33, Phillips, Amsterdam, Netherlands). A high-fidelity pressure transducer (SPR-3505; Millar Instruments, Houston, TX) was passed percutaneously into the LV through the femoral artery for continuous measurement of LV Pressure (LVP). Surface electrocardiogram (EKG), LVP, and arterial pressure (Hewlett-Packard 78534C monitor; Hewlett-Packard Inc, Santa Clara, CA) were monitored. Upon establishing baseline hemodynamics (90 mmHg peak LVP, 4.0 L/min cardiac output), cyclic ring strains were measured within the post-cardioplegic heart. After successful measurement of all endpoints, the subject was euthanized with 1 g thiopental and 80 mEq KCl. The heart was removed and opened to verify placement and firm anchoring of the device to the mitral annulus (Figure 5-16C).

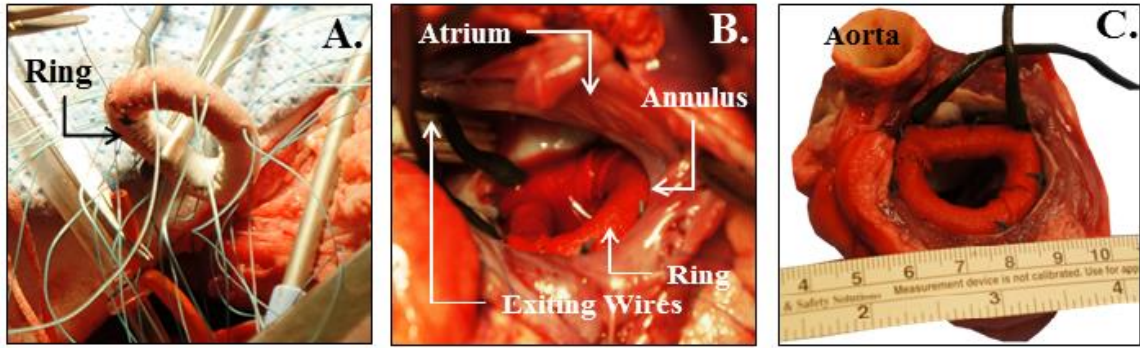


**Figure 5-16 (A) Ten 2-0 sutures are placed through the suture cuff of the annuloplasty ring transducer for implantation, (B) While on cardiopulmonary bypass the transducer is implanted to the mitral annulus, (C) Post-experimentation, the left atrium is removed and the transducer was inspected for firm anchoring to the mitral annulus.**

#### 5.2.1.4 Data Acquisition

Annuloplasty ring strains and LVP were continuously monitored using a compact Data Acquisition System (cDAQ 9174), strain gage bridge module (NI 9237), and analog voltage module (NI 9215) (National Instruments) at 1613 Hz. Ring strains, LVP, and EKG were monitored and recorded in 1 minute intervals using a custom-built program within the LabVIEW software program (National Instruments).

#### 5.2.1.5 Data Analysis and Experimental Endpoints

Recorded data were processed offline using a custom MATLAB program (See Appendix E) (Mathworks, Natick, MA). Within this program, measured strains were converted to stress using the elastic modulus of ring's titanium core (114 GPa). From the processed data, 10 consecutive cardiac cycles reaching a peak LVP of 90 mmHg were isolated for further analysis. From this cyclic data set, ring stresses at each ring position were computed as the change from their minimum diastolic value to maximum systolic value.

All ring stresses and LVP were averaged over the 10 consecutive cardiac cycles and reported as a mean  $\pm$  1 standard deviation.

## **5.2.2 Annuloplasty Ring Suture Force Transducer**

### 5.2.2.1 Suture Force Transducer Design

Novel strain gage transducers were designed to isolate the tensile forces in individual sutures along an annuloplasty ring (Figure 5-13A). The spring element of each transducer was designed to consist of an annuloplasty ring mounting bracket and a suture force measurement arm (Figure 5-17A and 5-17B). The four holes in the mounting bracket allowed for each transducer to be directly sutured to the annuloplasty ring using 2-0 Ti•Cron<sup>TM</sup> (Covidien, Mansfield, MA). The spring element's measurement arm was designed to replace the function of the ring's suture cuff. During implantation, mattress sutures are passed through and tied to the top of the spring element's measurement arm in the exact method used to secure sutures to a ring's suture cuff (Figure 5-17C and 5-17D).

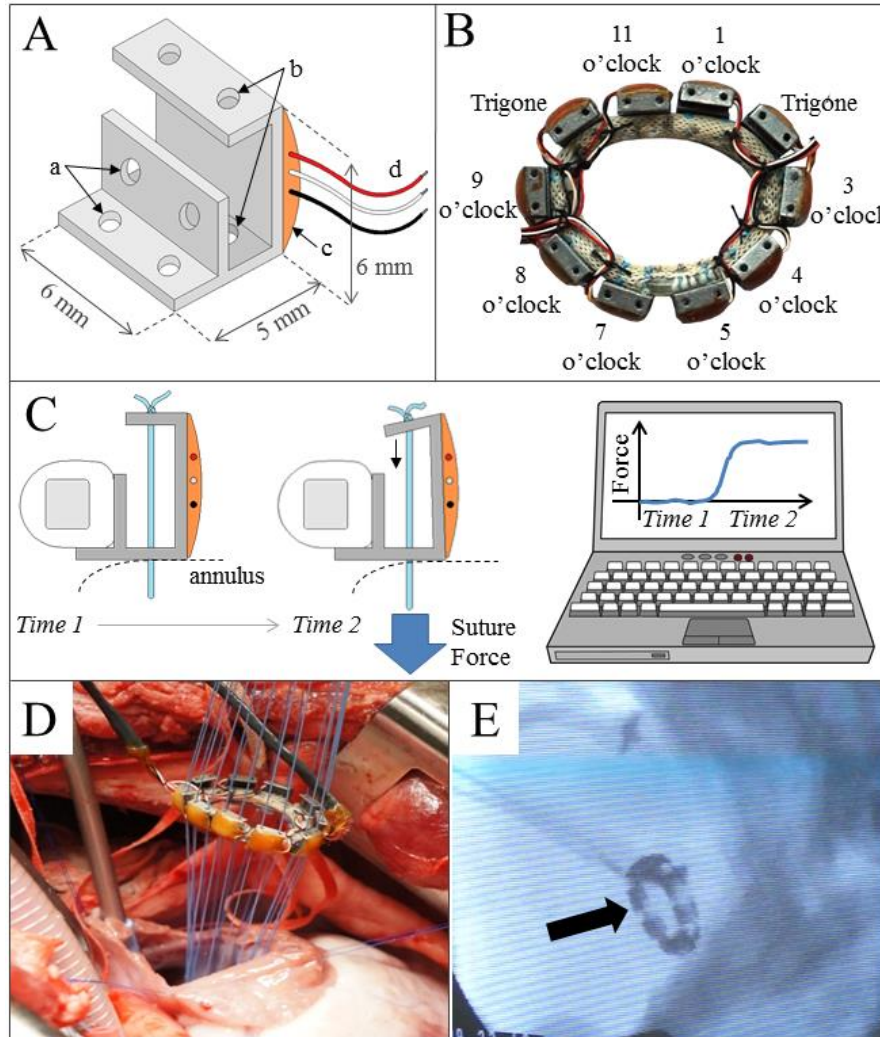


**Figure 5-17 (A) Schematic of transducer with (a) mounting holes for ring mounting, (b) mattress suture passages, (c) strain gage for force measurement, and (d) exiting wires. (B) Completed transducer. (C) Schematic of implanted ring with suture induced transducer deformation and force measurement. (D) Device implantation. (E) Implanted transducer imaged using fluoroscopy.**

Combining finite element analysis (SolidWorks, Waltham, MA) with forces previously measured, the dimensions of spring element were optimized for suture force measurement (Figure 5-17A). This optimization was completed in a similar fashion to the steps taken in the annular force transducer. Based on these analyses, the spring element was manufactured from 316L stainless steel (Fineline Prototyping, Raleigh, NC). This

material was chosen for its excellent biocompatibility and structural strength, and also for its reliability as an excellent linear-elastic material for strain gage measurements.

The ability of the developed transducers to measure suture forces is made possible by the adhered strain gages. As demonstrated in Figure 5-17C, forces applied to a suture result in the bending and deformation of the transducer's measurement arm. Since the strain gages are adhered to the transducer, the strain gages deform with the measurement arm. Strain gage deformations result in changes in the gage's electrical output. Through calibration, changes in electrical output are correlated to known forces providing the ability to convert measured electrical outputs to force measurements.

#### 5.2.2.2 Suture Force Transducer Fabrication

Using the materials outlined in Table 4-3, the annuloplasty ring suture force transducers were fabricated as follows:

**Step 1: Surface Preparation:** The surface of the spring element was wetted with M-Prep Conditioner A and subsequently sanded (400 grit). Following sanding, the surface was washed with more M-Prep Conditioner A and then wiped dry with a gauze sponge. When dry, liberal amounts of M-Prep Neutralizer 5A was applied to the spring element. The surface of the spring element was scrubbed with a cotton-tipped applicator until no discoloration of the applicator was observed. At this point, physical handling of the spring element was minimized such that the neutralized surface was not contaminated with particulate or grease from fingers or objects (tweezers, hemostats, etc.).

**Step 2: Strain Gage Preparation.** Strain gages were removed via tweezers from their packaging and laid on a clean glass surface. Excess gage material was removed.

**Step 3: Strain Gage Alignment.** With the grid and solder nodes facing upward on the glass surface, PCT-2M Gage Installation tape was laid over each gage. One edge of the tape was peeled upwards removing the gage from the work surface. Next, the tape was placed on the designated area of the spring element (Left of Figure 5-18) making sure to align the gage along the desired measurement axis.

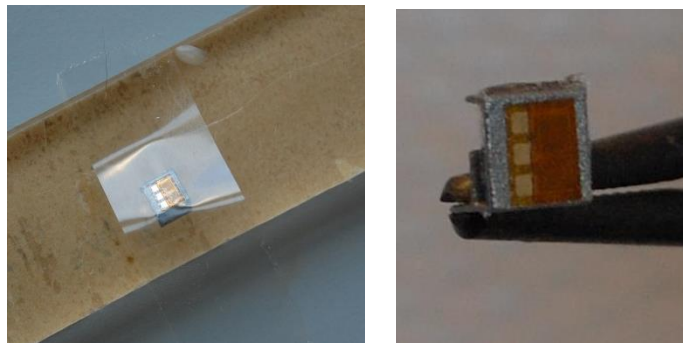


**Figure 5-18 Left: Strain gage alignment (Strain gage is not adhered to the surface of the transducer spring element); Right: Strain gage is adhered to the spring element.**

**Step 4: Strain Gage Adhesion.** Once a gage has been aligned in its designated position, the installation tape was peeled halfway from the spring element exposing the bottom side of the strain gage. A thin coat of M-Bond 200 Catalyst was applied to the bottom of the gage. Immediately following application, one drop (approximately 0.1 mL) of M-Bond 200 was applied to the area beneath the gage. Using a finger or soft tool, the tape and corresponding strain gage was pressed to the geometry's surface applying firm pressure to the gage area. Pressure was maintained over the gage area for 5 minutes.



After this period, the installation tape was peeled from the spring element leaving the strain gage adhered to the geometry's surface (Right of Figure 5-18).

**Step 5: Tin Strain Gage Solder Tabs.** PCT-2M Gage Installation tape was laid over each gage grid to protect from excess solder. After covering, each connection tab of the strain gage was tinned as pictured in the left of Figure 5-19.

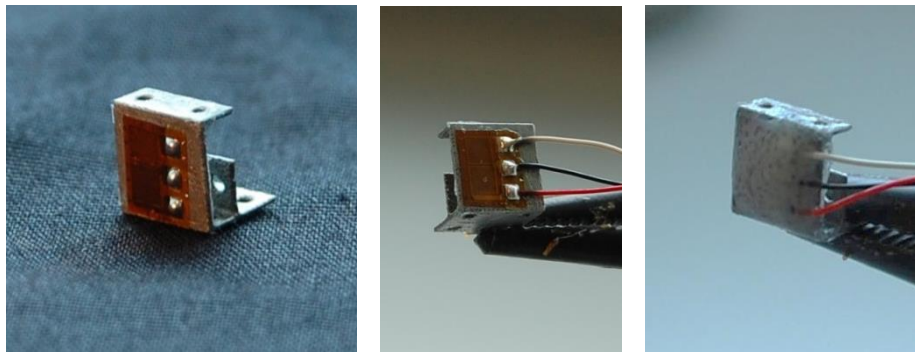


**Figure 5-19 Left: Tinned solder nodes on a strain gage; Center: Wired strain gage; Right: Strain gage surface coating with epoxy.**

**Step 6: Half Bridge Strain Gage Wire Connection.** Three 336-FTE three stranded wires were cut into 6' segments. At one end of the wire, approximately 1" of the braided wire was unwound for soldering to the strain gages (Center of Figure 5-19).

**Step 7: Rosin Removal.** M-Line Rosin Solvent was used to remove excess rosin from the soldered areas of each strain gage. The solvent was lightly brushed across each gage then was wiped dry with a clean cotton applicator.

**Step 8: Strain Gage Surface Coating.** Loctite® M-31CLTM Hysol® Medical Device Epoxy was applied in a thin coat (<0.5 mm) over each strain gage and solder nodes. The adhesive was allowed to cure for 24 hours (Right of Figure 5-19).

**Step 9: Coating for Moisture Protection.** One layer (<0.5 mm) of nitrile rubber is applied over each strain gage, solder nodes, and proximal wire. After 45 minutes of curing, the gage areas are checked for visible gaps. Any gaps found are re-layered and allowed additional 45 minutes to cure (Figure 5-21).

#### 5.2.2.3 Suture Force Transducer Calibration

Based on previous studies, all transducers were calibrated from 0-10 N for 5 independent trials [75,76]. To calibrate the transducers, a loose loop of suture was passed through the transducer's measurement arm and through a table with two holes positioned to match the device's mattress suture passages. The loop was knotted tightly by six square knots to prevent any slippage during trials. Weights ranging from 0.2-10 N (were suspended from the transducer's suture loop beneath the table in a sequential fashion. Weights included 20 g, 50 g, 100 g, 200 g, 500 g, and 1 kg. Correlations between applied forces and measured output voltages resulted in coefficients of determination exceeding 0.99.

#### 5.2.2.4 Assessing Transducer Accuracy and Precision

Following calibration of the initial fabricated transducers, the derived calibration constants were used to assess transducer accuracy and precision. Transducers were

repositioned in the calibration apparatus and were loaded from 0 to 10 N for 3 independent trials. Following these trials, the measured and true force was compared.

#### 5.2.2.5 Instrumenting the Annuloplasty Ring with the Suture Transducers

Once calibrated, ten suture force transducers were attached to size 24, 26, 28, and 30 Physio™ rings (Edwards Lifesciences, Irvine, CA). Transducers were sutured to the ring as depicted in Figure 5-20. Using the pictured method, transducers were placed at each trigonal location and at near symmetric locations around the ring (Figure 5-21). In this configuration, 4 transducers were placed on the anterior portion of the ring with the remaining 6 on the posterior circumference. Since the transducers sit external to the ring's suture cuff, the outer dimensions of the annuloplasty ring were increased by one Physio™ ring size.

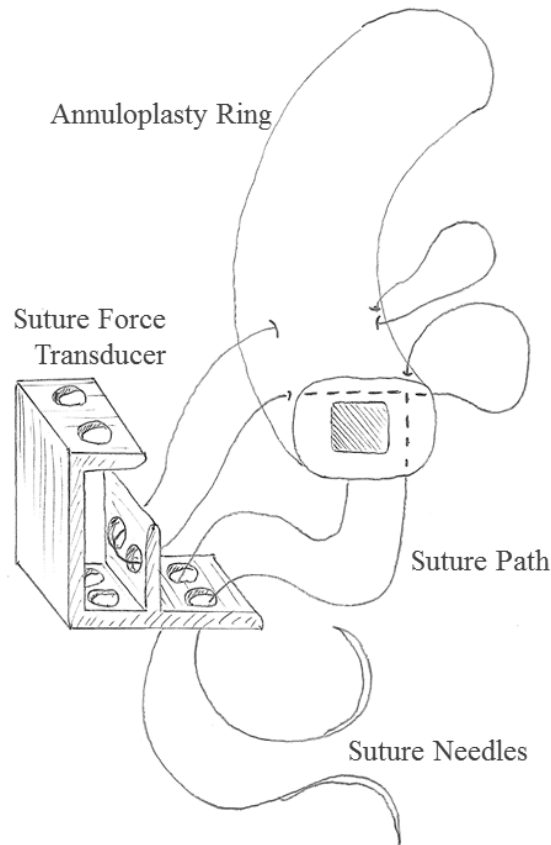


**Figure 5-20 Method used to secure a suture transducer to the annuloplasty ring.**



**Figure 5-21 Photograph of a size 24 Physio™ ring instrumented with 10 suture force transducers.**

#### 5.2.2.6 Experimental Protocol

Healthy Dorsett hybrid sheep were intubated, anesthetized, and ventilated with isoflurane (1.5% to 2%) and oxygen. Surface electrocardiogram and arterial blood

pressure was monitored. After establishment of cardiopulmonary bypass, a left atriotomy was performed. Ten 21 mm 2-0 Ti-Cron™ sutures (Covidien, Mansfield, MA) were placed in the mitral annulus and through the mounting holes of the transducers' measurement arms (Figure 5-17C). Prior to lowering and securing the ring into the mitral annulus, each of the transducers was zeroed to establish a zero force baseline. The annular mattress sutures were then secured to the ring in the following order: left fibrous trigone, right fibrous trigone, then each remaining suture proceeding clockwise from the left fibrous trigone. Each suture was secured with 5 surgeon's knots. After securing the final suture, the suture forces resulting from implanting the ring to the flaccid mitral annulus were recorded.

Following left atrial closure and separation from cardiopulmonary bypass; a high-fidelity pressure transducer (SPR-3505; Millar Instruments, Houston, TX) was passed through the femoral artery to the LV for continuous measurement of LVP. Surface electrocardiogram, LVP, and arterial pressure (Hewlett-Packard 78534C monitor; Hewlett-Packard Inc, Santa Clara, CA) were monitored. Upon establishing baseline hemodynamics (100 mmHg peak LVP, 4.0 L/min cardiac output), cyclic suture forces were measured within the post-cardioplegic heart. Continuous wave Doppler echocardiography was used to quantify the mean diastolic transmitral gradient. To evaluate the effects of increasing afterload, suture forces were recorded continuously for cardiac cycles exhibiting a peak LVP of 125 and 150 mmHg. Elevated LVP was achieved via intravenous injection of epinephrine. After successful force measurement, animals were euthanized with 1 g thiopental and 80 mEq KCl. The heart was explanted and opened to verify secure anchoring of the device to the annulus.

#### 5.2.2.7 Data Acquisition

Suture forces and LVP were continuously acquired using a compact Data Acquisition System (cDAQ 9174), strain gage bridge modules (NI 9237), and analog voltage module (NI 9215) (National Instruments) at 1613 Hz. Suture forces and LVP were monitored and recorded using a custom LabVIEW program (National Instruments).

#### 5.2.2.8 Data Processing and Experimental Endpoints

Recorded data were processed offline using a custom MATLAB program (See Appendix E) (Mathworks, Natick, MA). Cyclic force data corresponding to ten consecutive cardiac cycles reaching a peak LVP of 100, 125, and 150 mmHg were isolated for analyses. From these cyclic data sets, cyclic suture forces were computed as the change from their minimum diastolic value to maximum systolic value. The computed cyclic forces were averaged over the 10 consecutive cardiac cycles and are presented in Appendix B. This analysis was repeated for each animal and peak level of LVP. All results are reported as a mean  $\pm$  1 standard deviation. Due to the limited sample size, no statistical analyses were conducted.

## 5.3 Specific Aim 3 Methods

### 5.3.1 Assessing the Accuracy of the Georgia Tech Left Heart Simulator

#### 5.3.1.1 Experimental Protocol

Control (N=6) and chronic IMR ovine subjects (N=6) were intubated, anesthetized and ventilated with isoflurane and oxygen. Surface electrocardiogram and arterial blood pressure were monitored. A right thoracotomy was performed. Upon the heart's exposure, epicardial Doppler echocardiography images were obtained to evaluate MR (Phillips IE33 Matrix, Phillips, Amsterdam, Netherlands). MR was graded on a 0 to 4+ scale, where 0 represented no MR and 4+ represented severe MR with reversal of pulmonary vein flow.

Using published techniques, 2 mm hemispherical piezoelectric transducers (Sonometrics, London, Ontario) were localized to the mitral annulus (N=12), A2 anterior mitral leaflet (N=5), and papillary muscles (N=2) and connected to a Series 5001 Digital Sonomicrometer (Sonometrics, London, Ontario) (Figure 5-22 and Figure 4-3). After weaning each subject from cardiopulmonary bypass, a high-fidelity pressure transducer ( $\pm 1$ mmHg) (SPR-3505; Millar Instruments, Houston, TX) was passed percutaneously into the LV through the femoral artery for continuous measurement of left ventricular pressure. Surface electrocardiogram, LVP, and arterial pressure (Hewlett-Packard 78534C monitor; Hewlett-Packard Inc, Santa Clara, CA) were monitored.

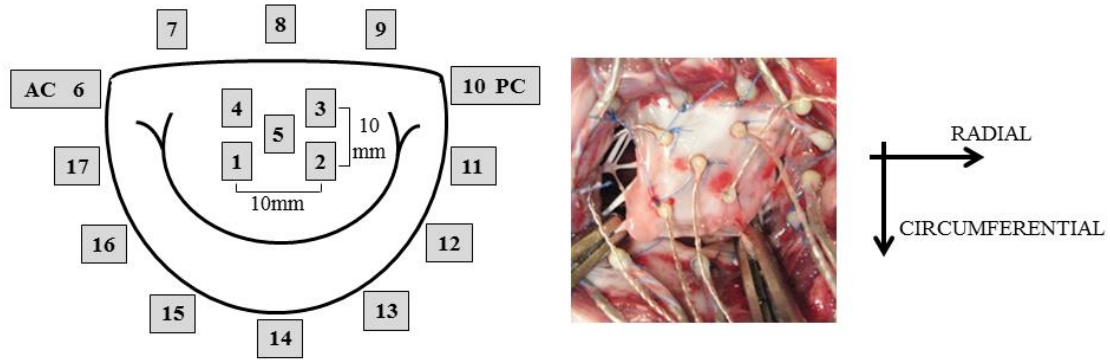


**Figure 5-22 Left: Geometric map of sonomicrometry crystals localized to the A2 anterior leaflet and mitral annulus; AC: Anterior Commissure, PC: Posterior Commissure; Right: in-vivo image of crystals localized to the mitral annulus and anterior leaflet with directions of strain shown (See Figure 4-3 for crystals localized to the papillary muscles).**

Upon establishing baseline ovine hemodynamics (100 mmHg peak LVP; 3.3 L/min cardiac output), the three-dimensional coordinates (resolution of  $\pm 0.01$  mm) of each sonometric transducer were recorded at 200 Hz with simultaneous measurements of LVP. Following experimental completion, animals were euthanized with 1 g thiopental and 80 mEq KCl. Hearts were explanted and the LV opened through the interventricular septum to quantify the infarct size as a percentage of the LV.

### 5.3.1.2 Mapping the Ovine Mitral Valve Geometry

Acquired data sets of the annular, leaflet, and papillary muscle positions as functions of time and LVP were used to map the ovine MV geometry and quantify leaflet strain in both healthy and chronic IMR animals. Peak systolic closure was assigned as the time point of peak LVP. At this time point, the annular and PM coordinates were used to determine the relative position of the PMs with respect to the annulus, annular area, annular orifice shape, annular-height-to-commissural-width ratio. These actions were



completed for both the healthy and chronic IMR animals to calculate relative changes in MV geometry for *in vitro* simulation.

#### 5.3.1.3 *In vitro* Experimental Protocol

Fresh ovine hearts were obtained and MVs excised (N=6) preserving their annular and subvalvular anatomy. MVs with an anterior leaflet height of 18-19 mm (as measured in our ovine animals (Table 6-8)), type 1 or 2 PMs [1], and with all leaflet chordae inserting directly into each PM were selected for experimentation. Selected MVs were sutured to the Georgia Tech Left Heart Simulator's annulus using a Ford interlocking stitch. For control conditions, the annulus was set to an area of 6.5 cm<sup>2</sup> and annular height to commissural width ratio of 15% as measured *in vivo* (Table 6-8). During valve suturing, care was taken to place each suture just above the valve's natural hinge and not through the leaflet tissue. Additionally, normal annular-leaflet geometric relationships were respected - the anterior leaflet occupied 1/3rd of annular circumference and commissures were aligned in the 2 and 10 o'clock positions.

Following suturing the MV to the prosthetic mitral annulus, a tissue dye (Thermo Scientific, Waltham, MA) was used to mark the anterior leaflet in a square grid. In this method, the mitral leaflets area allowed to hang from the annulus and dry for at least 40 minutes. During this period, the leaflets can be blotted with paper towel to assist in removing leaflet moisture. When dry, the atrial surface of the anterior leaflet's A2 cusp is marked with a 1.5 mm x 1.5 mm square array (9 dots in the array) using a blunted tip of a 17 mm needle. Using the aforementioned needle size, each of the dye markers were

approximately 0.5-1 mm in diameter. While the leaflet markers are drying (~30 minutes), the PMs and chordae are submerged in saline solution to maintain moisture.

After the dye grid on the anterior leaflet was completed, each PM was attached to the PM control rods. Each PM was carefully positioned and fine-tuned to establish the control MV geometry as previously described [104]. Transmitral ovine pulsatile conditions were simulated (3.3 L/min Cardiac Output, 120 beats/min, 100 mmHg transmitral pressure). Mitral coaptation was then inspected via echocardiography such that the anterior leaflet spanned approximately 2/3rds of the A2-P2 diameter and the coaptation length was approximately 4-5 mm as measured in our healthy animals (Table 6-8). If the control valve geometry conditions were successfully achieved, transmitral hemodynamics, 3D echocardiography (Philips ie-33), and dual camera high-speed images of the valve were acquired.

To simulate a chronic IMR MV geometry, the valve annulus was flattened and asymmetrically dilated per the mean valvular distortions measured in our chronic IMR animals (Table 6-8). The PMs were adjusted per the mean displacements observed between the healthy and chronic IMR animals. Based on this data, the posteromedial PM was displaced 4 mm laterally, 6 mm posteriorly, and 2 mm basally. The anterolateral PM was displaced 2 mm laterally, 1 mm anteriorly, and 1.5 mm apically. These displacements were consistent with previously published data [55]. After the displacement of each PM, transvalvular hemodynamics was established and experimental end-points recorded.

### 5.3.1.4 Quantifying Anterior Leaflet Strain *In vivo* and *In Vitro*

Sonomicrometry and tissue dye coordinates acquired in both the animal and bench experiments were used to compute the anterior leaflet strain. Using a custom MATLAB program (See Appendix E) (Mathworks, Natick, MA), biquintic finite element interpolation was used to fit a surface to the 3D anterior leaflet marker coordinates (Section 4.3.6) (Location of Program is in Appendix E). Generated surfaces were used to determine the mean radial and circumferential strains and strain rates endured by the anterior leaflet (Figure 5-23). Similar to previous studies, the referential leaflet strain configuration corresponded with the minimum LVP.

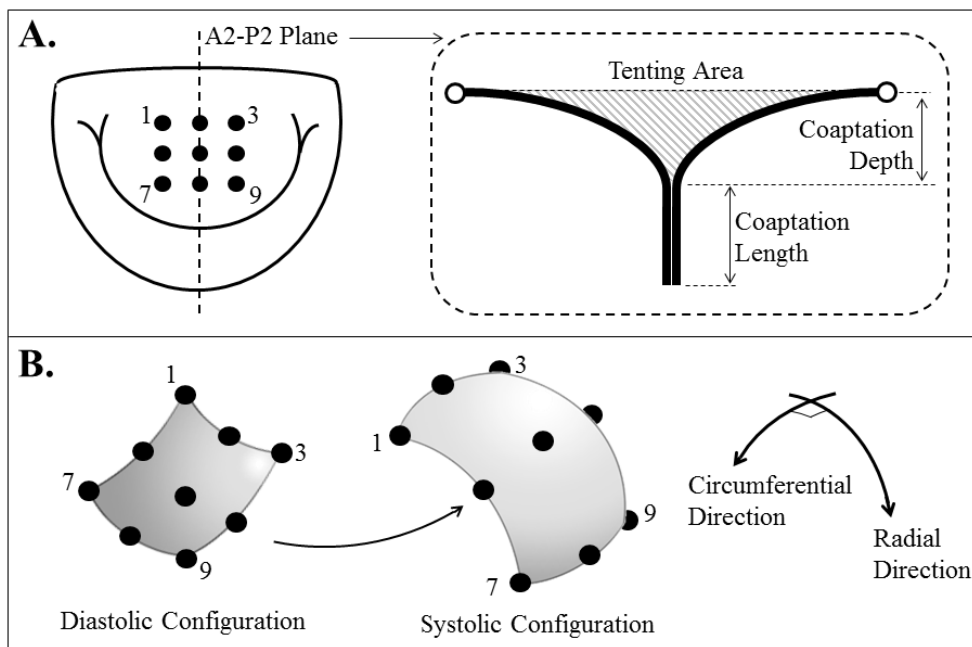


**Figure 5-23 (A) Schematic representation of the surgeon's view of the mitral valve with the A2-P2 echocardiography measurements of leaflet coaptation identified; (B) Direct linear transformation was used to calculate the radial and circumferential anterior leaflet strain using two high-speed cameras tracking nine fiduciary leaflet markers.**

#### 5.3.1.5 Data Processing

All *in vitro* hemodynamic data were processed offline within a custom MATLAB program (See Appendix E) and averaged over 10 consecutive cardiac cycles. *In vitro* regurgitation fractions were calculated as the total retrograde volume divided by the stroke volume. Echocardiography data were analyzed using Phillips QLab (v.7.0; Philips Healthcare; Andover, MA). Anterior leaflet strain was computed as outlined in Section 5.3.1.5.

#### 5.3.1.6 Statistical Analysis and Experimental Endpoints

To compare between animal groups and simulated conditions, a non-parametric Mann-Whitney U test was used. *In vitro* comparisons made between the control and chronic IMR conditions were completed with a Wilcoxon Signed Rank test. All statistical analyses were completed using SPSS 20 (IBM, Armonk, NY). End points are expressed as a mean  $\pm$ 1 standard deviation.

### **5.3.2 Evaluating the Effect of Undersized Annuloplasty on Subvalvular Tethering**

#### 5.3.2.1 Chordae Tendineae Selection and Instrumentation

Prior to each experiment, chordal force transducers were sutured directly to selected chordae tendineae to quantify cyclic tethering forces. Selected chordae included the anterior strut and posterior intermediary chords originating from both the anterolateral and posteromedial papillary muscles. In short, transducers were sutured directly to selected chordae using 17 mm RB-1 needle with 5-0 silk (Ethicon, Somerville, NJ) (Figure 5-24). Suture is passed directly above the transducer through the center of the

chord, then through the suture passage, then directly below the transducer through the chord as to not alter the native chordal length during suture knotting. Four surgeon's knots are tied within the slot of the transducer against the native chord in succession. Once a transducer is secured to the chord, the section of chordae located between the transducer's measurement arms is transected such that all tensile loading of the chord is transferred to the transducer.

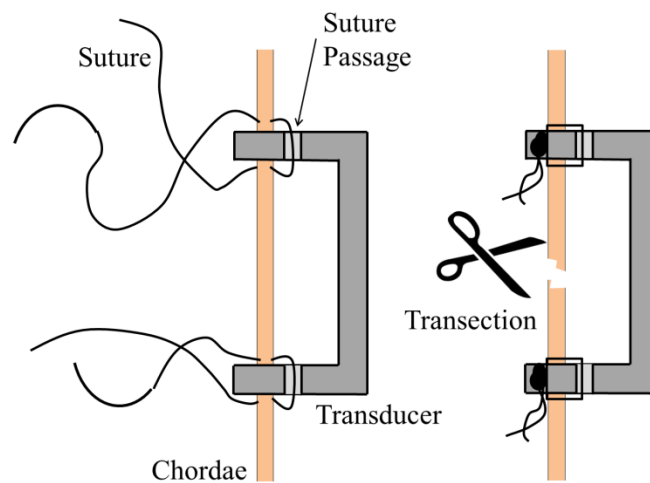


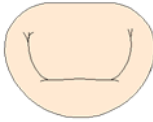
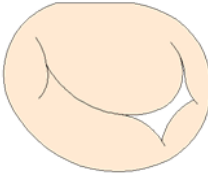
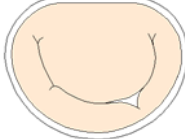
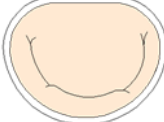
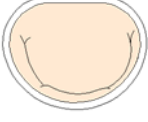
**Figure 5-24 Schematic representation of securing a chordal force transducer to a selected chordae tendineae.**

#### 5.3.2.2 Simulating Undersized Mitral Annuloplasty

Fifteen ovine MVs with an anterior leaflet height of 20-25 mm were utilized in this study. Anterior leaflet height has been demonstrated to correlate with commissural width and thus healthy annular area in more than 90% of cases [1]. If the selected MV was found to possess any mitral chordae that inserted directly in the LV wall, the valve was discarded and another MV was selected for experimentation. No additional screening criterion was used in mitral valve selection.

After suturing the excised MV to the simulator's mitral annulus, 4 chordae tendineae were instrumented with dedicated chordal force transducers as described in section 5.3.2.1. Following instrumentation, the MV was mounted into the simulator and the annulus was conformed to a size 30 Physio<sup>TM</sup> ring. Upon establishing human left heart hemodynamics (5.0 L/min cardiac output, 70 beats/min, 120 mmHg transmitral pressure), each papillary muscle was carefully positioned and fine-tuned to establish the control MV geometry. Mitral coaptation was inspected via echocardiography such that the anterior leaflet spanned approximately two-thirds of the A2-P2 diameter. When the control valve geometry conditions were successfully achieved, the experimental endpoints of transmitral flow, left atrial pressure, left ventricular pressure, 2D echocardiography (Philips ie-33 Matrix, Philips Healthcare, Andover, MA), and chordal forces were acquired.

To simulate chronic IMR due to an inferior myocardial infarction, the valve annulus was asymmetrically dilated to approximately 150% of the control valve area. The anterolateral papillary muscle was displaced 3 mm apically and 2 mm anteriorly, whereas the posteromedial papillary muscle was displaced 4 mm apically, 4 mm posteriorly, and 8 mm laterally. These changes were consistent with the geometric distortions measured and simulated in Specific Aim 3A. Papillary muscles were held in their displaced IMR positions for all levels of simulated annuloplasty (Figure 5-25). This was done to reflect the results of a previous porcine IMR study that demonstrated undersized Physio<sup>TM</sup> ring annuloplasty to not induce an overall pattern of PM relocation [121].

Condition	Control	IMR	Oversized Annuloplasty	True-Sized Annuloplasty	UMA
Annulus			 34 Physio	 30 Physio	 26 Physio
Papillary Muscles	Normal	IMR Configuration	—————→		

**Figure 5-25 Summary of experimental conditions progressing from control to ischemic mitral regurgitation (IMR), oversized mitral annuloplasty, true-sized mitral annuloplasty, and undersized mitral annuloplasty (UMA). (Please note images are not drawn to scale).**

Upon establishing these conditions, all endpoints were acquired. Following the simulation of IMR, the annulus was sequentially conformed to the shape of 3 mitral annuloplasty ring sizes. These conditions included an oversized condition (size 34 Physio™ Ring), a true-sized condition (size 30 Physio™ Ring), and an undersized mitral annuloplasty condition (size 26 Physio™ Ring). These experimental conditions are sequentially shown in Figure 5-25. At each condition, all experimental endpoints were recorded.

### 5.3.2.3. Data Processing

All data were processed offline within a custom MATLAB program (See Appendix E) and averaged over 10 consecutive cardiac cycles. All data are expressed as a mean ± standard error. Mitral regurgitation volume was measured directly by an electromagnetic flow probe located upstream of the atrium and was calculated as the total retrograde volume occurring during MV closure. Echocardiography data were analyzed using Philips QLab (v.7.0; Philips Healthcare; Andover, MA).

#### 5.3.2.4. Statistical Analysis and Experimental Endpoints

Measured endpoints were checked for normality using the Anderson-Darling test. A general linear model using each valve as a random factor was used to investigate the effect of the valve and experimental condition on each of the measured endpoints. To decrease the probability of type I errors, a Bonferroni post hoc test was used to determine if significant differences in each metric existed between experimental conditions. All statistical analyses were completed using Minitab 16 (Minitab Inc, State College, PA).



# CHAPTER 6

## RESULTS

### 6.1 Introduction to the Results

The results of this work are organized and presented by Specific Aim. For Specific Aim 1 (Section 6.2), the results of assessing transducer accuracy and performance are presented first (Sections 6.2.1-6.2.4) and followed by ovine animal characteristics, left heart hemodynamics, and mitral annular forces (Sections 6.2.5- 6.2.10). For Specific Aim 2 (Section 6.3), a pilot study quantifying the stresses imparted on a prosthetic annuloplasty ring in a healthy ovine animal are described (Section 6.3.1) followed by the results of quantifying suture forces in healthy ovine animals (Section 6.3.2). Finally for Specific Aim 3 (Section 6.4), the results of Part A for mimicking healthy and chronic IMR ovine MV geometry and function within the Georgia Tech Left Heart Simulator is presented (Section 6.4.1). This analysis is followed by the results of Specific Aim 3 Part B in which the effect of IMR and undersized annuloplasty on leaflet coaptation, MR, and chordal forces is assessed (Section 6.4.2)

### 6.2 Specific Aim 1 Results

The baseline characteristics, hemodynamics, and tabulated forces for each of the studied animals in Specific Aim 1 are presented in Appendix A. A catalog of the locations of the

echocardiography data sets on the laboratory's electronic server can be found in Appendix E.

### **6.2.1 Accuracy and Precision of the Calibration Apparatus**

A digital force gauge (Chatillon, Largo, FL) was used to verify the incremental loading of the annular force transducer calibration apparatus (Figure 6-1). To test the septal-lateral loading mechanism, the driving screw was turned seven full rotations in half rotation increments to achieve a peak loading of 8.4 N. This loading was repeated for 10 independent trials. The transverse loading mechanism was not tested given both the septal-lateral and transverse measurement arms of each transducer were calibrated using the septal-lateral loading mechanism. The mean septal-lateral force and 95% confidence interval for each measured load is pictured in Figure 6-1. For each rotation of the calibration apparatus's bolt, force increased by approximately 1.2 N. For all bolt rotations, mean measured forces were within the 95% CI of the expected value.

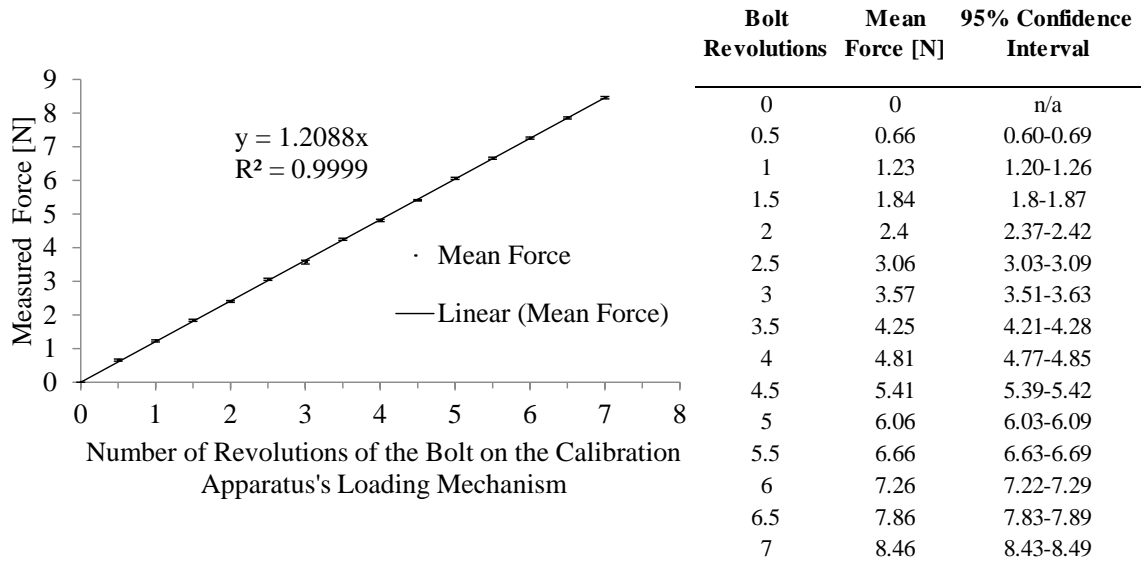


**Figure 6-1 Left: Mean force of 10 independent trials with a 95% confidence interval half-rotation bolt increments; Right: Table displaying the values and intervals at each bolt rotation.**

### 6.2.2 Transducer Calibration, Accuracy, and Precision

Each transducer was calibrated to determine the relationship between applied forces and output voltage. For all transducers, a linear relationship between voltage and calibrated force was observed in both the septal-lateral and transverse directions with correlation coefficients exceeding  $r^2=0.98$ . To assess the accuracy and precision of each calibration, each of the devices was placed back into the calibration apparatus and forces applied in six independent trials. A representative plot of this assessment is plotted and tabulated in Figure 6-2. In cases where the transducer exhibited mean errors (calculated across all tested values) greater than 3%, the calibration was repeated and accuracy and precision reassessed.

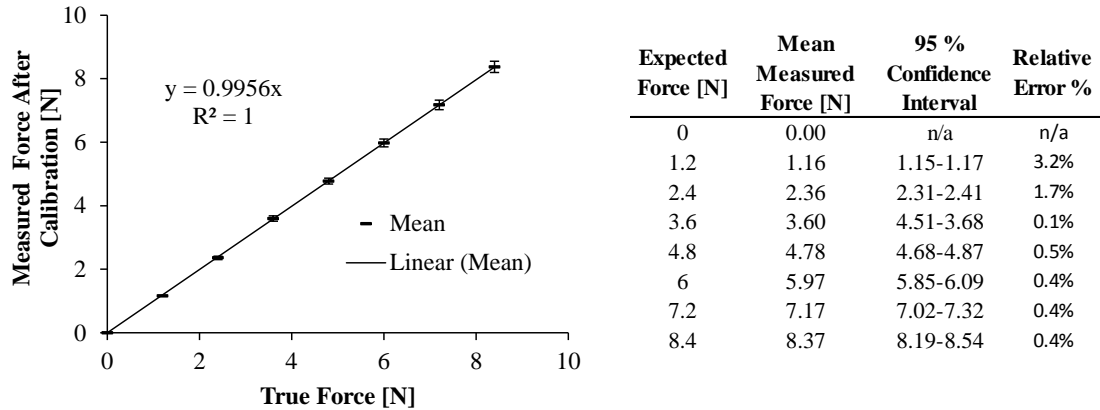


**Figure 6-2 Comparison of measured to true forces for the septal-lateral direction of a representative calibrated transducer.**

### 6.2.3 Effect of Loading on Transducer Measurement Arm Cross-Talk

During the design of the transducer, care was taken to isolate measurement directions resulting in the transducer’s cross-shaped geometry. Strain gages were adhered to the transducer’s spring element at locations more distant than close to the cross-arm intersection to minimize moment arm effects. Testing of these devices found peak loading (8.4 N) along one measurement arm to minimally influence the perpendicular arm resulting in measured forces less than 0.1 N.

### 6.2.4 Effect of Transmitral Flow on the Force Transducer Measurements

The transducer was implanted to the prosthetic annulus of the Georgia Tech Left Heart Simulator and studied under steady flow conditions to determine if transmitral flow creates any effect on force measurements. At transmitral flow rates similar to that estimated in the ovine subjects (10-20 L/min), the transducer measured negligible forces that were not discernible from the baseline noise levels. A representative image from

these *in vitro* experiments and its comparison to *in vivo* transmitral flow is pictures in Figure 6-3.

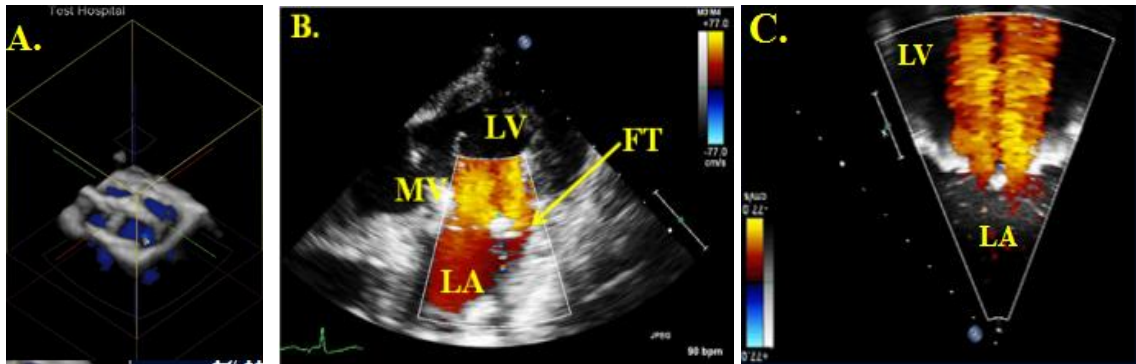


**Figure 6-3 (A) 3D Doppler echocardiographic image of the transducer mounted within the Georgia Tech Left Heart Simulator's static mitral annulus; (B) 2D Doppler echocardiographic image of the transducer (FT) within the sheep subject, the left ventricle (LV), left atrium (LA), and mitral valve (MV) are labeled; (C) Transducer within the simulator displaying similar flow patterns and magnitudes to that experienced in-vivo.**

### 6.2.5 Animal and Left Heart Hemodynamic Characteristics

Baseline characteristics of the control (N=6) and chronic IMR (N=6) animals are presented in Table 6-1. For the chronic IMR animals, the mean MR grade measured 6-8 weeks after myocardial infarction was  $2.3 \pm 0.5$ . Resulting MR grades were comparable with those achieved in previous studies utilizing an identical chronic IMR model [41]. When simulating worst-case hemodynamic loading conditions (LVP ranging from 150 to 200 mmHg), LVP was carefully controlled within each animal. No statistical differences were observed between animal groups for measured levels of elevated LVP and heart rate (Table 6-2). During each study, real-time 3D echocardiography images were acquired to assess transducer anchoring throughout the experiment (See Appendix D for the locations

of the image files on the laboratory's secure server). In all experiments, the transducer remained firmly secured to the mitral annulus.

**Table 6-1 Baseline characteristics of the ovine subjects.**

Parameter	Control Animals (N=6)	Chronic IMR Animals (N=6)
Weight [kg]	40.1 ± 7.4	39.7 ± 2.6
Heart Rate [bpm]	95 ± 15	96 ± 9
LVP [mmHg]	90 ± 2	92 ± 2
d(LVP)/dt [mmHg/s]	2105 ± 712	1253 ± 307
Graded MR	0	2.3 ± 0.5
Percent of infarcted endocardium [%]	0	19.0 ± 1.7

**Table 6-2 Characteristics of the ovine subjects at elevated levels of left ventricular pressure.**

		Target Peak Left Ventricular Pressure [mmHg]				
		90	125	150	175	200
Peak Left Ventricular Pressure [mmHg]	Control	90 ± 2	128 ± 3	151 ± 3	173 ± 3	201 ± 4
	Chronic IMR	92 ± 2	124 ± 2	152 ± 2	177 ± 2	198 ± 4
Heart Rate [beats/min]	Control	95 ± 15	116 ± 33	127 ± 32	140 ± 38	142 ± 35
	Chronic IMR	96 ± 9	111 ± 11	117 ± 16	130 ± 22	143 ± 18

### 6.2.6 Cyclic Annular Force Characteristics

Among control and chronic IMR animals, forces in the septal-lateral and transverse directions were observed to compressively increase from ventricular diastole to mid-systole. Representative unfiltered forces from both a control and chronic IMR animal are plotted with time and LVP in Figure 6-4. In both animals, slight elevations in force are seen during atrial systole followed by sharp rises during isovolumetric contraction.

During this period, septal-lateral and transverse forces were found to increase with LVP ( $p < 0.001$ ) and peak at approximately mid-systole. Implantation of the device was found to modestly affect mitral inflow velocities (Figure 6-5).

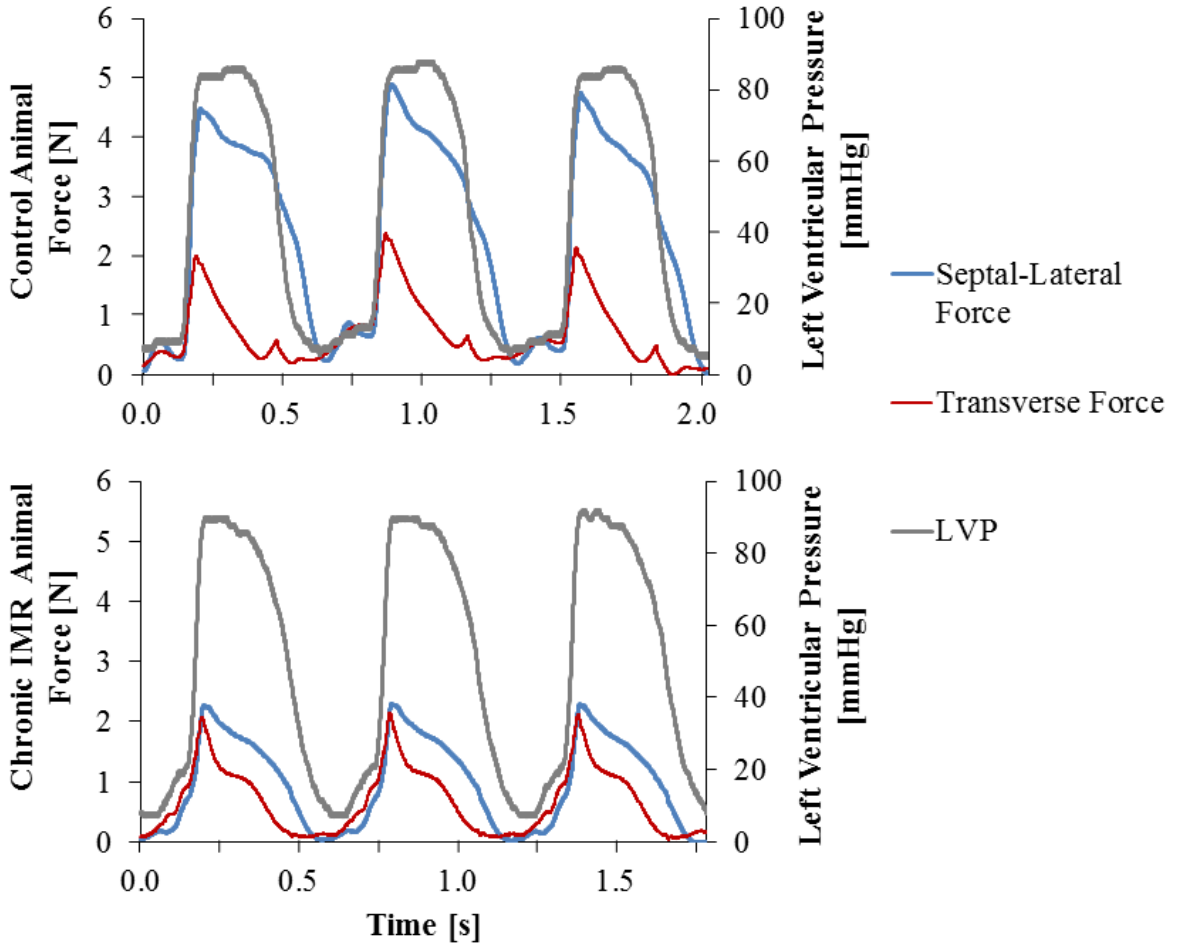


**Figure 6-4** Representative unfiltered forces from both a control (top) and chronic IMR (bottom) animal are plotted with time and LVP.

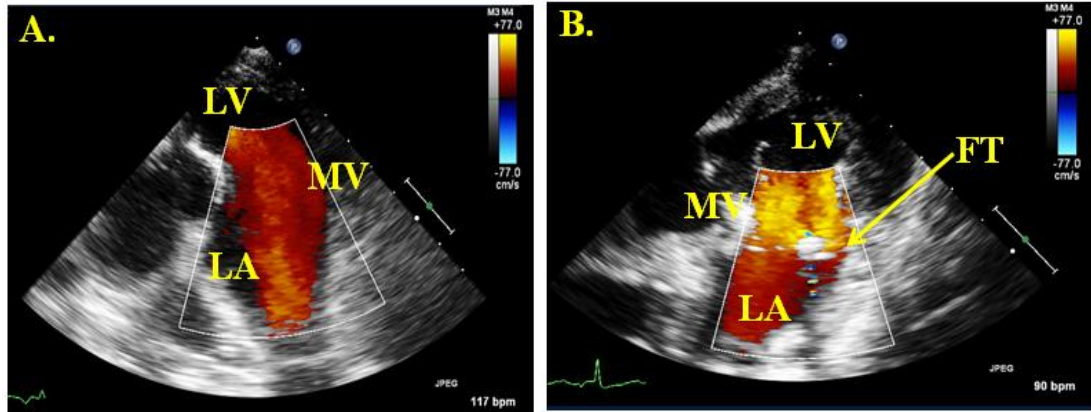


**Figure 6-5 (A) Doppler echocardiographic image of mitral inflow from the Left Atrium (LA) to the Left Ventricle (LV) in absence of the annular Force Transducer (FT); (B) Implanted transducer increases mitral inflow velocity.**

### **6.2.7 Change in Annular Forces with Increasing Afterload: Healthy Animals**

The peak change in septal-lateral force throughout the cardiac cycle was found to significantly increase at each peak level of LVP ( $p < .001$ ). Septal-lateral force was observed to significantly increase at the  $p < .001$  level from the baseline condition  $3.9 \pm 0.8$  N to  $5.2 \pm 1.0$  N (125 mmHg),  $5.9 \pm 0.9$  N (150 mmHg),  $6.4 \pm 1.2$  N (175 mmHg), and  $6.7 \pm 1.5$  N (200 mmHg) respectively. These results are plotted in Figure 6-6. Among all subjects and tested conditions, the peak change in septal-lateral force throughout the cardiac cycle was 9.2 N at 200 mmHg peak LVP.



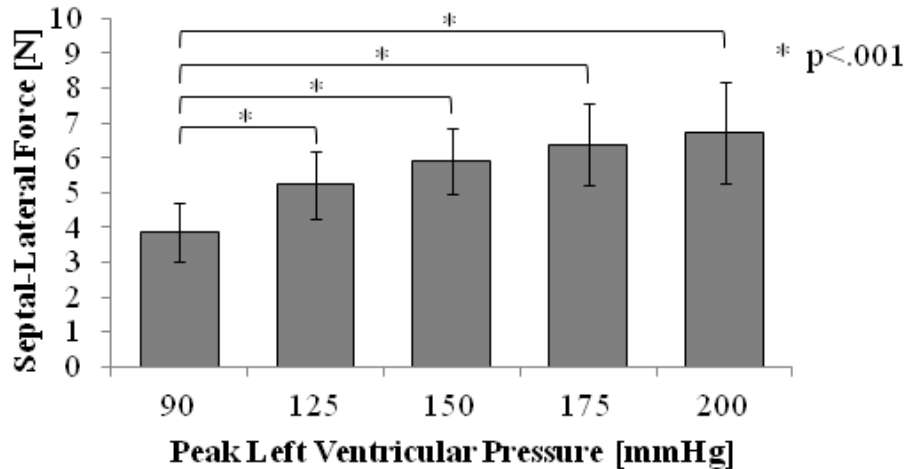


**Figure 6-6 The mean change in septal-lateral force throughout the cardiac cycle increased significantly from baseline to each level of peak left ventricular pressure.**

For the transverse direction, a statistically significant difference in force was found between peak levels of LVP ( $p < .005$ ). The change in transverse force throughout the cardiac cycle was seen to increase from the baseline condition  $2.6 \pm 0.6$  N to  $3.8 \pm 1.0$  N (125 mmHg)  $p < .01$ ,  $4.6 \pm 1.3$  N (150 mmHg)  $p < .001$ ,  $4.3 \pm 1.2$  N (175 mmHg)  $p < .001$ , and  $3.5 \pm 0.7$  N (200 mmHg)  $p < .05$  (Figure 6-7). Although statistically not significant, the mean transverse force was observed to decrease from 150 to 200 mmHg. Since the mean septal-lateral force is much larger at 175 and 200 mmHg (Figure 6-8), shortening of the transverse diameter may be hindered and thus may translate to a lower transverse force. Among all animals, the largest observed change in transverse force throughout the cardiac cycle was 6.3 N at 150 mmHg.

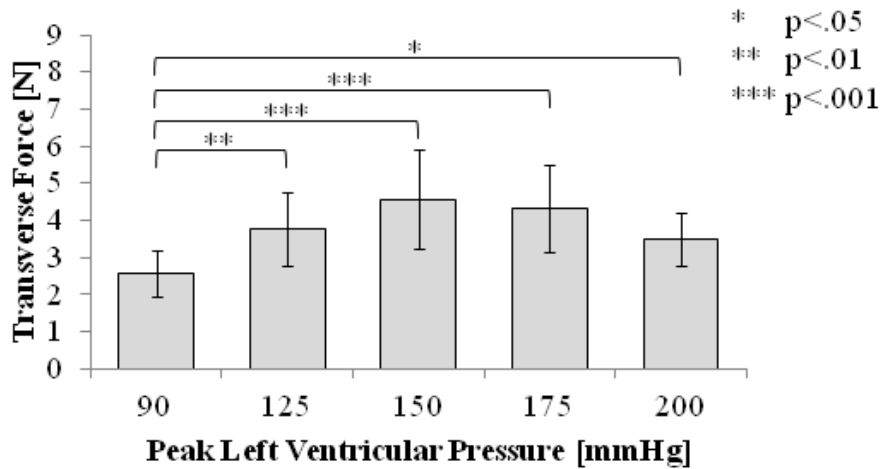


**Figure 6-7 The mean change in transverse force throughout the cardiac cycle increased significantly from baseline to each level of peak left ventricular pressure**

Measurements from each direction were subsequently compared to determine if forces in the septal-lateral direction were greater than those in the transverse. Results revealed the septal-lateral force to be significantly greater than the transverse force at a peak LVP of 90 mmHg ( $p < .05$ ), 125 mmHg ( $p < .05$ ), 175 mmHg ( $p < .001$ ), and 200 mmHg ( $p < .0005$ ) (See Figure 6-8). Due to larger variances in the transverse force, no statistically significant differences were found at the 150 mmHg peak LVP condition.

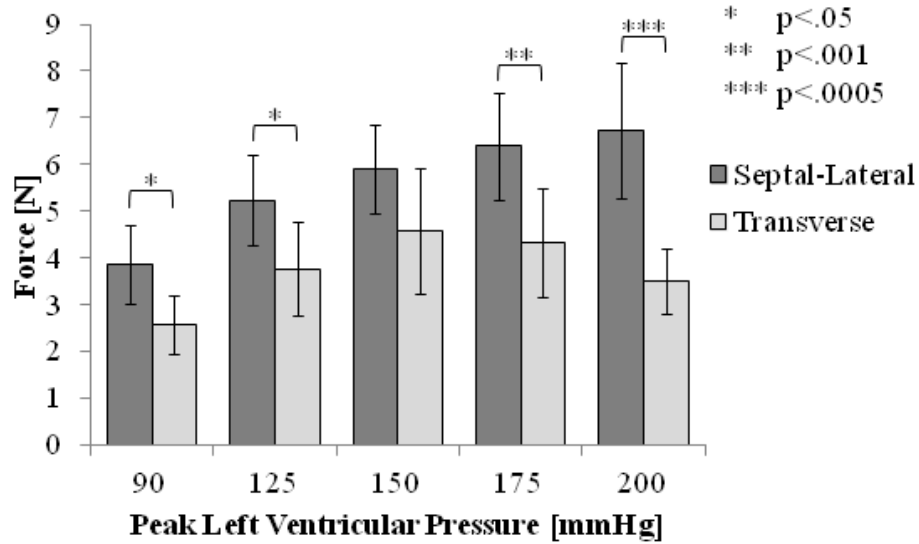


**Figure 6-8 Comparison of each directional force at increasing levels of peak left ventricular pressure.**

### **6.2.8 Change in Annular Forces with Increasing Afterload: Ischemic Mitral**

#### **Regurgitation Animals**

Septal-lateral force within the chronic IMR animals was found to statistically differ between increasing levels of afterload ( $p < 0.001$ ). These forces were observed to increase from the baseline  $2.5 \pm 0.6$  N to  $3.5 \pm 0.7$  N (150 mmHg)  $p < 0.001$ ,  $3.7 \pm 0.6$  N (175 mmHg)  $p < 0.001$ , and  $3.7 \pm 0.8$  N (200 mmHg)  $p < 0.001$ . No significant differences were found between the baseline and  $2.9 \pm 0.6$  N at 125 mmHg peak LVP. The largest septal-lateral force measured among all chronic IMR animals was 4.5 N at 200 mmHg peak LVP.

The changes in transverse forces throughout the cardiac cycle were also found to statistically differ with afterload ( $p < 0.05$ ). Transverse forces were observed to increase from the baseline  $2.2 \pm 0.9$  N to  $2.9 \pm 0.9$  N (150 mmHg)  $p < 0.05$  and  $2.9 \pm 1.2$  N (175 mmHg)  $p < 0.05$ . Transverse forces measured at 125 mmHg ( $2.7 \pm 0.8$  N) and 200 mmHg

( $2.7 \pm 1.2$  N) were found to be statistically not different from the baseline measurement. The largest transverse force measured within the chronic IMR animals was 4.6 N at 175 mmHg peak LVP. To determine if directional differences exist, septal-lateral and transverse forces were compared at each level of peak LVP. No statistical differences were observed between these directions within the studied chronic IMR animals.

### **6.2.9 Change in Annular Forces with Increasing Afterload: Healthy versus Ischemic Mitral Regurgitation Animals**

To determine if an inferior LV infarction results in a decrease in mitral annular forces, chronic IMR forces were compared to those measured previously in a healthy ovine model. Among all animals, the mean change in septal-lateral force was found to statistically differ between increasing levels of afterload ( $p < 0.001$ ) and animal groups ( $p < 0.001$ ). Septal-lateral forces in the control animals were found to be significantly larger than those in the chronic IMR group at 90 mmHg ( $p < 0.01$ ), 125 mmHg ( $p < 0.005$ ), 150 mmHg ( $p < 0.005$ ), 175 mmHg ( $p < 0.005$ ), and 200 mmHg ( $p < 0.005$ ). These results are plotted in Figure 6-9. Among all animals, the mean change in transverse force was found to statistically differ with increasing levels of afterload ( $p < 0.001$ ) but not between animal groups. Although not significant, the mean transverse forces within the chronic IMR group were observed to be consistently lower in magnitude than those measured in control animals, as shown in Figure 6-9.

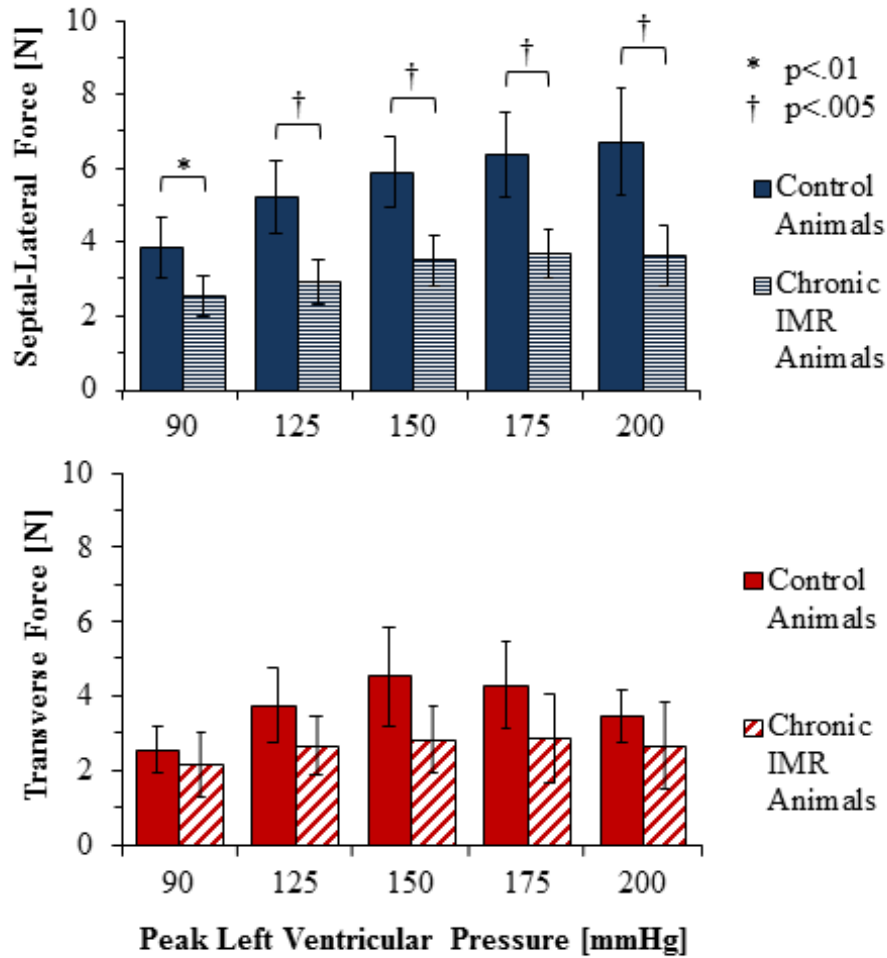


**Figure 6.9 Top:** The measured change in septal-lateral force throughout the cardiac cycle was observed to be significantly greater within the control animals at each level of peak left ventricular pressure; **Bottom:** No significant differences in the change in transverse force throughout the cardiac cycle was observed between the animal groups and left ventricular pressure levels.

#### 6.2.10 Rate of Change of Force during Isovolumetric Contraction: Healthy versus Ischemic Mitral Regurgitation Animals

The peak rate of increase for force (dF/dt) during isovolumetric contraction was quantified for both the control and chronic IMR animals at elevated levels of LVP. Among all animals, septal-lateral dF/dt was found to significantly differ between increasing levels of peak LVP ( $p < 0.005$ ) and animal groups ( $p < 0.05$ ). Within the control

group, septal-lateral dF/dt was found to significantly increase from the baseline condition to 150 mmHg (p<0.01), 175 mmHg (p<0.005), and 200 mmHg (p<0.001) (Table 6-3). No significant differences were observed between the baseline and 125 mmHg. Within the chronic IMR group, the peak septal-lateral dF/dt was found to significantly increase from the baseline to 150 mmHg (p<0.005), 175 mmHg (p<0.001), and 200 mmHg (p<0.001). Similar to the control group, no significant differences were found between the baseline condition and 125 mmHg peak LVP. After adjusting for multiple comparisons (Bonferroni), no significant differences in septal-lateral dF/dt were found between the control and chronic IMR animal groups at each level of LVP.

**Table 6-3 Peak rate of change for septal-lateral and transverse forces during isovolumetric contraction for the control and chronic IMR animals, significance is reported to the baseline values at 90 mmHg peak LVP within each group and direction: \* p<0.01, † p<0.005, and ‡ p<0.001.**

		Peak Left Ventricular Pressure [mmHg]				
		90	125	150	175	200
Septal-Lateral dF/dt [N/s]	Control	77 ± 31	126 ± 48	150 ± 72 *	169 ± 89 †	180 ± 95 ‡
	Chronic IMR	39 ± 12	42 ± 6	64 ± 9 †	66 ± 7 ‡	74 ± 12 ‡
Transverse dF/dt [N/s]	Control	36 ± 16	70 ± 32	88 ± 42 †	85 ± 43 *	72 ± 48
	Chronic IMR	30 ± 18	40 ± 19	60 ± 17 †	68 ± 35 ‡	62 ± 26 †

In the transverse direction, the peak dF/dt was found to significantly increase with afterload within all subjects (p<0.001), but did not significantly differ between groups (Table 6-3). In the control group, transverse dF/dt was found to significantly increase

from the baseline to 150 ( $p < 0.005$ ) and 175 mmHg ( $p < 0.01$ ). Within the chronic IMR subjects, transverse  $dF/dt$  was found to increase from the baseline to a peak LVP of 150 mmHg ( $p < 0.005$ ), 175 mmHg ( $p < 0.001$ ), and 200 mmHg ( $p < 0.005$ ).

### **6.3 Specific Aim 2 Results**

The baseline characteristics, hemodynamics, and tabulated forces for each of the studied animals in Specific Aim 2 is presented in Appendix B. A catalog of the locations of the echocardiography data sets on the laboratory's electronic server can be found in Appendix E.

#### **6.3.1 Annuloplasty Ring Stress Pilot Study**

##### **6.3.1.1 Animal Characteristics and Ring Transducer Implantation**

Prior to cardiopulmonary bypass, echocardiography revealed the ovine subject (45 kg) to exhibit an end-diastolic mitral annular area of  $7.14 \text{ cm}^2$  with septal-lateral and transverse dimensions of 2.45 cm and 3.37 cm, respectively. Negligible MR (grade 1+) was observed. During cardiopulmonary bypass and ring implantation, the transducer was found to slightly undersize the mitral annulus (Figure 6-10A and B). At implantation, a suture passed through the ring cuff inadvertently damaged the strain bridge measuring in-plane stresses on the septal portion of the ring. As a result, the study proceeded with 7 of 8 ring measurement locations.

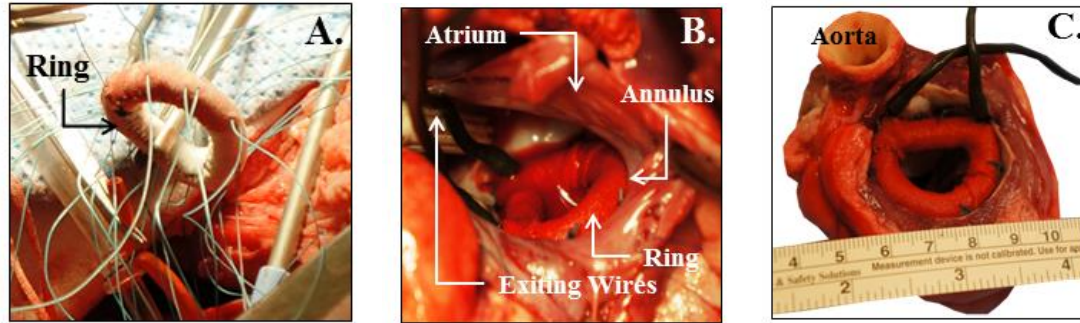


**Figure 6-10 (A) Ten 2-0 sutures are placed through the suture cuff of the annuloplasty ring transducer for implantation, (B) While on cardiopulmonary bypass the transducer is implanted to the mitral annulus, (C) Post-experimentation, the left atrium is removed and the transducer was inspected for firm anchoring to the mitral annulus.**

#### 6.3.1.2 Ring Stresses at Implantation

Following successful implantation; the stresses imparted on the ring by the flaccid annulus were measured. The distribution of stresses on the ring surface was heterogeneous with a combination of compressive (-) and tensile (+) stresses. On both the in- and out-of-plane surfaces, these stresses ranged from -3.17 to 5.34 MPa (Figure 6-11). The largest stress was observed on the apical-basal surface at the septal portion of the ring. While sutures were attempted to be placed at near symmetric locations around the ring's circumference, the order of suture anchoring was hypothesized to play a significant role in the heterogeneous sign and magnitude of the observed stresses.



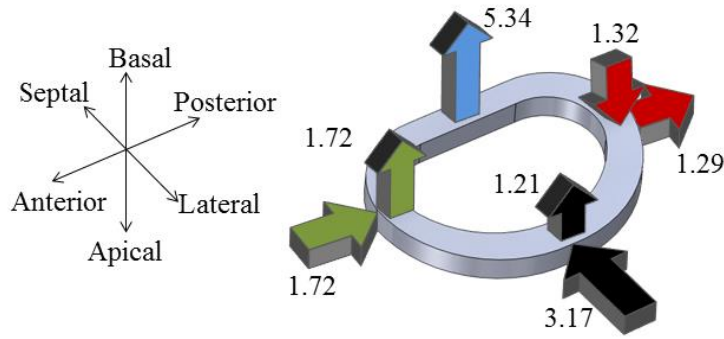


**Figure 6-11 Annuloplasty ring stresses measured after implanting the ring to the mitral annulus in the flaccid cardioplegic heart (all stresses are expressed in MPa) with arrows indicating compression (arrows pointing towards the ring) or tension (arrows pointing away from the ring) at each measurement location.**

6.3.1.3. Ring Stresses throughout the Cardiac Cycle

After weaning from cardiopulmonary bypass and establishing baseline hemodynamics, local cyclic stresses in the ring were successfully measured. Two consecutive representative cardiac cycles of the ring stresses with LVP and EKG are plotted in Figure 6-12. Through each cardiac cycle, ring stresses were observed to increase from ventricular diastole and peak during mid-systole. Exceptions to this observation included the lateral ring area (in the apical-basal direction) and the posterior commissural area (in the anterior-posterior direction) whose stresses became more negative during isovolumetric contraction indicating local tensile loading. The mean peak change in ring stresses for 10 consecutive cardiac cycles is shown in Table 6-4.

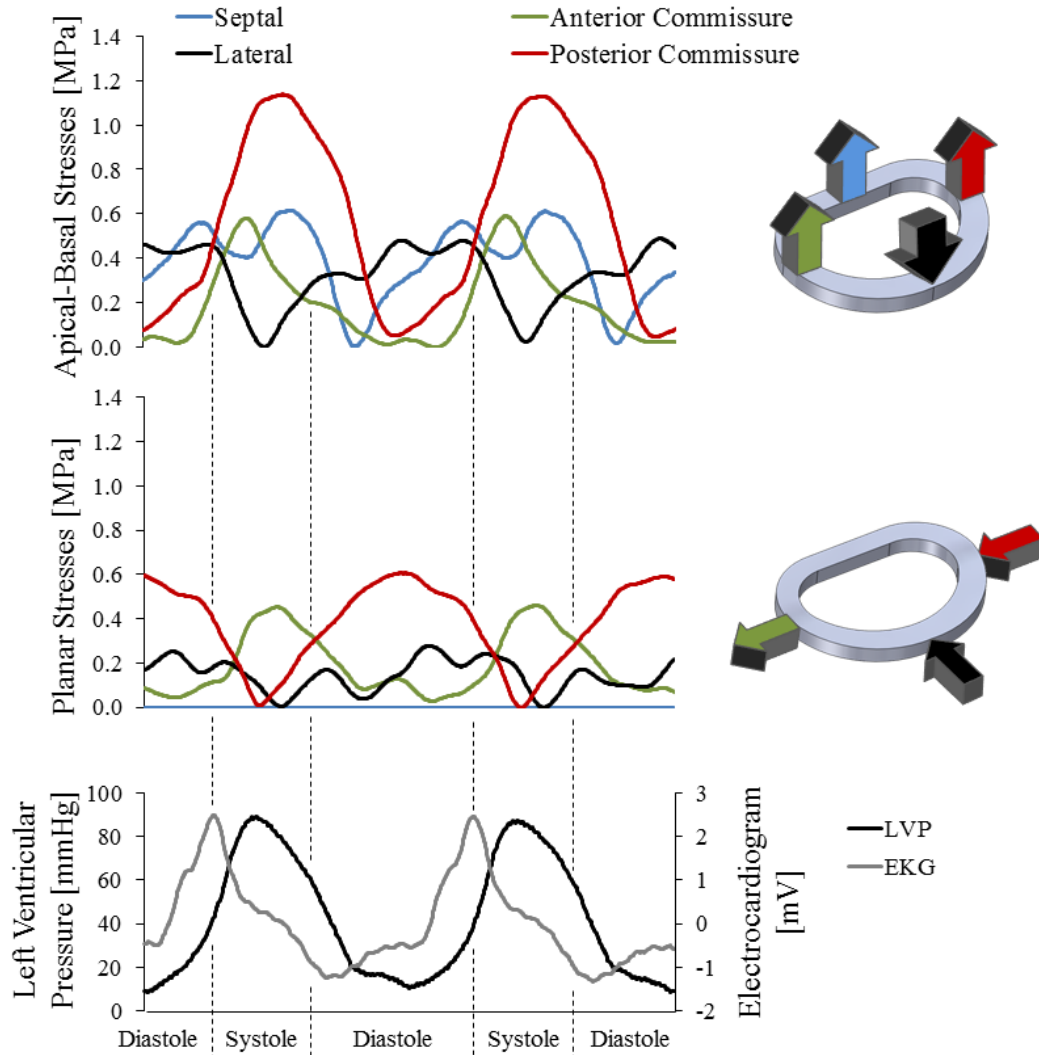


**Figure 6-12 Left: Two consecutive representative cardiac cycles of the apical-basal and planar ring stresses plotted with left ventricular pressure and electrocardiography; Right: pictorial representations of the ring with arrows indicating compressive stresses (arrows pointing towards the ring) or tensile stresses (arrows pointing away from the ring) at each measurement location at peak left ventricular pressure.**

Acquired 3D echocardiography images demonstrated the transducer to remain fixed in the annular plane throughout the experimental protocol. From Doppler echocardiography measurements, it was assessed that the implanted ring increased the mean transmitral pressure gradient from 1 mmHg (pre-implantation) to 8 mmHg at 126

beats/min. Combined with the inner orifice area of the ring transducer (1.6 cm<sup>2</sup>), ring implantation resulted in a moderate level of MV stenosis. Upon the study's completion, the heart was explanted, and the transducer was found to remain firmly secured to the mitral annulus with no thrombus formation.

**Table 6-4 10-cycle ensemble averaged stresses at each annuloplasty ring location and direction expressed as a mean  $\pm$  1 standard deviation in MPa (positive values indicate tension while negative values indicate compression).**

	Location on the Annuloplasty Ring			
	Septal	Lateral	Anterior Commissure	Posterior Commissure
Apical -Basal Direction	0.63 $\pm$ 0.02	-0.49 $\pm$ 0.01	0.54 $\pm$ 0.02	1.13 $\pm$ 0.01
Planar Direction	n/a	-0.31 $\pm$ 0.04	0.46 $\pm$ 0.01	-0.61 $\pm$ 0.01

### 6.3.2 Annuloplasty Ring Suture Forces

The baseline characteristics, hemodynamics, and tabulated forces for each of the animals in Specific Aim 2 is presented in Appendix B. A catalog of the locations of the echocardiography data sets on the CFM Lab's electronic server can be found in Appendix E.

#### 6.3.2.1. Transducer Calibration, Accuracy, and Precision

Each annuloplasty ring suture transducer was calibrated to determine the relationship between applied forces and output voltage. For all transducers, a linear relationship between voltage and calibrated force with correlation coefficients exceeding  $r^2=0.98$  (Figure 6-13). To assess the accuracy and precision of each calibration, the devices were

placed back into the calibration apparatus and forces applied in five independent trials. A representative plot of this assessment for the same transducers plotted in Figure 6-13 is plotted and tabulated in Figure 6-14. Calibration's exhibited mean accuracies of  $\pm 3\%$ .

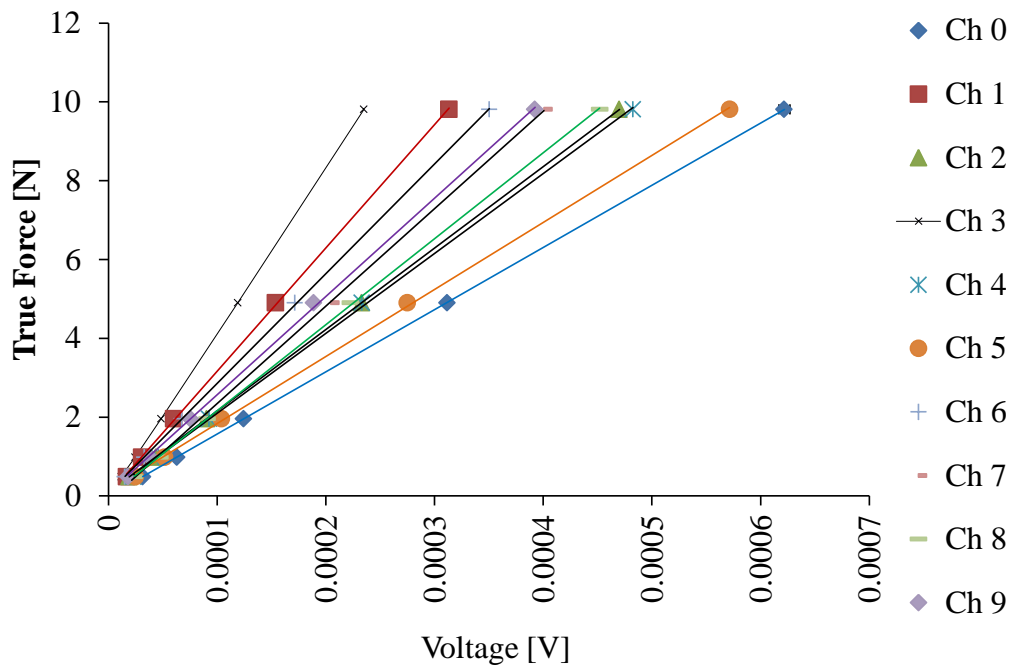


**Figure 6-13 Representative calibration curves for the 10 suture force transducers attached to a size 24 Physio™ ring**

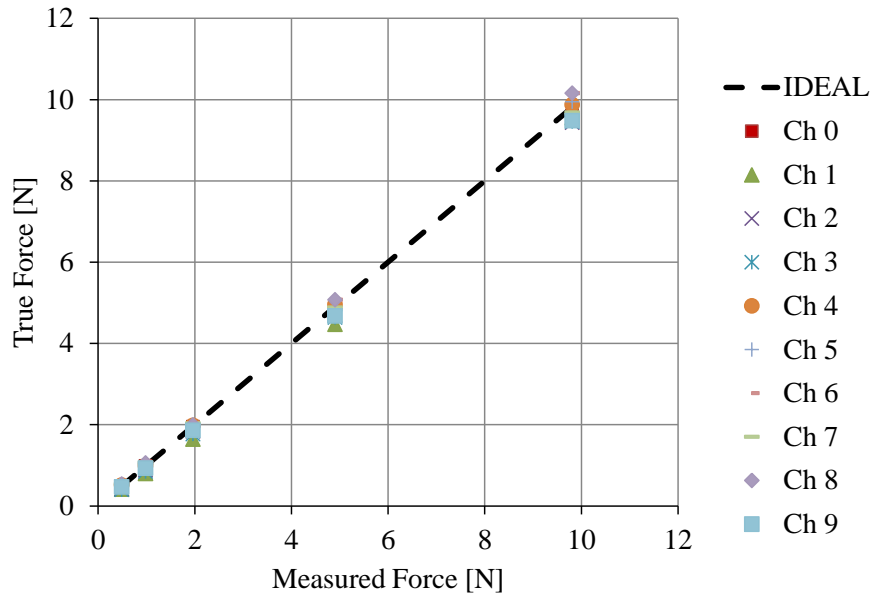


**Figure 6-14 Representative comparison of measured to true forces for the transducers whose calibration curves are graphed in Figure 6-13.**

### 6.3.2.2 Baseline and Elevated Animal Characteristics

Annuloplasty ring suture forces were successfully quantified in eight ( $59 \pm 10$  kg) healthy ovine animals. Baseline characteristics of the animals are presented in Table 6-5. Four animals received true-sized rings. The rings used for true sizing included a size 26, two size 28's, and a size 32 Physio<sup>TM</sup> ring (Table 6-5). All animals in the undersized ring group received a size 26 ring.

**Table 6-5 Baseline characteristics of the healthy ovine animals.**

	Animal Weight (kg)	Annulus Sized at Bypass (Physio™)	Implanted Ring Size (Physio™)
True-Sized	56 ± 10	28.5 ± 2.5	28.5 ± 2.5
Undersized	62 ± 10	30 ± 0.0	26 ± 0.0

Cyclic suture forces were acquired for 10 consecutive cardiac cycles reaching peak LVPs of 100, 125, and 150 mmHg. The mean LVP and heart rate corresponding to cycles for which the cyclic forces were recorded are presented in Table 6-6. From Table 6-6, negligible differences in LVP and heart rate were observed between the undersized and true-sized ring groups. Transmitral pressure gradients were quantified both pre and post-annuloplasty by Doppler echocardiography. Animals receiving a true sized ring had negligible changes in the transmitral gradient while animals receiving an undersized ring exhibited a net increase of  $3 \pm 1$  mmHg. During each study, real-time 3D echocardiography images were acquired to assess transducer anchoring throughout the experiment. In all experiments, the transducer remained firmly secured to the mitral annulus.

**Table 6-6 Characteristics of the ovine subjects at elevated levels of left ventricular pressure.**

		Target Left Ventricular Pressure [mmHg]		
		100	125	150
Peak Left Ventricular Pressure [mmHg]	True-Sized	101 ± 3	126 ± 1	151 ± 1
	Undersized	104 ± 2	129 ± 3	152 ± 2
Heart Rate [beats/min]	True-Sized	108 ± 29	119 ± 29	129 ± 29
	Undersized	109 ± 15	121 ± 15	134 ± 18

### 6.3.2.3 Cyclic Suture Force Characteristics

Among all levels of LVP, cyclic suture forces were observed to increase from ventricular diastole to mid-systole. Two representative cardiac cycles of measured forces with LVP is pictured in Figure 6-15. During onset of ventricular systole, suture forces exhibited sharp increases in force magnitude reaching their maximal values near mid-systole. During ventricular ejection, the magnitude of suture forces gradually decreased. This phase was followed by a sharp decrease in forces to their minimal diastolic values during ventricular relaxation.

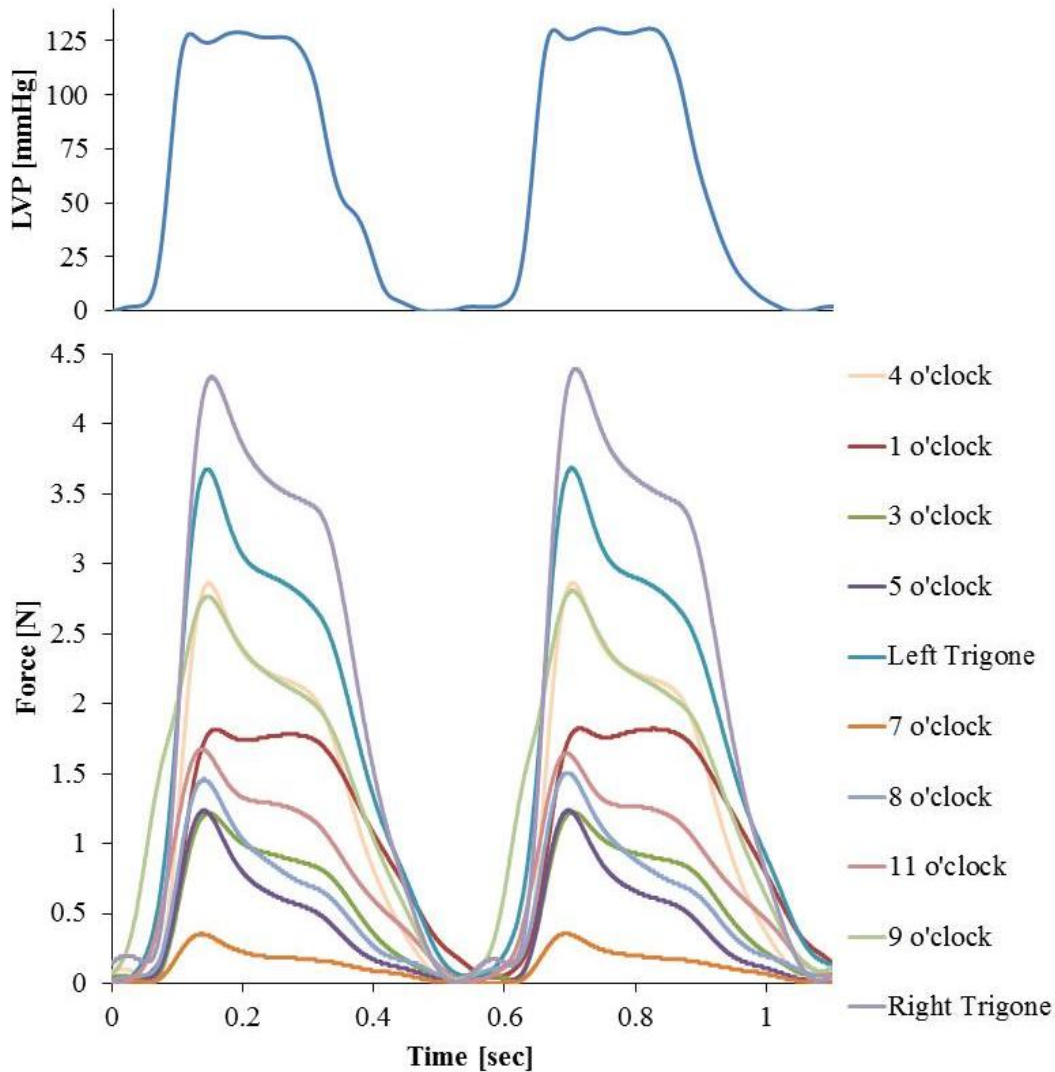


**Figure 6-15** Two representative cardiac cycles of measured suture forces with the corresponding left ventricular pressure trace.

#### 6.3.2.4. Effect of Ring-Annulus Sizing on Cyclic Suture Forces

All suture forces (regardless of ring position) were averaged for each of the true-sized and undersized rings to assess the effects of ring-annulus sizing. These results are shown in Figure 6-16. For both the true-sized and undersized rings, cyclic suture forces were demonstrated to marginally increase with increasing levels of LVP. Mean suture forces for the undersized rings were demonstrated to increase from  $2.3 \pm 1.5$  N (90 mmHg LVP)



to  $2.7 \pm 1.7$  N (125 mmHg LVP) and  $2.9 \pm 1.9$  N (150 mmHg LVP). For the true-sized rings, mean suture forces increased from  $1.6 \pm 0.7$  N (90 mmHg LVP) to  $1.9 \pm 0.9$  N (125 mmHg LVP) and  $2.2 \pm 1.0$  N (150 mmHg LVP). Undersized ring suture forces were approximately 41%, 38%, and 34% larger than true-sized ring suture forces at peak LVPs of 100, 125, and 150 mmHg, respectively.

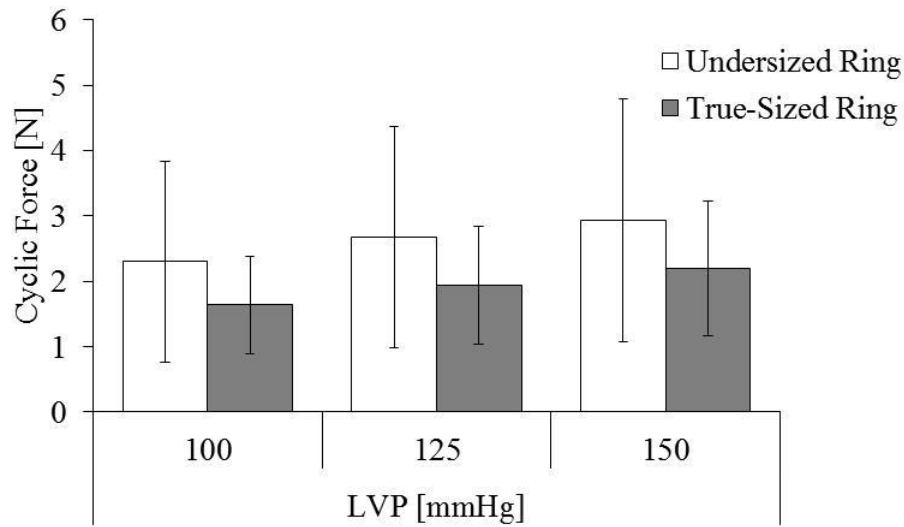


**Figure 6-16 Suture forces averaged by ring-annulus sizing.**

#### 6.3.2.5. Effect of Ring-Annulus Sizing and Suture Position on Cyclic Suture Forces

Based on the observed differences in cyclic force magnitudes between undersized and true-sized annuloplasty rings (Figure 6-17), the suture forces at each suture location were compared. Mean cyclic forces for all sutures were observed to increase with increasing levels of LVP (Figure 6-17). Cyclic suture forces were observed to range from 0.2 to 8.1 N and from 0.3 to 4.1 N for the undersized and true-sized rings, respectively.

From inspection, suture forces were elevated and depressed at similar suture locations regardless of ring-annulus sizing. The largest forces for both the undersized and

true-sized rings were observed at each trigone, 3 o'clock, and 9 o'clock positions. Similarly, the smallest forces were observed between the 7 o'clock and 8 o'clock positions. While further studies are required to evaluate this hypothesis, these trends may be likely due to suture securing order on the ring (left trigone, right trigone, then proceeding clockwise from the 11 o'clock position).

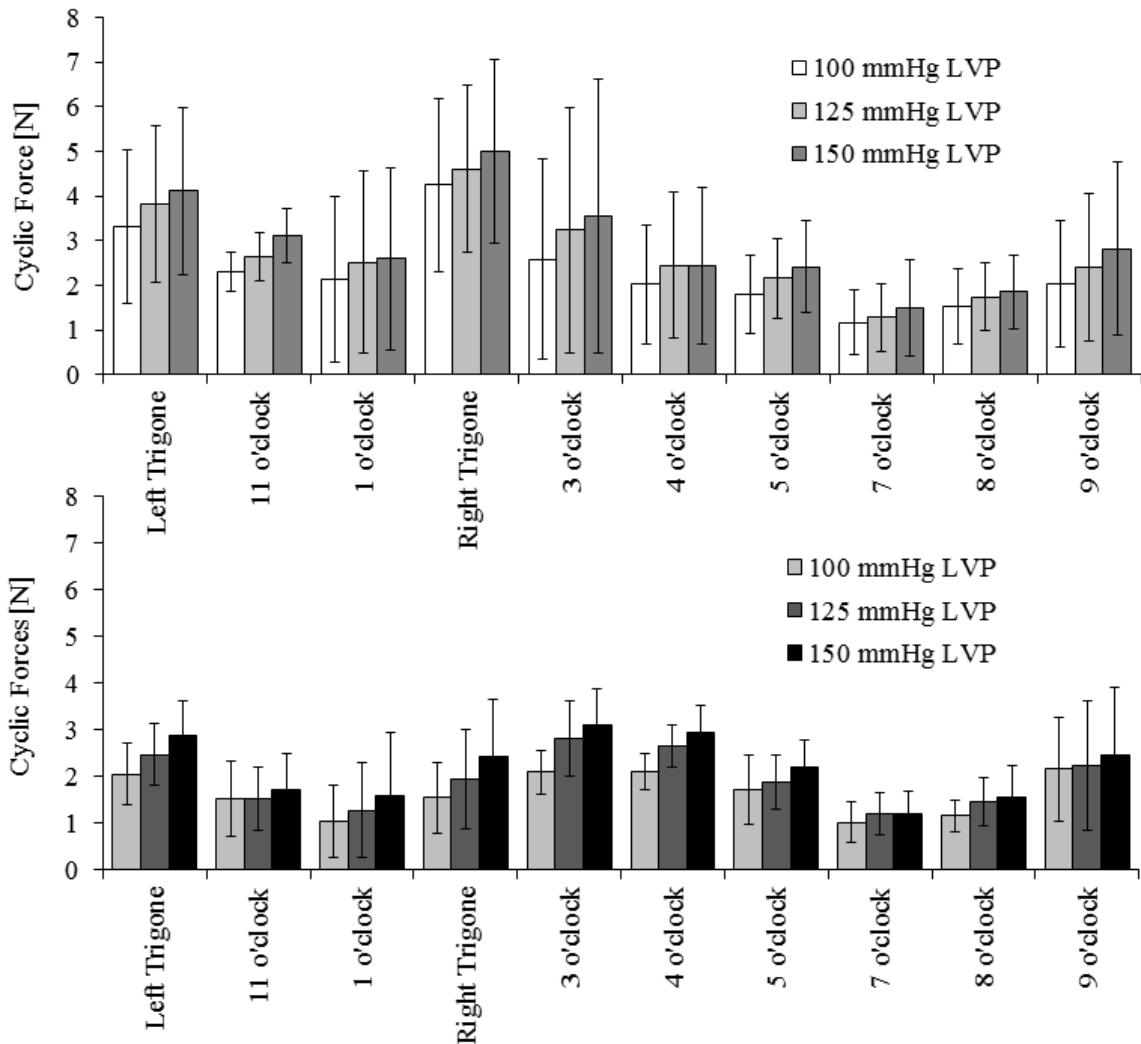


**Figure 6-17 Top: Undersized annuloplasty cyclic suture forces expressed as a mean  $\pm$  1 standard deviation for each ring position; Bottom: True-sized annuloplasty cyclic suture forces expressed as a mean  $\pm$  1 standard deviation for each ring position.**

Suture forces of the undersized rings were predominately greater than those measured for true-sized rings at each level of LVP. The percent differences between undersized and true-sized ring suture forces for each suture position and LVP is tabulated in Table 6-7. As a whole, undersized ring suture forces were larger. These differences were the greatest at ring locations between the left and right fibrous trigones. Paradoxically, suture forces at the 4 o'clock position were larger for true-sized rings at all levels of LVP. While further studies are required, this trend may be due to the disproportionately higher loads carried by the right trigone and the 3 o'clock position on the undersized rings which may lower cyclic forces at the 4 o'clock position.

**Table 6-7 Average percent increase in cyclic suture forces with an undersized ring.**

		Left Ventricular Pressure [mmHg]			Mean $\pm$ 1 SD
		100	125	150	
Ring Position	Left Trigone	61%	55%	43%	53 $\pm$ 9 %
	11 o'clock	50%	75%	83%	69 $\pm$ 17 %
	1 o'clock	106%	97%	63%	89 $\pm$ 9 %
	Right Trigone	175%	139%	107%	140 $\pm$ 34 %
	3 o'clock	24%	15%	15%	18 $\pm$ 5 %
	4 o'clock	-4%	-8%	-17%	-10 $\pm$ 7 %
	5 o'clock	5%	14%	10%	10 $\pm$ 4 %
	7 o'clock	15%	7%	25%	16 $\pm$ 9 %
	8 o'clock	30%	20%	19%	23 $\pm$ 6 %
	9 o'clock	-5%	8%	14%	6 $\pm$ 10 %

### 6.3.2.6 Variation of Suture Forces by Annuloplasty Ring Region

Based on the observed trends with suture location and ring-annulus sizing, the variation of suture forces by annuloplasty ring region was investigated. Cyclic forces were averaged for sutures residing in two regions of the annuloplasty rings. The anterior region was specified to include sutures located between the left and right fibrous trigones. The posterior ring region consisted of all other suture locations (proceeding clockwise from the 3 o'clock to 9 o'clock positions). The results of these analyses are plotted in Figure 6-18. Anterior ring suture forces were greater for the undersized rings for LVPs of 100 mmHg ( $3.0 \pm 1.7$  N vs.  $1.5 \pm 0.8$  N), 125 mmHg ( $3.4 \pm 1.7$  N vs.  $1.8 \pm 0.9$  N), and 150 mmHg ( $3.7 \pm 1.8$  N vs.  $2.1 \pm 1.1$  N), respectively. Comparatively, posterior ring suture forces were similar between the undersized and true-sized rings at LVPs of 100 mmHg ( $1.9 \pm 1.3$  N vs.  $1.7 \pm 0.7$  N), 125 mmHg ( $2.2 \pm 1.5$  N vs.  $2.0 \pm 0.9$  N), and 150 mmHg ( $2.4 \pm 1.7$  N vs.  $2.2 \pm 1.0$  N), respectively.

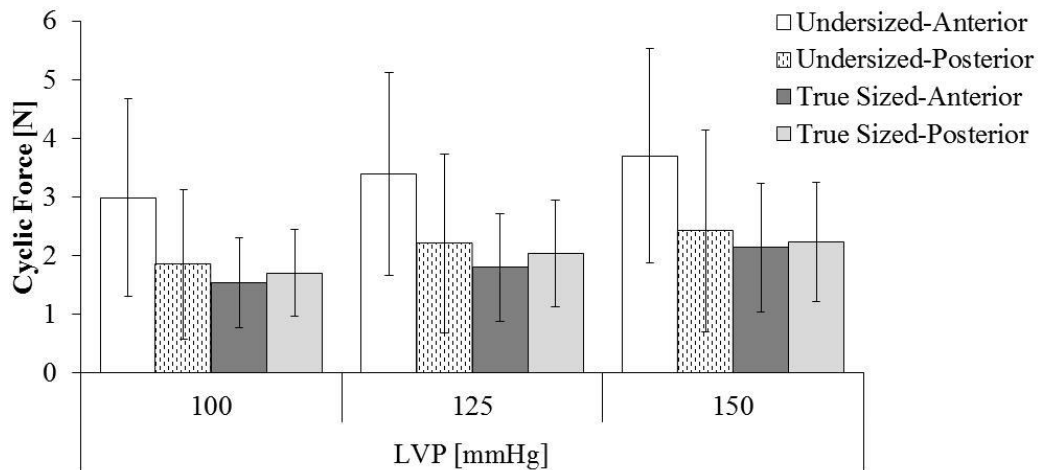


**Figure 6-18 Suture forces by ring region and ring-annulus sizing at each level of left ventricular pressure.**

## 6.4 Specific Aim 3 Results

### 6.4.1 Part A: In Vitro Mitral Valve Simulator Mimics Systolic Valvular Function of Healthy and Chronic Ischemic Mitral Regurgitation Ovine Model

The baseline characteristics, hemodynamics, and tabulated measurements for each of the studied animals in Specific Aim 3 is presented in Appendix C. Tabulated data from the corresponding in vitro simulation can additionally be found in Appendix C. A catalog of the locations of the echocardiography data sets on the laboratory's electronic server can be found in Appendix E.

#### 6.4.1.1 Animal Characteristics

Baseline characteristics of the control and chronic IMR animals are presented in Table 6-8. Both animal groups exhibited similar weights, heart rate, peak LVP, and anterior leaflet heights. Similar to previous studies, the chronic IMR animals exhibited a reduced rate change of LVP during isovolumetric contraction ( $d(LVP)/dt$ ) and mitral annular area increase of approximately 60% as modeled within the *in vitro* simulator.

**Table 6-8 Baseline characteristics of the ovine subjects; Note mitral annular area was measured at peak left ventricular pressure**

	Weight (kg)	Heart Rate [beats/min]	Peak LVP [mmHg]	dLVP/dt [mmHg]	Infarcted LV Endocardium (%)	Anterior Leaflet Height [cm]	Mitral Annular Area [cm <sup>2</sup> ]
<b>Control</b>	38 ± 2	98 ± 15	103 ± 6	1842 ± 493	0	1.8 ± 0.1	6.4 ± 1.2
<b>Chronic IMR</b>	39 ± 2	100 ± 13	101 ± 8	1592 ± 490	18.5 ± 1.6	1.9 ± 0.1	10.4 ± 2.2

The simulation of the chronic IMR valve geometry was a direct function of the annular perturbations measured in our animals and the relative PM displacements determined from historic data sets. From this data, the posteromedial PM was observed to have a mean relative displacement of 7.25 mm laterally, 10.05 mm posteriorly, and 1.75 mm basally; while the anterolateral PM exhibited a mean relative displacement of 4.04 mm laterally, 1.28 mm anteriorly, and 3 mm apically. These relative displacements were similar to those observed previously by Tibayan and colleagues [55]. In pilot studies, the use of these absolute displacements resulted in PM-chordal tearing. We believe this tearing was a consequence of using post-mortem tissue whereas *in vivo* the MV is distended over a greater period of time (8 weeks) and has exhibited the capacity to actively remodel [122,123]. For these reasons, intermediary levels of these displacements were utilized (See Section 5.3.1.3).

#### 6.4.1.2 A2-P2 Leaflet Coaptation

Leaflet coaptation across the A2-P2 annular diameter was evaluated for coaptation length, coaptation depth, and tenting area (Table 6-9). Measured values within each animal group were compared to those measured within the conditions simulated *in vitro*. For the control conditions, no significant differences were observed between the healthy animals and MV simulator in coaptation length ( $p=.681$ ), coaptation depth ( $p=.559$ ), and tenting area ( $p=.199$ ) (Table 6-9). Similarly for the chronic IMR conditions, no differences were observed between models in coaptation length ( $p=.596$ ), coaptation depth ( $p=.621$ ), and tenting area ( $p=.879$ ). While not reaching statistical significance,

coaptation length was consistently lower in the simulated conditions as verified by the comparatively greater coaptation depth.

**Table 6-9 A2-P2 coaptation characteristics between the animal and simulated valves; \* denotes a p<0.05 significant difference between the chronic IMR and control conditions simulated *in vitro*.**

		Coaptation Length [mm]	Coaptation Depth [mm]	Tenting Area [cm <sup>2</sup> ]
<b>Control</b>	<b>Animal</b>	4.4 ± 0.4	1.8 ± 0.2	0.23 ± 0.07
	<b>Simulator</b>	4.0 ± 0.4	2.1 ± 0.3	0.16 ± 0.05
<b>Chronic IMR</b>	<b>Animal</b>	3.2 ± 0.3	2.4 ± 0.8	0.27 ± 0.13
	<b>Simulator</b>	3.1 ± 0.6 *	2.8 ± 1.0 *	0.31 ± 0.13 *

To demonstrate changes in coaptation within the GTLHS, each measure of coaptation was compared between the simulated control and chronic IMR conditions (Table 6-9). Results revealed the coaptation length to significantly decrease from the control to chronic IMR condition (p=.027) across the A2-P2 annular diameter. Additionally, coaptation depth (p=.046) and tenting area (p=.028) were observed to significantly increase with simulated chronic IMR.

#### 6.4.1.3 Mitral Regurgitation

Mitral regurgitation was assessed between the chronic IMR animals and simulated conditions. Within the animal group, observed MR was consistent with previous studies reaching a mean grade of 3.17±0.75 [41]. For the simulated conditions, MR was quantified by direct measurement using an electromagnetic flow probe. The mean *in vitro* mitral regurgitation fraction was found to reach 46±6 % and mean grade of 3+. In

comparison to the chronic IMR animals, *in vitro* MR jets were observed to be asymmetric and originate from the tethered A3-P3 leaflets.

#### 6.4.1.4 Anterior Leaflet Mechanics

For control conditions, no significant differences were observed in the A2 leaflet strain between the control animals and simulated conditions in the radial ( $21 \pm 14$  % vs.  $32 \pm 18$  %,  $p=.230$ ) and circumferential ( $6 \pm 10$  % vs.  $11 \pm 7$  %,  $p=.364$ ) directions. Similarly, no significant differences were observed between the chronic IMR animals and simulated IMR conditions and in the radial ( $21 \pm 11$  % vs.  $34 \pm 18$  %,  $p=.151$ ) and circumferential ( $7 \pm 9$  % vs.  $9 \pm 7$  %,  $p=.586$ ) directions respectively. To determine if leaflet strain increases from a control to chronic IMR valve geometry, radial and circumferential strains were compared between the simulated conditions. In comparison to the control condition, results revealed a significant increase in radial ( $p=.028$ ) and circumferential ( $p=.028$ ) strains.

In addition to the peak measured values, the peak rate of change of these strains ( $d(\epsilon)/dt$ ) were determined during Isovolumetric contraction and compared between animal and simulation groups (Table 6-10). Since these values are largely a function of the rate at which LVP increases, all  $d(\epsilon)/dt$  values were normalized by  $d(LVP)/dt$  (Table 6-10). Results revealed no significant differences between the control animals and simulated control conditions in the radial ( $p=.873$ ) and circumferential ( $p=.109$ ) directions respectively. Similar results were observed between the chronic IMR animals in the radial ( $p=.631$ ) and circumferential ( $p=.200$ ) directions. To determine if leaflet strain rate increases from a control to chronic IMR valve geometry condition, radial and



circumferential strain rates were compared between the simulated conditions. In comparison to the control condition, results revealed a significant increase in the normalized radial ( $p=.005$ ) and circumferential ( $p=.018$ ) strain rates.

**Table 6-10 Normalized strain rate ( $d(\epsilon)/d(LVP)$ ); \* denotes a  $p<0.05$  and † denotes a  $p<.01$  significant difference between the chronic IMR and control simulated conditions.**

		<b>Radial</b>	<b>Circumferential</b>
<b>Control</b>	<b>Animal</b>	$0.24 \pm 0.21$	$0.20 \pm 0.13$
	<b>Simulator</b>	$0.23 \pm 0.05$	$0.11 \pm 0.07$
<b>Chronic IMR</b>	<b>Animal</b>	$0.30 \pm 0.18$	$0.20 \pm 0.13$
	<b>Simulator</b>	$0.52 \pm 0.14$ †	$0.16 \pm 0.06$ *

#### **6.4.2 Part B: Effect of Annuloplasty on Subvalvular Tethering**

In part 1 of Specific Aim 3, *in vitro* simulations were demonstrated to mimic the systolic MV geometry, leaflet coaptation, regurgitation, and anterior leaflet strain of a healthy and chronic IMR ovine model. Given the unique ability of the simulator to mimic systolic MV function, the simulator was utilized to assess the sequential effects of IMR and annuloplasty on mitral regurgitation, leaflet coaptation, and tethering forces of the strut and intermediary chordae tendineae.

All raw data for the explanted mitral valves studies in part B of Specific Aim 3 is presented in Appendix D. A catalog of the locations of the echocardiography data sets on the laboratory's electronic server can be found in Appendix E.

#### 6.4.2.1 Mitral Regurgitation

Mitral regurgitation was observed to significantly differ between experimental conditions (Table 6-11). Mean MR volumes expectedly increased from control to IMR ( $p<.001$ ). At the IMR condition, each regurgitation jet was asymmetric and originated from the tethered A3-P3 leaflets. Following IMR, MR volumes were significantly reduced with increasing levels of annuloplasty ring under sizing ( $p<.001$ ). While oversized annuloplasty reduced MR volumes from the IMR condition, MR volumes with oversized annuloplasty remained significantly greater than that of the control ( $p<.001$ ). Elimination of MR was successfully achieved with both true-sized and undersized annuloplasty. Both of these repairs resulted in MR volumes that were statistically not different from the healthy control.

**Table 6-11 Effect of the evaluated conditions on mitral regurgitation volume (MRV) and A2-P2 coaptation length (CL); asterisks (\*) and dagger (†) denote significant differences of  $p<.001$  relative to the healthy control condition and ischemic mitral regurgitation condition, respectively.**

Measurement	Healthy Control	Ischemic Mitral Regurgitation	Oversized Annuloplasty	True-sized Annuloplasty	Undersized Annuloplasty
MRV [mL]	$27.6 \pm 1.4$	$47.0 \pm 2.2 *$	$37.4 \pm 2.2 *†$	$27.5 \pm 1.2 †$	$24.9 \pm 1.2 †$
CL [cm]	$4.84 \pm 0.13$	$3.19 \pm 0.14 *$	$3.54 \pm 0.11 *$	$3.90 \pm 0.13 *†$	$4.75 \pm 0.16 †$

#### 6.4.2.2 A2-P2 Leaflet Coaptation Length

Leaflet coaptation length across the 12 to 6 o'clock annular diameter was observed to significantly differ between the tested conditions ( $p<.001$ ) (Table 6-11). The largest reduction in coaptation length was observed between the control and IMR condition

( $p < .001$ ). Reshaping the mitral annulus to an oversized or true-sized ring slightly improved coaptation length but these improvements remained significantly less than the coaptation length occurring in the control condition ( $p < .001$ ). Undersized annuloplasty was the only repair condition which successfully restored A2-P2 coaptation length to values statistically not different from the healthy control condition.

#### 6.4.2.3 Chordal Tethering from the Posteromedial Papillary Muscle

Simulating an inferior myocardial infarction resulted in significant changes in chordal tethering for the posteromedial PM's anterior strut and posterior intermediary chordae (Table 6-12). Anterior strut chordal forces were observed to approximately double with IMR (Figure 6-17). Compared to the IMR condition, undersized annuloplasty significantly reduced anterior strut chordal forces by approximately 27% ( $p < .05$ ). Despite this result, anterior strut chordal forces at each level of annuloplasty remained significantly larger than forces measured in the control condition (Table 6-12).

**Table 6-12 Effect of the evaluated conditions on anterior strut (AS) and posterior intermediary (PI) chordal forces [N] (mean  $\pm$  standard error) originating from the posteromedial (PM) and anterolateral (AL) papillary muscles; asterisks (\*) and dagger (†) denote significant differences ( $p < .05$ ) relative to the healthy control condition and ischemic mitral regurgitation condition, respectively.**

Papillary Muscle	Chordae Tendineae	Healthy Control	Ischemic Mitral Regurgitation	Oversized Annuloplasty	True-sized Annuloplasty	Undersized Annuloplasty
PM	AS	0.71 $\pm$ 0.08	1.23 $\pm$ 0.11 *	0.99 $\pm$ 0.10 * †	0.91 $\pm$ 0.09 * †	0.88 $\pm$ 0.08 * †
	PI	0.28 $\pm$ 0.03	0.55 $\pm$ 0.08 *	0.47 $\pm$ 0.07 *	0.47 $\pm$ 0.06 *	0.51 $\pm$ 0.07 *
AL	AS	0.62 $\pm$ 0.11	0.80 $\pm$ 0.14 *	0.72 $\pm$ 0.12	0.68 $\pm$ 0.11	0.66 $\pm$ 0.10 †
	PI	0.49 $\pm$ 0.09	0.71 $\pm$ 0.13 *	0.61 $\pm$ 0.11	0.55 $\pm$ 0.09 †	0.53 $\pm$ 0.09 †

Similar to the anterior strut chordae, the posterior intermediary chordal forces were observed to significantly increase with IMR (Table 6-12). However, statistically significant differences were not observed between the IMR condition and each level of annuloplasty. Among the tested conditions, posterior intermediary forces remained significantly greater than those observed during the control condition ( $p < .05$ ). While not statistically significant, posterior intermediary forces demonstrated an increasing trend from oversized to undersized annuloplasty (Figure 6-19). Following undersized annuloplasty, posterior intermediary chordal forces were only marginally reduced (by approximately 4%) from the IMR condition.

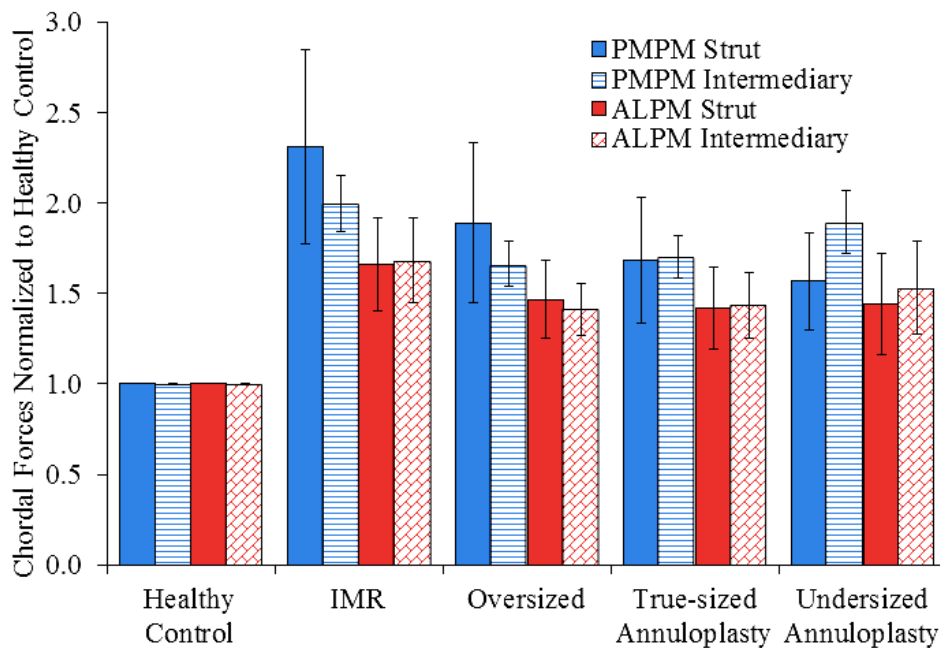


**Figure 6-19 Chordal forces from the posteromedial papillary muscle (PMPM) and anterolateral papillary muscle (ALPM) were normalized to the forces observed during the healthy control condition to demonstrate relative changes in cyclic chordal tethering with ischemic mitral regurgitation (IMR) and increasing degrees of annular under sizing.**

#### 6.4.2.4 Chordal Tethering from the Anterolateral Papillary Muscle

Similar to chordae from the posteromedial PM, simulating an inferior myocardial infarction resulted in significant changes to anterior strut and posterior intermediary tethering from the anterolateral PM (Table 6-12). Anterior strut and posterior intermediary forces were both observed to significantly increase with IMR ( $p < .05$ ). With increasing levels of annular under sizing, anterior strut chordal forces were found to significantly decrease between the IMR and undersized annuloplasty condition ( $p < .05$ ). Similarly, posterior intermediary chordal forces were observed to significantly decrease from the IMR condition to true-sized ( $p < .05$ ) and undersized ( $p < .05$ ) annuloplasty respectively.

#### 6.4.2.5. Chordal Tethering Forces Summed by Papillary Muscle

The strut and intermediary chordal forces from each PM were summed to examine if differences in cyclic tethering exist between each PM (Table 6-13). For both PMs, significant differences in summed chordal forces were observed between the tested conditions. For the posteromedial PM, summed forces were significantly greater than the control condition during IMR ( $p < .05$ ) and each of the annuloplasty conditions ( $p < .05$ ). Compared to IMR, summed forces on the posteromedial PM were observed to significantly decrease with oversized annuloplasty ( $p < .05$ ), true-sized annuloplasty ( $p < .05$ ), and undersized annuloplasty ( $p < .05$ ).

**Table 6-13 Effect of the evaluated conditions on strut and intermediary chordal forces [N] summed by papillary muscle; asterisks (\*) and dagger (†) denote significant differences (p<.05) relative to the healthy control condition and ischemic mitral regurgitation condition, respectively.**

Papillary Muscle	Healthy Control	Ischemic Mitral Regurgitation	Oversized Annuloplasty	True-sized Annuloplasty	Undersized Annuloplasty
Posteromedial	0.98 ± 0.08	1.76 ± 0.11 *	1.50 ± 0.10 * †	1.41 ± 0.09 * †	1.42 ± 0.11 * †
Anterolateral	1.01 ± 0.12	1.41 ± 0.19 *	1.24 ± 0.18 *	1.18 ± 0.16 †	1.14 ± 0.14 †

Summed forces on the anterolateral PM were observed to significantly increase from the control condition to IMR and oversized annuloplasty (Table 6-13). Compared to IMR, summed forces were observed to statistically decrease at true and undersized annuloplasty (p<.05), respectively. While not reaching statistical significance, summed forces on the posteromedial PM were observed to be greater than those on the anterolateral PM at IMR and at each level of mitral annuloplasty.

## CHAPTER 7

### DISCUSSION

#### 7.1 Introduction to the Discussion

Three specific aims were evaluated in this work. In Specific Aim 1, a novel transducer was developed to measure the radially directed forces that may act on devices implanted to the mitral annulus. In an ovine model, radial forces were found to statistically increase with left ventricular pressure and were reduced in the setting of IMR. In Specific Aim 2, the suture forces required to constrain true-sized and undersized annuloplasty rings to the mitral annulus of healthy ovine subjects was evaluated. Suture forces were observed to be larger on the anterior aspect of the rings and were elevated with annular undersizing. In Specific Aim 3, an *in vitro* simulator's ability to mimic healthy and IMR ovine mitral valve function was evaluated. After understanding the accuracy of the model, the *in vitro* IMR model was used to evaluate the progressive effects of annuloplasty undersizing on strut and intermediary chordal tethering. Compared to the IMR condition, increasing levels of undersizing annuloplasty significantly reduced regurgitation, increased coaptation, reduced posteromedial papillary muscle strut chordal forces, and reduced intermediary chordal forces from the anterolateral papillary muscle.

Similar to the organization of the Results Chapter, the Discussion is organized by Specific Aim. Specific Aim 1, 2, and 3 are sequentially presented in Sections 7.2, 7.3,

and 7.4, respectively. Each discussion additionally includes the limitations and clinical implications of the results.

## **7.2 Specific Aim 1**

### **7.2.1 Discussion**

Ejection of the heart's blood to the systemic circulation requires the left ventricle to generate enough pressure to open the aortic valve leaflets and empty the LV volume. This critical function is accomplished by the myocardium aligned circumferentially in the LV wall. During ventricular systole, the myocardium contract and reduce the LV diameter by generating forces that act along the direction of each myocardial fiber. These forces not only facilitate the generation of LVP, but at the basal level, reduce the mitral annular area and compress devices implanted to the mitral annulus. The septal-lateral and transverse forces measured in Aim 1 are vector components of the circumferentially generated myocardial forces.

In comparison to prior studies, the radially directed forces measured within the healthy animals were in good agreement with the magnitudes previously reported [75,76]. The maximum forces reported to act on prosthetic Edwards-Duromedics mitral valves (6-8 N) in a porcine subject are similar to the maximum values reported herein (4.3-6.9 N) at comparable mean peak LVP (130 vs. 125 mmHg) and heart rate (144 vs. 130 beats/min) [75]. A direct comparison between the directions of these maximum forces however cannot be made. Hasenkam reported the maximum force to act 30°



clockwise from the natural intercommissural line whereas the present study was limited to measurements in the septal-lateral and transverse directions.

Similar to our results, Shandas et al [76] found the maximum annular force on St. Jude Medical Biocor<sup>®</sup> stented prosthetic valves (between 4.4 and 13.9 N) to act in the septal-lateral direction. Compared to the present study, this larger range of peak force is likely due to the comparably smaller number of experimental subjects (n=2) and the limitations of using 3D intravascular ultrasound to map 2D deformation of the studied stented valves. A key difference however was the timing of the peak force. Shandas described the peak force to occur during atrial contraction whereas our results are in good agreement with Hasenkam to occur during mid-systole. We believe the later timing to be correct as mid-systole would coincide with near peak LV contraction and thus peak force.

A recent study by Jensen et al. measured the forces in traction sutures placed between the right fibrous trigone and the P1, P2, and P3 annular segments [124]. No difference in force was found between the P1, P2, and P3 segments across all levels of annular under sizing. The peak forces at 32% annular under sizing were  $1.2 \pm 0.9$  N,  $1.5 \pm 1.0$  N, and  $0.8 \pm 0.2$  N for the trigone-P1, trigone-P2, and trigone-P3 segments, respectively. The maximum total suture forces in the mitral plane during downsizing increased from  $0.12 \pm 0.03$  N to  $3.5 \pm 1.3$  N ( $p < .005$ ). While the forces measured in the aforementioned study are fundamentally different from the forces measured herein, these studies provides supplementary information for the forces which may push or pull on devices implanted in the mitral annulus.

In the healthy animals, the cyclic change in septal-lateral forces was found to be larger than the cyclic change of forces in the transverse direction. This directional

difference is supported by a similar study describing the areal reduction of the mitral annulus throughout the cardiac cycle. Using sonometric crystals to three-dimensionally map the mitral annulus within 55 ovine subjects; Rausch et al. [46] found the septal-lateral diameter to have a larger mean peak reduction (12.06%) than the transverse diameter (5.51%) given by  $p < .001$ . This result supports our findings in that a greater circumferential shortening of myocardial fibers aligned near the posterior annulus, results in not only a greater reduction in septal-lateral diameter but a greater vectorially resolved radial force.

When comparing the results of the healthy and IMR animal groups an inferior LV infarction significantly decreased septal-lateral forces while modestly decreasing those in the transverse direction. This can be explained by the fact that an inferior infarction not only impairs the ability of the infarcted myocardium to contract, but additionally alters the cross-sectional geometry of the LV [41, 54, 125-127]. Due to infarction, the magnitudes of circumferentially directed forces in the postero-inferior wall are reduced and are directionally more oblique with respect to the geometric center of the LV. As a result, the relative contributions of the postero-inferior myocardium to the radially directed septal-lateral and transverse forces are reduced. We believe the septal-lateral force was decreased to a greater extent due to ligation of the OM<sub>3</sub> coronary artery which has been previously demonstrated to impair more of the posterior wall [41, 125-127].

Lower forces observed in the chronic IMR animals have important implications in the development of minimally invasive and transcatheter IMR devices. These forces can inform bench and computational studies to evaluate the structural durability and relevant failure modes of these devices. International Standards Organization (ISO) standards and

Food and Drug Administration (FDA) guidelines recommend evaluating these devices under cyclic forces at magnitudes at least as severe as those anticipated *in vivo* under hypertensive conditions [128, 129]. While septal-lateral and transverse forces were observed to be reduced in the presence of IMR, a reasonable safety margin needs to be maintained to ensure long-term device durability and patient safety [130].

Findings within healthy animal subjects demonstrated directional differences in the change in force throughout the cardiac cycle. These differences and their exacerbation with increasing LVP can inform the structural strengthening of devices and worst-case loading conditions. Despite these findings, directional differences were not observed within the chronic IMR animals. An inferior infarction was found to significantly decrease septal-lateral forces, but not to a magnitude that was statistically different from those measured in the transverse direction. While transverse forces were consistently lower in the chronic IMR group, they were statistically not different from transverse forces measured in healthy subjects.

In addition to cyclic force magnitudes, the rates at which these forces increase during ventricular contraction carry equal importance. These rates can more accurately inform device testing and the use of device materials (e.g., polymers) with rate dependent behavior [128-130]. The rates measured herein were found to significantly increase with peak LVP, but did not significantly differ between directions and groups. While statistically significant differences in  $dF/dt$  were not observed between groups in the septal-lateral direction, we believe the large differences in magnitude are representative of a meaningful difference that might be observed to be statistically significant with a larger sample size. When combined with the peak magnitudes of these cyclic forces,

measured rates will contribute to more accurate experimental and computational models that further assist in optimizing device materials, design, durability and safety.

The translation of the measured chronic IMR annular forces in the ovine model to that which may be anticipated in IMR patients requires careful attention. Healthy ovine animals and humans have been compared previously and shown to possess similar mitral annular areas, LV mass and wall thickness, and comparable LVP and  $d(LVP)/dt$  [1,131]. Ligation of the obtuse marginal coronaries infarcts approximately 20% of the LV mass, includes the posteromedial papillary muscle, and produces increasingly more severe MR with progressive LV remodeling [41,125-127]. Similar to clinical descriptions, abnormalities and reductions in both LV and MV contractility are observed with significant increases in end systolic and diastolic LV volumes [41,132,133]. While the size and age of infarcts in IMR patients widely vary, LV wall motion abnormalities are overwhelmingly located in the postero-inferior aspect of the LV, and usually involve the posterior papillary muscle [54].

Given that our forces were measured under anesthesia and within the post-cardioplegic heart, we believe mitral annular forces within humans suffering from a posterior infarct to be of greater magnitude than the forces reported herein at 125 mmHg peak LVP. The forces expected in the human mitral annulus may present greater directional heterogeneity as coronary disease may be more widespread, diffused, and affect global LV contraction. We hypothesize a greater degree of localized myocardial infarction may result in a disproportionate systolic annular area reduction and potential shearing of devices in the mitral annulus. Moreover, annular under sizing as with restrictive mitral annuloplasty may differ from the results presented herein as the ring

will likely undergo cyclic tension from a contracting and grossly dilated LV. Future studies are required to not only describe these force profiles, but also understand the potential heterogeneity introduced by reshaping the mitral annulus to a given device.

Beyond in-plane forces, it is important to note that out-of-plane forces also exist. Jensen et al [118,119] were the first to describe the magnitude and distribution of these forces on flat and saddled shaped annuloplasty rings. Although they are of lower magnitude, they play an equally important role in understanding the forces that may act on mitral annular devices. Currently no methods exist to resolve the three-dimensionality of mitral annular forces; however, we believe those acting within the annular plane are of greatest magnitude. Although challenging, future studies may wish to consider the magnitude of forces acting circumferentially around the mitral annulus. Combined with various models of myocardial strain mapping, material properties of the mitral annulus may be determined and computational models more accurately employed.

Despite the advantages of the present study, several limitations exist in measuring these radially directed forces. Calibration of each transducer within our well-defined apparatus may not fully represent device fixation within the mitral annulus. Out-of-plane deformation was found to influence transducer signals. While out-of-plane transducer deformation was believed to be minimized by constraining the annulus to the semi-rigid flat transducer, it was not possible to determine how much out-of-plane bending contributed to observed forces. Although care was taken to match each transducer to the subject's annular size, exact matching was not likely achieved. Implantation of one device in a healthy subject inadvertently induced trace mitral regurgitation. The

magnitude of forces measured within the chronic IMR model are likely to be dependent on infarct size and may change with a lesser or greater degree of myocardial infarction.

Described forces are limited to this IMR model and may not represent the forces that may be seen in other mitral etiologies. As IMR repairs aim to reshape and reduce mitral annular area, transducers implanted within our chronic IMR subjects were true-sized to the enlarged mitral annulus. This was done to reduce any unknown effects of transducer-annular sizing on measured forces. In each study, the transducers were found to be either slightly undersized or exhibit a snug but not oversized fit. Absolute forces experienced by each device due to implantation and function were difficult to quantify due to observed variations in the diastolic forces from combined changes in annular contractility. For these reasons, the change in force throughout the cardiac cycle is reported. As implantation of any device will likely alter the native mitral annular mechanics, any forces measured may not be equal to those with an implanted device. As all studies were terminal, the long-term impact of these devices on left heart function was not assessed.

### **7.2.2 Clinical Implications**

Mitral annular forces were measured for the first time in a healthy and chronic IMR animal model. Our findings provide a foundation for not only the forces that exist but the mean rates at which they are generated during left ventricular contraction. Our new understanding for the timing, magnitude, directionality, and variation of these forces with ventricular afterload will improve device development and testing. These data may be used to refine mitral annular device development and evaluation via finite element

modeling, fatigue testing, and regulatory assessment. With improved knowledge for the forces which may act on implanted annular devices, these data will ultimately assist in optimizing device durability, flexibility, and safety.

## **7.3 Specific Aim 2**

### **7.3.1 Annuloplasty Ring Stress Transducer**

The stresses imparted on the ring at implantation were approximately 4-fold larger than the cyclic changes in stress throughout the cardiac cycle. From these initial results, implantation of the rigid ring transducer may have restricted the ability of the surrounding myocardium to systolically shorten. This can be explained by the fact that the ring transducer possessed a core whose relative thickness was 3 to 4 fold larger than commercially available rings. Results from implanting the rigid ring however compare favorably to previously observed reductions in annular dynamics from rigid ring implantation [134].

Understanding annuloplasty ring stresses can aid in the improvement of ring design and develop a greater understanding for the mechanistic relationship between ring implantation and LV function. Evaluating the relationship between mitral annular geometries and ring stress may lead to improvements for optimizing complete rigid ring geometry and materials. Measured in-plane and out-of-plane stresses that are specific to differing ring designs can aid in identifying areas of elevated stresses and develop methods or techniques to reduce them. Moreover, these transducers can aid in

understanding how increasing the number of ring-annulus sutures may impact regional ring stresses and basal LV function.

While it was desired to isolate the magnitude and direction of forces acting on the annuloplasty ring, it was not possible to isolate directional forces through the use of a calibration apparatus. Since annuloplasty transducers are complete rings, a force applied to a given ring location will affect the material deformation at other ring locations. A ring deformation that is measured by a strain gage therefore can be the result of an infinite combination of directional forces acting at locations other than the intended calibrated location and direction. As a result, this pilot study aimed to quantify the ring material stresses that are a result of the multidirectional loading for which implanted annuloplasty ring endure.

Several limitations exist in this study. In comparison to commercially available annuloplasty rings, the developed transducer is larger due to limitations in strain gage size. Measured ring stresses were likely affected by suture location and tie-down order. Increasing the number of implantation sutures may reduce ring stresses, but an optimal ratio of sutures to ring-annulus geometry is currently unknown. The physiological benefit of adding more sutures to reduce ring stress for a given ring-annulus geometry is also unknown and should be a subject of further investigation. Carefully controlling ring transducer manufacturing, methods of surgical implantation and the number of annular-ring sutures will be critical for the success of future studies.



### **7.3.2. Annuloplasty Ring Suture Forces**

For the first time, the cyclic tensile forces required to restrain true-sized and undersized annuloplasty rings to the mitral annulus of healthy ovine animals were quantified. These data revealed preliminary insight to the variations in cyclic suture forces by ring-annulus sizing, suture position, ring region, and left ventricular pressure. Throughout the cardiac cycle, cyclic forces were observed to reach their maximal values during isovolumetric contraction. This timing is consistent with the timing of maximal mitral annular radial forces in Specific Aim 1 and maximal ring stresses in the pilot study of Specific Aim 2.

All suture forces (regardless of ring position) were averaged for each of the true-sized and undersized rings to assess the effects of ring-annulus sizing and elevated levels of LVP. These preliminary results demonstrated undersized ring suture forces were approximately 41%, 38%, and 34% larger than true-sized ring suture forces at peak LVPs of 100, 125, and 150 mmHg, respectively. Based on these observed differences, the cyclic forces at each suture location were compared. Distinct similarities in the location of the largest and smallest suture forces were observed (Figure 7-1). For both groups of ring annular sizing, the largest forces were observed between the left and right fibrous trigones while the smallest forces were at the 7 o'clock suture position. Moreover, the overall trend in force magnitude by suture position was similar between the ring-annulus sizing groups and levels of LVP (Figure 7-1). While preliminary, the overall trends for force magnitude by suture position are believed to be in part due to suture securing order. Future studies are required to evaluate the effects of suture securing order on suture force profiles.

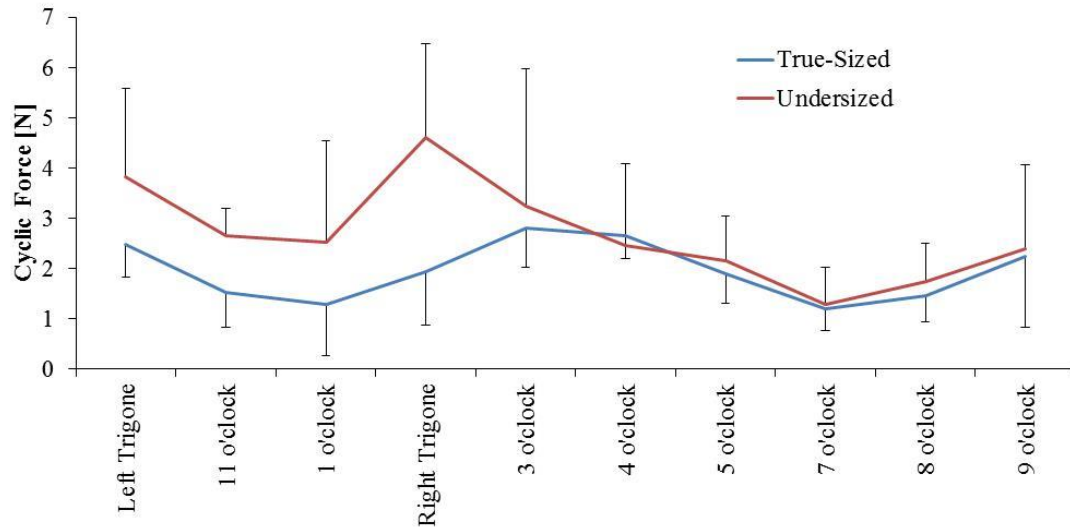


**Figure 7-1 Overall trends for force magnitude by suture position at an LVP of 125 mmHg.**

Suture forces of the undersized rings were predominately greater than those measured for true-sized rings at each level of LVP (Table 6-7). The largest differences in cyclic force were found to exist at sutures located between the left and right fibrous trigones. When suture forces were averaged by ring region (anterior vs. posterior), the anterior region of undersized rings exhibited a mean force that was greater than the posterior region of undersized rings. The anterior region of undersized rings was additionally found to be larger than both the anterior and posterior regions of true sized rings. Interestingly, the mean force on the posterior portion of the undersized rings was approximately equal to mean forces for both regions of the true-sized rings.

The increased forces measured along the anterior annulus of the undersized annuloplasty rings are likely the result of a blunting of the normal annular saddle shape with the flat undersized annuloplasty ring. During systole the saddle shape of the anterior annulus is accentuated with the mid-anterior annulus being “elevated” toward the atrium

by the filling of the aortic root and the fibrous trigones being “depressed” toward the ventricle by LV contraction. In a healthy heart, a flat undersized annuloplasty ring prevents this normal accentuation. The increased forces measured along the anterior annulus and fibrous trigones were likely the result of the annulus pulling away from the flat ring in these regions. The posterior annulus likely produces lower forces and smaller force variations throughout systole because its relatively flatter geometry is more stable throughout the cardiac cycle and similar to the flat annuloplasty ring.

These data provide preliminary insights and implications for annuloplasty ring design. The salutary effects of saddle shape annuloplasty on leaflet geometry and leaflet stress have been described [51]. These have included lowering mitral leaflet stresses and reducing chordal tethering. The data presented here also suggest saddled rings may potentially reduce suture forces on the anterior annulus. To fully understand these effects, future studies will evaluate the difference in suture forces between flat and saddled annuloplasty rings. These studies will additionally evaluate if regional LV distortions associated with IMR can exacerbate posterior ring suture forces. These data will provide critical knowledge for patient-ring selection and understanding ring dehiscence.

To better understand what may contribute the most to ring dehiscence, careful comparison of observed forces to those which may cause suture failure, knot failure, or annular tissue tearing is required. A previous study evaluated the strength of surgeon knots thrown from 3-0 Ti-Cron [8]. Five suture throws decreased the ultimate suture holding strength from 27 to 17.8 N. While 2-0 sutures are expected to exhibit a larger holding strength, results from 3-0 sutures are approximately 120% greater than the maximum force measured in this study (8.1 N at 150 mmHg peak LVP).

In comparison to suture and suture knot failure, annular tissue tearing may be a more likely failure mechanism in ring dehiscence. Among patients with varying MV disease, single sutures have been shown to tear from MV annular tissue with a mean force of  $6.0 \pm 4.5$  N [9]. While this study used only 10 sutures to implant the undersized ring (~16-20 used for a IMR patient), the magnitude of annular tissue tearing forces is within the range of forces measured herein. Future studies are required to understand the effects of suture number on measured forces and the resulting potential for annular-tissue tearing.

In our ongoing studies, evaluating the relative suture holding strength at differing annular locations will provide additional insight to the mechanisms of annular-tissue tearing and suture dehiscence. The observation that cyclic suture forces are greater for an undersized ring's anterior region is in part paradoxical given suture dehiscence is more commonly observed on the posterior annulus. This may suggest the suture holding strength of the aorto-mitral curtain may be greater than that of the posterior mitral annulus. This hypothesis could be evaluated in ex-vivo studies by carefully controlling for suture bite width and depth around the circumference of the annulus. Sutures placed in the mitral annulus may be pulled in a controlled fashion whose tension during pulling and tissue tearing may be recorded by a load cell.

Despite the advantages of the present study, several limitations exist. Measured forces were likely affected by suture bite width, bite depth, suture securing order, and use of anesthetic isoflurane. While isoflurane has been demonstrated to depress LV contractility [135], measurements at elevated LVP provide insight to the range of forces which may be anticipated in the awake, extubated, and ambulating animal. The use of

dobutamine to achieve elevated levels of LVP increased the subject's heart rate from 97 to 110 and 150 beats/min. Future studies will additionally evaluate the effects of heart rate on observed suture forces. All measurements herein are limited to Physio™ annuloplasty rings and healthy left ventricles. Future studies will aid in understanding the effects of ring shape, annular sizing, LVP, and LV dilatation on observed ring suture forces.

### **7.3.3. Clinical Implications**

The presented preliminary study was successful in assessing the feasibility of developing a transducer to quantify the regional stresses imparted on a flat mitral annuloplasty ring due to implantation and cyclic annular contraction. Understanding annuloplasty ring stresses can aid in the improvement of ring design and develop a greater understanding for the mechanistic relationship between ring implantation and LV function. Evaluating the relationship between mitral annular geometry and ring stress may lead to improvements for optimizing complete rigid ring geometry and materials. Measured stresses that are specific to differing ring designs can aid in identifying areas of high stress and develop methods or techniques to reduce them. Future studies should evaluate the effect of differing annuloplasty ring sizes, geometries, and implantation methods. The determination of these endpoints will significantly contribute to improved knowledge for the annulus-ring stresses, their relationship with LV function, and the safer development of surgical techniques and devices for MV repair.

## 7.4 Specific Aim 3

### 7.4.1 Assessing the Accuracy of the In Vitro Mitral Valve Simulator

Simulated changes in systolic MV geometry from a healthy to chronic IMR ovine model were modeled within the Georgia Tech Left Heart Simulator. When simulating a chronic IMR MV geometry, significant decreases in coaptation length and significant increases in coaptation depth and tenting area were observed as clinically described [24,25,26,28]. These changes in leaflet coaptation were accompanied with MR jets of a magnitude similar to that observed in the ovine subjects. In comparison to the simulated controls, a chronic IMR MV geometry resulted in significant increases in both radial and circumferential anterior leaflet strains. This can be explained in that the IMR geometry increases the leaflet area exposed to the transmitral pressure resulting in a greater force and stretch within the leaflet tissue.

The annular MV geometric changes and MR observed within our animals are in good agreement with previous studies [33,41,79,127]. Since the coronary anatomy varies very little between sheep and they do not form collateral vessels, these sheep provide a reliable and repeatable model of chronic IMR [127]. Due to the precise control that's allowed by the simulator's components, the simulated annular dilatation and PM displacement is also very repeatable. During valve selection, great care was given to selecting valves of similar size to that in-vivo. While similar in size, the number of chordae per valve likely differed as did their geometric insertions into the PMs and leaflets. Even with this variability, the standard deviations found in the *in vitro* MR fractions, coaptation characteristics, and strain was reduced in comparison to previous studies [107,110,111,115].

Given the consistency of both models, demonstrating negative results with a larger sample size would still not supersede or overcome the limitations of the *in vitro* simulator. For these reasons, the negative results reported herein are meaningful and highlights the unique ability of the simulator to mimic the systolic valvular distortions, coaptation characteristics, and anterior leaflet strain of a chronic IMR ovine model. These results additionally demonstrate the repeatability of the simulator and its ability to detect small differences between experimental conditions that are difficult in animal or human studies.

For type IIIb dysfunctions, the surgical reconstructive goals are to cease MR and promote reverse LV remodeling [1,24,25]. The effectiveness of IMR repairs is dependent on the repair's ability to compensate for the distended LV by restoring coaptation and ceasing MR during systolic closure [26,28,87]. For these reasons, *in vitro* simulators must aim to mimic the systolic closure of the leaflets; and moreover, aid in developing new methods and or techniques to maximize post-repair coaptation. Hence, the ultimate goal of our simulator is to mimic the systolic closure of the leaflets and provide a platform to investigate how to improve it in repair conditions.

Several limitations are associated with both the *in vitro* simulator and the methodologies used in this study. The described mitral valve simulator can recreate the systolic geometric configurations of the mitral valve but at current does not incorporate the intricate mechanics associated with valvular-ventricular interaction. Its inclusion would likely increase the accuracy of mimicking the dynamic *in vivo* valve function whose effects should be isolated in future studies. While at current the model can focus

on the geometry of the annulus, leaflets, and PMs, evaluating repairs that directly affect the ventricle will require appropriate *in vivo* geometric boundary conditions.

The comparison of our simulated results is limited to an extensively studied inferior IMR ovine model and does not emulate the valvular distortion and function that may be seen in other etiologies. The IMR ovine model's resulting valvular geometry are likely dependent on infarct size and may change with a lesser or greater degree of myocardial infarction. The evaluation of leaflet coaptation was limited to the A2-P2 annular plane as the ability to quantify coaptation along the A3-P3 plane was limited due to the thin poorly coapting leaflets. In future studies, a broader spectrum of IMR valvular geometries (i.e. from more diffuse coronary disease or anterolateral infarction) should be simulated with similarities assessed between the *in vitro* and *in vivo* models. Dynamic leaflet motion within the simulator should additionally be evaluated.

In our studied animals, implantation of the miniature sonomicrometry transducers to the anterior leaflet likely influenced the local deformation of the anterior leaflet and could be improved with the use of radio-opaque markers. For the computation of A2 leaflet strain, the number of transducers that could be localized to the ovine anterior leaflet was limited to 5 whereas in the GTLHS strain was computed with 9 markers. Using 9 markers improves on strain interpolation and improves the accuracy of the strain computations. While statistically significant differences between the measured parameters were not observed, the differences in the magnitudes between each metric are representative of that which may be observed with larger sample size.



### **7.4.2 Effect of Ischemic Mitral Regurgitation and Annuloplasty on Mitral Valve Function**

Computational tools exhibit significant potential for assessing how effective a proposed surgical strategy may be for addressing an IMR patient's MV anatomy and dysfunction. While advances in structural modeling and medical imaging have been made, modeling the complex chordae tendineae remains challenging. To date, most MV models have relied on idealized chordal structures whose inter-study variation has been demonstrated to impact modeling results [95,101]. These idealized chordae can number from a few dozen to several hundred, have no or limited branching, and exhibit poorly-defined insertions both in the mitral leaflets and papillary muscles. Compounding this uncertainty is the lack of experimental data providing boundary conditions for how the tethering of the chordae may change from IMR to UMA. Addressing both of these challenges is critical for improving IMR surgical planning tools and advancing their predictive capabilities.

Current best case scenarios utilize non-standard-of-care computed tomography (CT) imaging to generate high-resolution models of patient MV geometry and architecture [101]. The use of CT in this setting provides the ability to not only identify PM position but additionally demarcate major load bearing chordae that include the anterior strut and posterior intermediary chordae. Given CT may provide the best imaging modality to detail the MV's subvalvular structures, these models still require the appropriate boundary conditions to accurately predict the function and response of the chordae tendineae to both IMR and UMA.

This study was successful in generating an in vitro ground-truth data that may be used as boundary conditions for IMR computational models. This study was the first to simultaneously quantify leaflet coaptation, MR, anterior strut, and posterior intermediate chordal forces in the sequential transition from a healthy control, to IMR, and through multiple levels of undersized annuloplasty. As the algorithms and methods used in computational solvers can vary considerably, these data will aid the further development of computational tools to increase confidence in the simulated results. Additionally, these data reduce some uncertainty associated with extracting limited data from previous studies which may not directly represent IMR or UMA.

The presented data can enhance the modeling of idealized chordal structures within computational models (Figure 7-2). Computational models can assume a given chordal geometry and test the effect of IMR and or undersized mitral annuloplasty under similar transmitral hemodynamics. The computationally observed values or trends for leaflet closure and chordal forces can be compared to the results herein to parametrically evaluate how the chosen chordal geometry influences coaptation and tethering. Based on these differences, the assumed chordal geometry could be iteratively tuned in terms of both numbers and geometry to more accurately achieve a target coaptation geometry, MR, and force distribution. With a more finely tuned chordal architecture, higher confidence will exist for subsequent simulations of progressive disease or surgical repairs. These evaluations should be completed prior to the application of the developed methods to patient specific MV modeling.

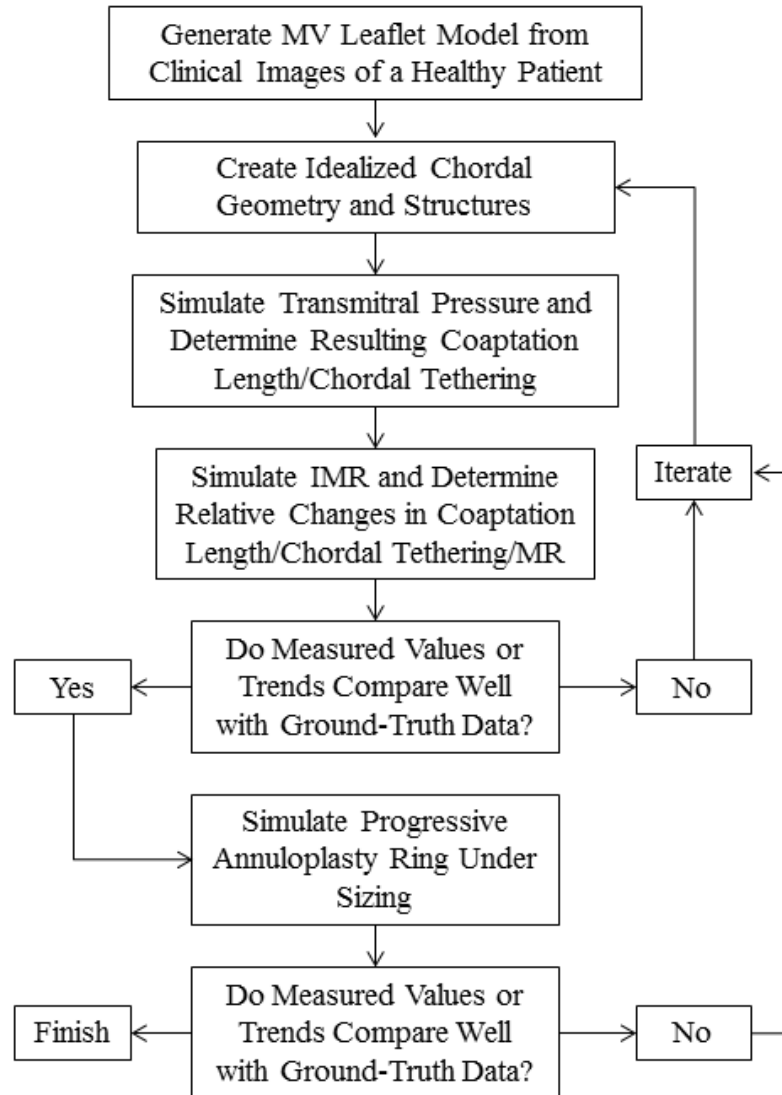


**Figure 7-2 Example iterative scheme for improving modeling of idealized chordal structures and geometry using the presented in vitro data.**

Summed chordal forces from each PM were used to examine if differences in cyclic tethering exist between each PM. Early studies by Jensen et al. demonstrated PM displacement to increase the cyclic PM forces [103]. With inferior myocardial infarctions, the posterior papillary muscle is displaced more than the anterior papillary muscle [1,2,24,41,54,55,58]. As a result, the summation of the intermediary and strut chordal forces is expected to be greater for the posteromedial PM. When the summed

forces between the PMs for each experimental condition were compared, no statistical differences were found (Table 6-13). This in part suggests that other chordae may be bearing additional loading and whose tethering also likely contributes to leaflet malcoaptation. Understanding the tethering of other chordae, their relationship to strut chordal tethering, and their effect on coaptation in IMR and annuloplasty may lead to improved mitral valve repair techniques [136,51].

Prior to this study, Nielsen et al. utilized a porcine model to evaluate the effect of acute IMR on marginal (also referred to in literature as primary) chordae tendineae forces for both PMs and leaflets [136]. For the anterolateral PM, anterior leaflet marginal chordal forces were observed to statistically increase from control to IMR ( $p < .05$ ), while non-significant decreases were observed in posterior marginal chordal forces. For the infarcted posteromedial PM, posterior leaflet marginal chordal forces remained relatively unchanged from control to IMR; however, anterior leaflet marginal chordal forces were significantly decreased ( $p < .05$ ). One explanation for these changes in chordal forces is that mitral leaflet malcoaptation (due to restrictive posterior leaflet motion) reduces the posterior leaflet surface area exposed to the LV pressure. The authors' hypothesized this mechanism to reduce the chordal forces of the posterior leaflet and contribute to further mitral leaflet malcoaptation [136].

In comparison to previous studies, the chordal forces reported herein are in good agreement with in vitro and large animal studies. For a healthy MV geometry, mean anterior leaflet strut and intermediary chordal forces have been found to range from approximately 0.65-1.22 N (compared to 0.62-0.71 N in this study) [51,104,106,137]. For the posterior leaflet, previous studies have reported a mean range of 0.25-0.78 N

(compared to 0.28-0.49 N in this study) [51,104,106,137]. Compared to the forces in this Aim, the larger range of chordal forces measured for a healthy MV geometry is attributed to the wide range of MV sizes used in previous studies. As the magnitude of chordal forces is directly related to the area of the MV leaflets exposed to the transvalvular pressure gradient, the greater the valve size, the larger the chordal forces [51].

While no previously published data exist for strut and intermediary chordal forces in IMR or UMA, an in vitro study has evaluated the effect of isolated papillary muscle displacement on strut and intermediary chordal tethering forces [104]. In the study, a parametric sweep of 5 mm displacements of both PMs in the apical, lateral, and posterior directions was performed. Significant increases in anterior strut and posterior intermediary chordal forces were observed when both PMs were displaced in either the apical or apical and lateral directions. Compared to the present study, these conditions most closely resemble a condition of true-sized annuloplasty. Our results compare favorably to that of Jimenez et al. by demonstrating anterior strut and posterior intermediary chordal forces significantly increase from the control condition with a true-sized annulus [104]. The results presented by Jimenez et al., Nielsen et al., and those herein provide complimentary information for how strut, intermediary, and marginal chordal tethering may be affected by either symmetric or asymmetric PM displacement towards the further development of computational MV models [104,136].

Despite the advantages of using an in vitro simulator to evaluate chordal tethering in IMR and annuloplasty, there are limitations associated with the experimental methods. A3-P3 leaflet coaptation was not quantified due to the difficulty in imaging the thin and poorly coapting ovine leaflets. The described MV simulator can recreate the systolic

geometric configuration of the mitral valve but at present does not incorporate the diastolic relaxation of the mitral annulus and systolic papillary muscle contraction. While in patients both the annular and papillary muscle dynamics may be ablated with the implantation of a complete rigid undersized annuloplasty ring and LV ischemia, the inclusion and intelligent variation of these parameters within the simulator would likely increase modeling accuracy.

Although only the anterior strut and posterior intermediate chordal forces were quantified, these chordae are known to bear the largest loads and have been demonstrated to most significantly contribute to leaflet malcoaptation in IMR [51]. With left ventricular dilatation and papillary muscle displacement, the strut and intermediary chordae tether the belly of each mitral leaflet and can lead to restricted leaflet motion, regional loss of coaptation, and MR [24,54,55,138]. Strut and intermediary chordae have additionally been implicated in UMA repair failure through long term post-operative left ventricular dilation, which further exacerbates sub-valvular tethering [26-28]. For these reasons, the data from this Aim can provide critical boundary conditions to further develop in silico platforms to model IMR and UMA.

### **7.4.3 Clinical Implications**

This study was successful in utilizing a novel technology to quantify mattress suture forces for true-sized undersized annuloplasty rings implanted in a healthy ovine model. The developed methods and technology provide the means to evaluate how patient-ring selection, ring geometry, implantation technique, and left heart geometry affect mattress suture forces and how their magnitudes relate to potential for suture dehiscence. The

determination of these endpoints will significantly contribute to improved clinical knowledge and improve annuloplasty ring design and surgical repair techniques. (Need to expand once the final data is analyzed and discussion finished).

Our findings in this study demonstrate the ability of an in vitro simulator to mimic A2-P2 leaflet coaptation, anterior leaflet strain, and MR characteristics of healthy and chronic IMR ovine animals at peak systole. These results provide a clinically relevant platform to evaluate the effect of IMR MV geometry on the effectiveness of current and future IMR repairs. While limitations do exist, the use of the simulator to evaluate IMR repairs can provide mechanistic understanding for the effect of a given repair on MV geometry, function, and mechanics. These findings should provide key insight to the effect of MV geometry on repair effectiveness and contribute to our clinical understanding of the geometric based mechanisms that restore valvular competence.

The present study provides for the first time a novel comprehensive data set for refining the ability of computational mitral valve models to simulate IMR and UMA. It is the first study to parametrically evaluate MV coaptation, MR, and strut and intermediary chordal forces in the sequential transition from a control to IMR and annuloplasty geometry. The quantification of these sequential effects is a significant finding and improves on the use of data from multiple studies whose materials and methods may not directly represent IMR or UMA [51]. This data is important for not only for improving computational modeling boundary conditions but also assessing modeling results. Combined with the results of previous studies [51], these data provide a ground-truth data set for the future development and refinement of MV computational models and future surgical planning tools.

## CHAPTER 8

### CONCLUSIONS AND FUTURE WORK

#### 8.1 Specific Aim 1

##### 8.1.1 Conclusions

- Mitral annular forces in the septal-lateral and transverse annular directions were measured for the first time in a healthy and chronic IMR animal model.
- In both animal groups, septal-lateral and transverse forces were observed to statistically increase with increasing levels of left ventricular pressure.
- The rate of change of septal-lateral and transverse forces during isovolumetric contraction were additionally quantified and demonstrated to significantly increase with increasing levels of left ventricular pressure.
- In healthy animals, septal-lateral forces were statistically greater than transverse forces at left ventricular pressures of 90, 125, 175, and 200 mmHg.
- In chronic IMR animals, an inferior left ventricular infarct significantly decreased septal-lateral forces while modestly lowering those in the transverse.
- The quantified force magnitudes and their variation will significantly aid the further development and evaluation of current and future mitral annular based devices.



### **8.1.2 Future Work**

Due to the complex dynamics of the left heart, devices that are implanted to the mitral annulus must undergo a complex three-dimensional loading environment. In combination, these forces may include planar compression, expansion, circumferentially directed stretching or compression, and out-of-plane bending (e.g. with the formation of the annular saddle). Quantifying these forces and understanding their physiological variation will significantly impact both clinical and industrial knowledge. Some of these studies may include but are not limited to:

- Understanding the effects of device-annular sizing on mitral annular forces.
- Quantifying the complex loads which may act on devices that are implanted to the heart's coronary sinus.
- Quantifying septal-lateral and transverse mitral annular forces in the setting of an anterior and or anterior/inferior myocardial infraction.
- Determining methods to more accurately quantify absolute forces (versus changes in force throughout the cardiac cycle).
- Understanding how annular force profiles may change when adjunct reconstructive techniques are employed (i.e. papillary muscle relocation, papillary muscle sling, ventricular reconstruction, leaflet augmentation, chordal transection, etc.).
- Understanding if a physiological impact exists between the measured annular forces and left ventricular function.

## 8.2 Specific Aim 2

### 8.2.1 Conclusions

- Mattress suture forces were quantified for the first time on true-sized and undersized mitral annuloplasty rings in a healthy ovine model.
- Preliminary results demonstrate trends in annuloplasty suture forces and their variation with ring location and LVP
- Suture forces for undersized annuloplasty rings were larger than those measured on true-sized rings.
- Regardless of ring sizing, the largest suture forces were observed at locations including and between the left and right fibrous trigones.
- Suture forces on the anterior portion of undersized annuloplasty rings were greater than suture forces observed on the posterior region of undersized rings and both the anterior and posterior regions of true-sized rings.
- The methods developed and the technology provide the means to evaluate how patient-ring selection, ring geometry, implantation technique, and left heart geometry affect mattress suture forces and how their magnitudes relate to potential for suture dehiscence.

### 8.2.2 Future Work

The data presented in Specific Aim 2 represent a small portion of an ongoing experimental investigation evaluating the influence of annuloplasty ring selection (with and without leaflet augmentation) on annuloplasty ring suture forces. Future studies in this investigation will include:

- Evaluating ring suture forces in a chronic IMR ovine model.
- Investigating the effects of anterior, posterior, and bi-leaflet augmentation on ring suture forces.
- Determining the effects of more extreme ring geometries (such as the profile 3D ring) on suture forces.
- Determining if correlations exist between ring selection, suture forces, and left ventricular function both pre and post intervention.
- Evaluating the effects of the number of sutures and the implantation method on observed ring-suture forces.

### **8.3 Specific Aim 3**

#### **8.3.1 Conclusions**

##### 8.3.1.1 Part A

- The Georgia Tech Left Heart Simulator was demonstrated to mimic the A2-P2 leaflet coaptation, anterior leaflet strain, and mitral regurgitation characteristics of healthy and chronic IMR ovine animals at peak ventricular systole.
- Reported results provide a foundation to evaluate the effect of IMR MV geometry on the effectiveness of current and future IMR repairs.
- Investigation of repairs targeting inferior myocardial infarcts should provide key insights into the effect of MV geometry on repair effectiveness and contribute to our clinical understanding of the geometric based mechanisms that restore valvular competence.

### 8.3.1.2 Part B

- For the first time, this aim provides a novel comprehensive data set for refining the ability of computational mitral valve models to simulate ischemic mitral regurgitation and undersized mitral annuloplasty.
- This study is the first to parametrically evaluate mitral leaflet coaptation, mitral regurgitation, and strut and intermediary chordal forces in the sequential transition from a control to ischemic mitral regurgitation and annuloplasty geometry.
- Combined with the results of previous studies, these data provide a ground-truth data set for the future development and refinement of mitral valve computational models and future surgical planning tools.

### **8.3.2 Future Work**

Bench-top simulators exhibit a number of advantages which allow for parametric evaluations of MV function. While MV function has been extensively studied *in vitro*, a multitude of studies may still be conducted to both improve clinical knowledge and better inform computational mitral valve modeling studies. Some of these studies may include, but are not limited to:

- Investigating the geometric limits of IMR repairs to evaluate to what extent certain repairs will fail with progressive LV dilatation.
- Creating a library of mitral valve data sets for providing realistic boundary conditions (leaflet closure, leaflet strain, chordal forces, flow, pressure, particle image velocimetry) for MV computational models.

- Evaluating the effectiveness of different subvalvular based mitral valve repair techniques.
- Transitioning *in vitro* modeling from functional to degenerative mitral valve disease scenarios.
- Incorporating contracting annulus and papillary muscles to evaluate their mechanical and dynamic effects on mitral valve function.

## **CHAPTER 9**

### **FUNDING SOURCES**

#### **9.1 Acknowledgement of Funding Sources**

Specific aim 1 was supported by a research grant awarded from the Food and Drug Administration (FDA1061718) and by grants from the National Heart, Lung and Blood Institute of the National Institutes of Health, Bethesda, MD (HL63954 and HL73021). Robert Gorman and Joseph Gorman were supported by individual Established Investigator Awards from the American Heart Association, Dallas, TX.

The ring stress transducer in specific aim 2 was supported by grants awarded from the National Heart, Lung, and Blood Institute (HL73021, HL63954 and HL090661). The authors would like to additionally thank James “Jim” McEntree for fabricating the titanium annuloplasty ring core and dedicate this manuscript in his memory. The suture force transducer study was supported by a grant from the National Heart, Lung and Blood Institute (R01HL113216).

Part A of specific aim 3 was supported by a research grant awarded from the National Institute of Health (R01 HL090661-02) and from the National Heart and Lung Institute (HL063954, HL073021, HL103723, and HL108330). Robert Gorman and Joseph Gorman were supported by individual Established Investigator Awards from the American Heart Association. Part B of specific aim 3 was supported by a research grant

awarded from the National Heart Lung and Blood Institute (R01 HL090661). We thank Phillips Medical systems for the use of an iE33 Matrix Echocardiography system.

Additional funding was provided by the generous contributions of Tom and Shirley Gurley.

## APPENDIX A

### SPECIFIC AIM 1 DATA

**Table A-1 Septal-lateral forces [N] for each of the healthy animals at each target level of peak left ventricular pressure.**

	Peak Left Ventricular Pressure				
	90 mmHg	125 mmHg	150 mmHg	175 mmHg	200 mmHg
Healthy Animal 1	3.7	4.7	5.2	5.9	6.3
Healthy Animal 2	5.1	6.9	7.6	8.3	9.2
Healthy Animal 3	4.4	5.9	6.5	7.3	7.4
Healthy Animal 4	2.6	4.8	5.2	5.4	4.9
Healthy Animal 5	3.8	4.9	5.8	6.0	6.1
Healthy Animal 6	3.6	4.3	5.3	5.5	6.4

**Table A-2 Septal-lateral force rate [N/s] during isovolumetric contraction for each of the healthy animals at each target level of peak left ventricular pressure.**

	Peak Left Ventricular Pressure				
	90 mmHg	125 mmHg	150 mmHg	175 mmHg	200 mmHg
Healthy Animal 1	35	106	108	130	142
Healthy Animal 2	83	170	252	307	346
Healthy Animal 3	97	176	203	227	205
Healthy Animal 4	40	46	51	50	60
Healthy Animal 5	107	118	119	125	145
Healthy Animal 6	99	142	167	172	181



**Table A-3 Transverse forces [N] for each of the healthy animals at each target level of peak left ventricular pressure.**

	Peak Left Ventricular Pressure				
	90 mmHg	125 mmHg	150 mmHg	175 mmHg	200 mmHg
Healthy Animal 1	2.5	4.7	5.4	4.3	4.1
Healthy Animal 2	3.5	5.2	6.3	5.9	3.6
Healthy Animal 3	2.0	2.5	2.6	2.9	2.8
Healthy Animal 4	2.0	3.4	4.9	5.3	4.3
Healthy Animal 5	3.2	3.5	4.6	4.2	3.8
Healthy Animal 6	2.3	3.2	3.5	3.3	2.5

**Table A-4 Transverse force rate [N/s] during isovolumetric contraction for each of the healthy animals at each target level of peak left ventricular pressure.**

	Peak Left Ventricular Pressure				
	90 mmHg	125 mmHg	150 mmHg	175 mmHg	200 mmHg
Healthy Animal 1	25	74	97	79	46
Healthy Animal 2	55	88	131	118	42
Healthy Animal 3	40	49	44	42	41
Healthy Animal 4	32	99	106	133	154
Healthy Animal 5	14	16	28	29	38
Healthy Animal 6	52	95	122	111	108

**Table A-5 Mean left ventricular pressure for each of the healthy animals at each target level of peak left ventricular pressure.**

	Peak Left Ventricular Pressure				
	90 mmHg	125 mmHg	150 mmHg	175 mmHg	200 mmHg
Healthy Animal 1	90	125	151	174	200
Healthy Animal 2	89	134	146	168	205
Healthy Animal 3	90	126	153	177	199
Healthy Animal 4	86	130	151	173	196
Healthy Animal 5	92	127	153	174	200
Healthy Animal 6	93	127	153	173	208

**Table A-6 Mean heart rate for each of the healthy animals at each target level of peak left ventricular pressure.**

	Peak Left Ventricular Pressure				
	90 mmHg	125 mmHg	150 mmHg	175 mmHg	200 mmHg
Healthy Animal 1	88	116	117	160	154
Healthy Animal 2	126	180	181	199	192
Healthy Animal 3	89	93	94	98	105
Healthy Animal 4	87	106	109	118	142
Healthy Animal 5	88	92	110	109	100
Healthy Animal 6	129	110	148	156	160

**Table A-7 Septal-lateral forces [N] for each of the IMR animals at each target level of peak left ventricular pressure.**

	Peak Left Ventricular Pressure				
	90 mmHg	125 mmHg	150 mmHg	175 mmHg	200 mmHg
IMR Animal 2	2.1	2.4	2.8	2.9	2.2
IMR Animal 3	1.8	2.2	2.9	3.7	3.9
IMR Animal 4	2.2	2.8	3.0	3.1	3.3
IMR Animal 5	3.1	3.5	4.0	4.4	4.5
IMR Animal 6	3.1	3.8	4.6	4.4	4.4
IMR Animal 7	2.9	3.0	3.7	3.8	3.6

**Table A-8 Septal-lateral force rate [N/s] during isovolumetric contraction for each of the IMR animals at each target level of peak left ventricular pressure.**

	Peak Left Ventricular Pressure				
	90 mmHg	125 mmHg	150 mmHg	175 mmHg	200 mmHg
IMR Animal 2	21	47	72	75	59
IMR Animal 3	56	35	58	69	83
IMR Animal 4	49	45	60	54	86
IMR Animal 5	38	34	58	66	78
IMR Animal 6	36	47	77	65	75
IMR Animal 7	32	44	57	64	60

**Table A-9 Transverse forces [N] for each of the IMR animals at each target level of peak left ventricular pressure.**

	Peak Left Ventricular Pressure				
	90 mmHg	125 mmHg	150 mmHg	175 mmHg	200 mmHg
IMR Animal 2	3.6	3.8	4.0	4.6	4.5
IMR Animal 3	2.6	3.3	3.6	3.6	3.3
IMR Animal 4	2.2	2.7	2.5	2.1	2.0
IMR Animal 5	1.6	2.0	3.1	3.4	2.6
IMR Animal 6	2.2	2.8	2.6	2.5	2.7
IMR Animal 7	1.1	1.6	1.4	1.2	1.0

**Table A-10 Transverse force rate [N/s] during isovolumetric contraction for each of the IMR animals at each target level of peak left ventricular pressure.**

	Peak Left Ventricular Pressure				
	90 mmHg	125 mmHg	150 mmHg	175 mmHg	200 mmHg
IMR Animal 2	43	64	68	87	83
IMR Animal 3	56	55	79	94	72
IMR Animal 4	31	33	42	29	36
IMR Animal 5	22	33	46	53	54
IMR Animal 6	23	43	79	114	95
IMR Animal 7	5	11	45	33	31

**Table A-11 Mean LVP for each of the IMR animals at each target level of peak left ventricular pressure.**

	Peak Left Ventricular Pressure				
	90 mmHg	125 mmHg	150 mmHg	175 mmHg	200 mmHg
IMR Animal 2	90	126	151	176	202
IMR Animal 3	96	120	152	180	197
IMR Animal 4	92	125	153	177	199
IMR Animal 5	94	125	150	181	202
IMR Animal 6	91	124	156	176	201
IMR Animal 7	94	126	151	177	192

**Table A-12 Mean heart rate for each of the IMR animals at each target level of peak left ventricular pressure.**

	Peak Left Ventricular Pressure				
	90 mmHg	125 mmHg	150 mmHg	175 mmHg	200 mmHg
IMR Animal 2	95	98	100	102	132
IMR Animal 3	105	117	122	130	140
IMR Animal 4	99	125	132	165	171
IMR Animal 5	81	110	112	119	132
IMR Animal 6	104	117	138	143	160
IMR Animal 7	93	100	102	121	128

## APPENDIX B

### SPECIFIC AIM 2 DATA

**Table B-1 Baseline characteristics of the healthy ovine animals.**

	True-Sized Animals				Undersized Animals			
	GTA	GTA	GTA	GTA	GTA	GTA	GTA	GTA
	4	5	8	10	2	3	6	7
Weight [kg]	52	62	65	43	72	70	54	52
Annulus Sized at Bypass (Physio™)	26	32	28	28	30	30	30	30
Implanted Ring Size (Physio™)	26	32	28	28	26	26	26	26

**Table B-2 Mean left ventricular pressure and heart rate for 10 consecutive cardiac cycles at the target left ventricular pressure for the healthy ovine animals.**

	Target Left Ventricular Pressure	True-Sized Animals				Undersized Animals			
		GTA	GTA	GTA	GTA	GTA	GTA	GTA	GTA
		4	5	8	10	2	3	6	7
Actual Left Ventricular Pressure [mmHg]	100	105	102	97	100	105	106	105	101
	125	126	125	125	126	129	125	130	132
	150	152	151	151	151	155	154	151	151
Heart Rate [beats/min]	100	89	102	150	90	97	108	130	99
	125	100	127	155	92	110	107	135	132
	150	123	129	166	96	150	111	146	130

**Table B-3 Mean suture forces [N] measured for cardiac cycles reaching a peak left ventricular pressure of 100 mmHg.**

		True-Sized Animals				Undersized Animals			
		GTA	GTA	GTA	GTA	GTA	GTA	GTA	GTA
		4	5	8	10	2	3	6	7
Ring Position	Left Fibrous Trigone	2.0	2.9	1.3	2.0	4.9	4.6	2.2	1.5
	11 o'clock	1.4	1.6	2.5	0.6	2.5	2.7	1.8	2.1
	1 o'clock	2.1	0.6	1.1	0.4	3.6	3.9	0.7	0.4
	Right Fibrous Trigone	1.7	0.6	2.4	1.5	3.9	5.1	1.7	6.2
	3 o'clock	1.7	2.5	1.7	2.5	1.4	1.6	5.9	1.3
	4 o'clock	1.6	2.4	2.1	2.3	0.2	3.0	3.0	1.8
	5 o'clock	0.9	1.9	2.7	1.3	2.0	2.9	0.8	1.5
	7 o'clock	0.8	1.0	1.7	0.7	0.9	0.3	1.5	2.0
	8 o'clock	1.0	1.4	1.5	0.8	1.0	1.9	0.6	2.5
	9 o'clock	3.0	2.8	2.3	0.5	3.2	3.3	0.4	1.3

**Table B-4 Mean suture forces [N] measured for cardiac cycles reaching a peak left ventricular pressure of 125 mmHg.**

		True-Sized Animals				Undersized Animals			
		GTA	GTA	GTA	GTA	GTA	GTA	GTA	GTA
		4	5	8	10	2	3	6	7
Ring Position	Left Fibrous Trigone	2.3	3.4	1.9	2.2	5.5	5.2	2.5	2.1
	11 o'clock	1.7	1.9	2.0	0.5	3.1	3.1	2.0	2.3
	1 o'clock	2.6	0.6	1.6	0.3	4.4	4.1	0.9	0.6
	Right Fibrous Trigone	1.9	0.8	3.3	1.7	4.9	5.9	1.9	5.8
	3 o'clock	1.8	3.7	2.7	3.1	1.7	1.9	7.4	2.0
	4 o'clock	2.0	2.9	3.0	2.7	0.3	3.4	3.9	2.1
	5 o'clock	1.2	2.2	2.5	1.6	2.4	3.2	1.0	1.9
	7 o'clock	1.2	1.0	1.8	0.8	1.1	0.4	1.4	2.2
	8 o'clock	1.3	1.6	2.1	0.8	1.2	2.2	1.0	2.6
	9 o'clock	3.4	3.3	1.6	0.5	3.7	4.0	0.7	1.3

**Table B-5 Mean suture forces [N] measured for cardiac cycles reaching a peak left ventricular pressure of 150 mmHg.**

		True-Sized Animals				Undersized Animals			
		GTA	GTA	GTA	GTA	GTA	GTA	GTA	GTA
		4	5	8	10	2	3	6	7
Ring Position	Left Fibrous Trigone	2.9	3.9	2.3	2.4	5.7	5.7	2.7	2.3
	11 o'clock	2.0	1.9	2.4	0.6	3.6	3.6	2.3	3.0
	1 o'clock	3.3	0.7	1.9	0.3	4.5	4.2	1.0	0.7
	Right Fibrous Trigone	2.3	1.2	4.1	2.0	5.6	6.6	2.0	5.8
	3 o'clock	2.0	3.8	3.1	3.5	1.7	2.1	8.1	2.2
	4 o'clock	2.1	3.4	3.3	3.0	0.2	2.3	4.5	2.8
	5 o'clock	1.6	2.6	2.8	1.8	2.8	3.6	1.1	2.2
	7 o'clock	1.0	0.9	1.9	0.9	0.9	0.6	1.5	3.0
	8 o'clock	1.4	1.7	2.3	0.7	1.3	2.6	1.0	2.5
	9 o'clock	3.6	3.7	1.8	0.7	4.2	4.7	0.7	1.6

## APPENDIX C

### SPECIFIC AIM 3 (PART A) DATA

**Table C-1 Healthy animal characteristics.**

	Weight [kg]	Heart Rate (beats/min)	Peak Left Ventricular Pressure [mmHg]	Annular Area [cm x cm]	Anterior Leaflet Height [mm]
MV03	36	87	93	6.4	18.5
MV07	41	110	114	6.5	18.2
MV09	37	81	101	6.3	16.8
MV11	42	95	97	6.2	17.6
GT28	37	92	100	6.3	17.7
GT29	35	121	105	6.6	19.5

**Table C-2 Healthy Animal A2-P2 leaflet coaptation characteristics.**

Animal Designation	Coaptation Length [mm]	Coaptation Depth [mm]	Tenting Area [cm x cm]
MV 03	3.6	2	0.27
MV 07	4.4	1.4	0.2
MV 09	4.6	1.6	0.18
MV 11	4.8	1.9	0.21
GTB 28	4.5	1.8	0.19
GTB 29	4.7	1.9	0.35



**Table C-3 Healthy Animal Anterior A2 Leaflet Strain and Strain Rate Normalized by d(LVP)/dt in the radial and circumferential leaflet directions.**

Animal Designation	Strain		Normalized Strain Rate	
	Radial	Circumferential	Radial	Circumferential
MV 03	0.050	0.003	0.03%	0.03%
MV 07	0.114	0.092	0.13%	0.20%
MV 09	0.176	0.001	0.24%	0.22%
MV 11	0.421	0.227	0.09%	0.11%
GTB 28	0.161	-0.054	0.56%	0.27%
GTB 29	0.308	0.109	0.40%	0.38%

**Table C-4 Ischemic mitral regurgitation animal characteristics.**

	Weight [kg]	Heart Rate (beats/min)	Peak Left Ventricular Pressure [mmHg]	Annular Area [cm x cm]	Anterior Leaflet Height [mm]	Percent of Left Ventricular Infarction
GTB05	37	89	93	12.6	18.7	15.8%
GTB07	38	99	105	9.9	18.6	20.0%
GTB08	37	91	106	10.4	19.4	20.1%
GTB10	42	96	102	13.4	18.9	19.2%
GTB22	36	124	107	8.3	19.1	18.0%
GTB23	37	98	108	7.8	20.1	17.7%

**Table C-5 Ischemic Mitral Regurgitation Animal A2-P2 leaflet coaptation characteristics.**

Animal Designation	Coaptation Length [mm]	Coaptation Depth [mm]	Tenting Area [cm x cm]
GTB 05	3.7	1.6	0.10
GTB 07	2.7	2.5	0.16
GTB 08	3.3	1.7	0.27
GTB 10	3.4	2.1	0.4
GTB 22	3.1	2.5	0.26
GTB 23	3	3.7	0.43

**Table C-6 Ischemic Mitral Regurgitation Animal Anterior A2 Leaflet Strain and Strain Rate Normalized by  $d(LVP)/dt$  in the radial and circumferential leaflet directions.**

Animal Designation	Strain		Normalized Strain Rate	
	Radial	Circumferential	Radial	Circumferential
GTB 05	0.144	0.094	0.33%	0.30%
GTB 07	0.139	0.013	0.13%	0.09%
GTB 08	0.358	-0.002	0.48%	0.16%
GTB 10	0.088	0.018	0.07%	0.04%
GTB 22	0.248	0.239	0.29%	0.40%
GTB 23	0.307	0.035	0.53%	0.19%

**Table C-7 Results of simulating healthy animal mitral valve geometry: A2-P2 leaflet coaptation characteristics.**

Experiment	Coaptation Length [mm]	Coaptation Depth [mm]	Tenting Area [cm x cm]
H	4.6	1.9	0.19
G	3.8	1.7	0.1
M	3.7	1.7	0.11
N	4.2	2.4	0.15
P	3.4	2.5	0.21
J	4.2	2.1	0.21

**Table C-8 Results of simulating healthy animal mitral valve geometry: Anterior A2 Leaflet Strain and Strain Rate Normalized by  $d(LVP)/dt$  in the radial and circumferential leaflet directions.**

Experiment	Strain		Normalized Strain Rate	
	Radial	Circumferential	Radial	Circumferential
H	0.37	0.17	0.16%	0.06%
G	0.04	0.02	0.22%	0.09%
M	0.33	0.10	0.21%	0.10%
N	0.19	0.05	0.19%	0.09%
P	0.46	0.11	0.22%	0.06%
J	0.55	0.22	0.31%	0.21%

**Table C-9 Results of simulating ischemic mitral regurgitation animal mitral valve geometry: A2-P2 leaflet coaptation characteristics.**

Experiment	Coaptation Length [mm]	Coaptation Depth [mm]	Tenting Area [cm x cm]
H	3.9	3.1	0.28
G	2.6	2	0.16
M	3.6	1.6	0.19
N	2.5	3.4	0.37
P	2.7	4.3	0.52
J	3	2.4	0.33

**Table C-10 Results of simulating ischemic mitral regurgitation animal mitral valve geometry: Anterior A2 Leaflet Strain and Strain Rate Normalized by  $d(LVP)/dt$  in the radial and circumferential leaflet directions.**

Experiment	Strain		Normalized Strain Rate	
	Radial	Circumferential	Radial	Circumferential
H	0.39	0.16	0.29%	0.10%
G	0.06	0.00	0.41%	0.16%
M	0.35	0.11	0.40%	0.10%
N	0.24	0.10	0.42%	0.18%
P	0.54	0.03	0.71%	0.12%
J	0.49	0.17	0.54%	0.23%

## APPENDIX D

### SPECIFIC AIM 3 (PART B) DATA

**Table D-1 Mitral regurgitation [mL] for each of the experiments and conditions.**

<b>Experimental Condition</b>	<b>Experiment</b>							
	<b>A</b>	<b>B</b>	<b>C</b>	<b>D</b>	<b>E</b>	<b>F</b>	<b>H</b>	<b>I</b>
Control	23.7	21.1	23.7	22.9	27.0	21.8	21.9	25.7
IMR	49.0	42.2	31.0	41.5	47.3	52.4	36.2	47.8
Oversized Annuloplasty	43.1	30.4	25.1	34.2	41.5	39.6	21.4	33.7
True Sized Annuloplasty	26.4	19.7	20.3	27.3	28.7	21.9	22.1	28.7
Undersized Annuloplasty	22.6	17.9	17.6	19.2	24.4	20.2	23.1	28.3

<b>Experimental Condition</b>	<b>Experiment</b>						
	<b>J</b>	<b>K</b>	<b>L</b>	<b>M</b>	<b>N</b>	<b>O</b>	<b>P</b>
Control	28.4	34.8	33.9	27.4	38.3	31.3	31.3
IMR	47.3	55.2	60.1	37.7	47.9	46.4	63.6
Oversized Annuloplasty	39.7	44.8	48.5	32.2	39.7	35.1	52.8
True Sized Annuloplasty	31.4	33.6	31.3	27.5	33.5	28.6	31.5
Undersized Annuloplasty	29.6	32.8	26.8	26.2	31.0	26.2	28.0

**Table D-2 Coaptation length [cm] for each of the experiments and conditions.**

<b>Experimental Condition</b>	<b>Experiment</b>							
	<b>A</b>	<b>B</b>	<b>C</b>	<b>D</b>	<b>E</b>	<b>F</b>	<b>H</b>	<b>I</b>
Control	0.59	0.48	0.48	0.54	0.53	0.48	0.41	0.47
IMR	0.36	0.33	0.41	0.33	0.29	0.35	0.33	0.31
Oversized Annuloplasty	0.37	0.35	0.43	0.34	0.32	0.37	0.34	0.28
True Sized Annuloplasty	0.43	0.32	0.51	0.41	0.36	0.41	0.35	0.43
Undersized Annuloplasty	0.56	0.46	0.45	0.52	0.49	0.49	0.38	0.48

<b>Experimental Condition</b>	<b>Experiment</b>						
	<b>J</b>	<b>K</b>	<b>L</b>	<b>M</b>	<b>N</b>	<b>O</b>	<b>P</b>
Control	0.45	0.49	0.38	0.51	0.49	0.47	0.50
IMR	0.39	0.33	0.18	0.36	0.27	0.29	0.27
Oversized Annuloplasty	0.40	0.37	0.27	0.36	0.36	0.33	0.40
True Sized Annuloplasty	0.41	0.41	0.32	0.39	0.35	0.33	0.41
Undersized Annuloplasty	0.52	0.55	0.35	0.54	0.41	0.43	0.48

**Table D-3 Cyclic force [N] for the anterior leaflet strut chord originating from the posteromedial papillary muscle for each of the experiments and conditions.**

<b>Experimental Condition</b>	<b>Experiment</b>							
	<b>A</b>	<b>B</b>	<b>C</b>	<b>D</b>	<b>E</b>	<b>F</b>	<b>H</b>	<b>I</b>
Control	0.95	0.61	0.77	0.90	1.25	1.17	0.63	0.70
IMR	1.68	1.22	1.63	1.52	1.82	1.91	0.97	1.23
Oversized Annuloplasty	1.58	1.06	1.51	0.51	1.30	1.60	0.85	1.09
True Sized Annuloplasty	1.10	1.09	1.40	0.55	1.15	1.48	0.78	1.03
Undersized Annuloplasty	1.05	1.06	1.40	0.57	1.07	1.42	0.79	0.99

<b>Experimental Condition</b>	<b>Experiment</b>						
	<b>J</b>	<b>K</b>	<b>L</b>	<b>M</b>	<b>N</b>	<b>O</b>	<b>P</b>
Control	0.73	0.02	0.62	0.49	0.92	0.42	0.50
IMR	1.20	0.21	0.90	0.79	1.00	1.31	1.07
Oversized Annuloplasty	1.02	0.17	0.86	0.77	0.86	1.10	0.67
True Sized Annuloplasty	0.88	0.14	0.80	0.73	0.93	1.07	0.60
Undersized Annuloplasty	0.81	0.11	0.81	0.70	0.95	1.00	0.61

**Table D-4 Cyclic force [N] for the posterior leaflet intermediary chord originating from the posteromedial papillary muscle for each of the experiments and conditions.**

Experimental Condition	Experiment							
	A	B	C	D	E	F	H	I
Control	0.16	0.22	0.33	-	0.28	0.26	0.38	0.35
IMR	0.28	0.23	0.61	-	0.36	0.57	0.51	0.62
Oversized Annuloplasty	0.25	0.16	0.64	-	0.37	0.38	0.42	0.49
True Sized Annuloplasty	0.27	0.26	0.63	-	0.36	0.40	0.40	0.44
Undersized Annuloplasty	0.32	0.32	0.87	-	0.34	0.42	0.43	0.45

Experimental Condition	Experiment						
	J	K	L	M	N	O	P
Control	0.20	0.56	0.30	0.14	0.33	0.38	0.04
IMR	0.38	1.12	0.86	0.29	0.83	0.92	0.13
Oversized Annuloplasty	0.33	0.98	0.67	0.31	0.82	0.73	0.07
True Sized Annuloplasty	0.31	0.90	0.77	0.30	0.70	0.72	0.09
Undersized Annuloplasty	0.29	0.89	0.97	0.30	0.64	0.70	0.13

**Table D-5 Cyclic force [N] for the anterior leaflet strut chord originating from the anterolateral papillary muscle for each of the experiments and conditions.**

Experimental Condition	Experiment							
	A	B	C	D	E	F	H	I
Healthy	0.82	0.29	0.89	1.84	0.75	0.60	0.04	0.44
IMR	0.50	0.62	0.76	2.21	0.37	1.15	0.17	0.52
125% Annuloplasty	0.51	0.52	0.77	1.91	0.45	0.91	0.15	0.43
True Sized Annuloplasty	0.57	0.52	0.73	1.69	0.46	0.77	0.16	0.49
Undersized Annuloplasty	0.55	0.49	0.68	1.60	0.44	0.70	0.19	0.56

Experimental Condition	Experiment						
	J	K	L	M	N	O	P
Control	0.14	0.72	0.23	0.96	0.48	0.41	0.63
IMR	0.46	1.19	0.27	1.32	0.88	0.52	1.06
Oversized Annuloplasty	0.40	1.10	0.26	1.32	0.79	0.37	0.91
True Sized Annuloplasty	0.38	1.09	0.17	1.30	0.77	0.40	0.73
Undersized Annuloplasty	0.37	0.95	0.18	1.30	0.77	0.38	0.68

**Table D-6 Cyclic force [N] for the posterior leaflet intermediary chord originating from the anterolateral papillary muscle for each of the experiments and conditions.**

<b>Experimental Condition</b>	<b>Experiment</b>							
	<b>A</b>	<b>B</b>	<b>C</b>	<b>D</b>	<b>E</b>	<b>F</b>	<b>H</b>	<b>I</b>
Healthy	0.49	0.17	0.20	0.67	0.34	0.03	0.90	0.34
IMR	0.39	0.68	0.24	0.68	0.45	0.11	1.07	0.46
125% Annuloplasty	0.38	0.48	0.24	0.61	0.44	0.07	0.87	0.37
True Sized Annuloplasty	0.49	0.50	0.24	0.46	0.43	0.07	0.76	0.46
Undersized Annuloplasty	0.56	0.57	0.24	0.35	0.42	0.08	0.77	0.56

<b>Experimental Condition</b>	<b>Experiment</b>						
	<b>J</b>	<b>K</b>	<b>L</b>	<b>M</b>	<b>N</b>	<b>O</b>	<b>P</b>
Control	0.81	0.83	0.01	1.05	0.49	0.22	0.82
IMR	1.34	1.34	0.02	1.14	0.62	0.34	1.73
Oversized Annuloplasty	1.05	1.19	0.03	1.13	0.57	0.26	1.39
True Sized Annuloplasty	0.79	1.10	0.04	1.08	0.57	0.25	1.14
Undersized Annuloplasty	0.63	1.11	0.06	0.83	0.51	0.23	1.18

## **APPENDIX E**

### **CATALOG OF THESIS DATA STORAGE**

#### **E.1 Specific Aim 1 Data on the Laboratory's Electronic Server**

E.1.1 Healthy animal mitral annular force data that includes processed cyclic forces at each level of left ventricular pressure:

alicia3/home/asiefert3/Thesis Data/Aim1/Healthy Animal Forces/

E.1.2 Healthy animal echocardiography data sets:

alicia3/home/asiefert3/Thesis Data/Aim1/Healthy Animal Echos/

E.1.3 IMR animal mitral annular force data that includes processed cyclic forces at each level of left ventricular pressure:

alicia3/home/asiefert3/Thesis Data/Aim1/IMR Animal Forces/

E.1.4 IMR animal echocardiography data sets:

alicia3/home/asiefert3/Thesis Data/Aim1/IMR Animal Echos/

#### **E.2 Specific Aim 2 Data on the Laboratory's Electronic Server**

E.2.1 Annuloplasty ring stress transducer study:

E.2.1.1 Annuloplasty ring stress transducer data:

alicia3/home/asiefert3/Thesis Data/Aim2/Annuloplasty Ring Stress/Data

E.2.1.2 Annuloplasty ring stress transducer echocardiography data set:

alicia3/home/asiefert3/Thesis Data/Aim2/Annuloplasty Ring Stress/Echos

E.2.2 Annuloplasty ring suture force studies:



E.2.2.1 Undersized annuloplasty ring suture force data and images:

alicia3/home/asiefert3/Thesis Data/Aim2/Annuloplasty Ring Suture  
Forces/Undersized Ring Data and Images

E.2.2.2 Undersized annuloplasty ring suture force echocardiography data sets:

alicia3/home/asiefert3/Thesis Data/Aim2/Annuloplasty Ring Suture  
Forces/Undersized Ring Echos

E.2.2.3 True-sized annuloplasty ring suture force data and images:

alicia3/home/asiefert3/Thesis Data/Aim2/Annuloplasty Ring Suture  
Forces/True Sized Ring Data and Images

E.2.2.4 True-sized annuloplasty ring suture force echocardiography data sets:

alicia3/home/asiefert3/Thesis Data/Aim2/Annuloplasty Ring Suture  
Forces/True Sized Ring Echos

### **E.3 Specific Aim 3A Data on the Laboratory's Electronic Server**

E.3.1 In-vitro data:

E.3.1.1 In-vitro data sets:

alicia3/home/asiefert3/Thesis Data/Aim3A/In Vitro Data/Data

E.3.1.2 In-vitro echocardiography data sets:

alicia3/home/asiefert3/Thesis Data/Aim3A/In Vitro Data/Echos

E.3.2 Animal data

E.3.2.1 Sonomicrometry data sets for the healthy and IMR animals:

alicia3/home/asiefert3/Thesis Data/Aim3A/Animal Data/Sonomicrometry

E.3.2.2 Echocardiography data sets for the healthy and IMR animals:

alicia3/home/asiefert3/Thesis Data/Aim3A/Animal Data/Echos

#### **E.4 Specific Aim 3B Data on the Laboratory's Electronic Server**

##### E.4.1 echocardiography data sets

alicia3/home/asiefert3/Thesis Data/Aim3B/Echos

##### E.4.2 Chordal force transducer calibrations and experimental files

alicia3/home/asiefert3/Thesis Data/Aim3B/ Chordal Force Transducer  
Calibrations and Experimental Files

##### E.4.3 Processed hemodynamic, chordal Force, and coaptation data

alicia3/home/asiefert3/Thesis Data/Aim3B/Processed Data

#### **E.5 Matlab and LabView Programs**

##### E.5.1 Suture force transducer analysis

alicia3/home/asiefert3/Thesis Data/Matlab and LabView Programs/Suture Force  
Transducer Analysis/

##### E.5.2 Suture Force Data Acquisition

alicia3/home/asiefert3/Thesis Data/Matlab and LabView Programs/Suture Force  
Data Acquisition

##### E.5.3 Chordal Force Processing

alicia3/home/asiefert3/Thesis Data/Matlab and LabView Programs/Chordal Force  
Processing

##### E.5.4 Heartbreaker Data Acquisition and Hemodynamic Post Processor

alicia3/home/asiefert3/Thesis Data/Matlab and LabView Programs/Heartbreaker

### E.5.5 Area Calculator

alicia3/home/asiefert3/Thesis Data/Matlab and LabView Programs/Area

Calculator

## **APPENDIX F**

### **CATALOG OF PUBLICATION AND CONFERENCE DATA STORAGE**

#### **F.1 Publication Documents and High Resolution Images**

##### **F.1.1 PDFs of the publications**

alicia3/home/asiefert3/Thesis Data/Publications/PDFs of Publications

##### **F.1.2 Specific Aim 1 publications**

F.1.2.1 *In Vivo* Transducer to Measure Mitral Annular Forces

alicia3/home/asiefert3/Thesis Data/Publications/Specific Aim 1/Tech Note for  
Journal of Biomechanics

F.1.2.2 Dynamic Assessment of Mitral Annular Force Profile in an Ovine Model

alicia3/home/asiefert3/Thesis Data/Publications/Specific Aim 1/Healthy  
Animals for The Annals of Thoracic Surgery

F.1.2.3 Contractile Mitral Annular Forces are Reduced in an Ovine Model of  
Ischemic Mitral Regurgitation

alicia3/home/asiefert3/Thesis Data/Publications/Specific Aim 1/ Healthy vs.  
IMR Animals Journal of Thoracic and Cardiovascular Surgery

### **F.1.3 Specific Aim 2 publications**

F.1.3.1 Suture Forces in Undersized Mitral Annuloplasty: Novel Device and Measurements

alicia3/home/asiefert3/Thesis Data/Publications/Specific Aim 2/ Ring Suture Forces Tech Note for The Annals of Thoracic Surgery

F.1.3.2 *In Vivo* Mitral Annuloplasty Ring Transducer: Implications for Implantation and Annular Downsizing.

alicia3/home/asiefert3/Thesis Data/Publications/Specific Aim 2/ Annuloplasty Ring Stress Transducer Tech Note Journal of Biomechanical Engineering

### **F.1.4 Specific Aim 3 publications**

F.1.4.1 In-Vitro Mitral Valve Simulator Mimics Systolic Valvular Function of Chronic Ischemic Mitral Regurgitation Ovine Model

alicia3/home/asiefert3/Thesis Data/Publications/Specific Aim 3/ Simulator Validation Annals of Thoracic Surgery

F.1.4.2 Quantitative Evaluation of Annuloplasty on Mitral Valve Chordae Tendineae Forces to Supplement Surgical Planning Model Development

alicia3/home/asiefert3/Thesis Data/Publications/Specific Aim 3/ Annuloplasty Undersizing Cardiovascular Engineering and Technology

### **F.1.5 Other Publications**

F.1.5.1 Isolated Effect of Geometry on Mitral Valve Function for In-Silico Model Development

alicia3/home/asiefert3/Thesis Data/Publications/Other Publications/NIH

Specific Aim 1 Computer Model Boundary Conditions

F.1.5.2 Accuracy of a Mitral Valve Segmentation Method Using J-Splines for Real-Time 3D Echocardiography Data

alicia3/home/asiefert3/Thesis Data/Publications/Other Publications/MV

Segmentation Accuracy

F.1.5.3 In-Vitro Comparison of Doppler and Catheter Measured Pressure Gradients in 3D Models of Mitral Valve Calcification

alicia3/home/asiefert3/Thesis Data/Publications/Other Publications/Mitral

Stenosis Journal Submission

F.1.5.4 Mitral Valve Annular Downsizing Forces: Implications for Annuloplasty Device Development

alicia3/home/asiefert3/Thesis Data/Publications/Other Publications/C-Ring

Annulus Downsizing

F.1.5.5 In vitro assessment of available coaptation area as a novel metric for the quantification of tricuspid valve coaptation.

alicia3/home/asiefert3/Thesis Data/Publications/Other Publications/Tricuspid

Valve Coaptation Area

## **F.2 Conference Proceedings**

### **F.2.1 Specific Aim 1 Conference Proceedings**

F.2.1.1 In-Vivo Force Measurement of the Contractile Mitral Annulus

alicia3/home/asiefert3/Thesis Data/Conference Proceedings/Specific Aim

1/2012 Mitral Conclave New York

F.2.1.2 Quantification of Dynamic Annular Forces in an Ovine model of Ischemic Mitral Regurgitation

alicia3/home/asiefert3/Thesis Data/Conference Proceedings/Specific Aim

1/2012 ACC Chicago

F.2.1.3 Novel Method to Quantify Forces with the Heart's Native Valves

alicia3/home/asiefert3/Thesis Data/Conference Proceedings/Specific Aim

1/2013 GTRIC

## **F.2.2 Specific Aim 2 Conference Proceedings**

F.2.2.1 Annuloplasty Ring Stresses: Implications for Implantation and Annulus Downsizing

alicia3/home/asiefert3/Thesis Data/Conference Proceedings/Specific Aim

2/2013 Mitral Conclave New York

F.2.2.2 Annuloplasty Suture Forces: Preliminary Insight for Identifying the Mechanisms of Ring Dehiscence

alicia3/home/asiefert3/Thesis Data/Conference Proceedings/Specific Aim

2/2014 Heart Valves in the Big Apple

## **F.2.3 Specific Aim 3 Conference Proceedings**

F.2.3.1 Mechanistic Comparison of Restrictive Annuloplasty and Adjunct Anterior Leaflet Augmentation for Ischemic Mitral Regurgitation

alicia3/home/asiefert3/Thesis Data/Conference Proceedings/Specific Aim  
3/2014 AATS Toronto

#### F.2.3.2 Isolated Effect of Geometry on Mitral Valve Function for In-Silico Model Development

alicia3/home/asiefert3/Thesis Data/Conference Proceedings/Specific Aim  
3/2013 BMES Seattle

#### F.2.3.3 Boundary Conditions for Mechanobiological Testing of Mitral Valve Leaflets

alicia3/home/asiefert3/Thesis Data/Conference Proceedings/Specific Aim  
3/2012 Biomechanics in Vascular Biology and Cardiovascular Disease

#### F.2.3.4 *In Vivo* Validation of an In Vitro Model of Ischemic Mitral Regurgitation

alicia3/home/asiefert3/Thesis Data/Conference Proceedings/Specific Aim  
3/2012 BMES Atlanta

### **F.2.4 Scanned Historical Slides**

alicia3/home/asiefert3/Thesis Data/Conference Proceedings/Scanned Historical  
Slides

### **F.2.5 Other**

#### F.2.5.1 Edwards Lifesciences Presentation

alicia3/home/asiefert3/Thesis Data/Conference Proceedings/Other/2014  
Edwards Lifesciences

#### F.2.5.2 Dr. Y's Moorehouse College Talk



alicia3/home/asiefert3/Thesis Data/Conference Proceedings/Other/2014 Dr Y  
Moorehouse Talk

F.2.5.3 Accuracy of a Mitral Valve Segmentation Method for Real-Time 3D  
Echocardiography Using Disease Mitral Valve Models

alicia3/home/asiefert3/Thesis Data/Conference Proceedings/Other/2013  
SHVD Venice Italy

F.2.5.4 Dr. Y's Isreal Mitral Talk

alicia3/home/asiefert3/Thesis Data/Conference Proceedings/Other/2012 MV  
Isreal Talk

F.2.5.5 Dr. Y's University of Texas Mitral Talk

alicia3/home/asiefert3/Thesis Data/Conference Proceedings/Other/2012 Dr Y  
University of Texas

F.2.5.6 Dr. Y's Mitral Prizker

alicia3/home/asiefert3/Thesis Data/Conference Proceedings/Other/2012 Dr Y  
Mitral Pritzker

F.2.5.7 Patient Specific Modeling of Mitral Stenosis: Isolated effect of restricted  
leaflet opening on transvalvular pressure gradient.

alicia3/home/asiefert3/Thesis Data/Conference Proceedings/Other/2012  
BMES Atlanta

## REFERENCES

### References

- [1] Carpentier A, Adams DH, Filsoofi. *Carpentier's Reconstructive Valve Surgery*, Saunders, Maryland Heights, Missouri. 2010.
- [2] Savage EB, Bolling SB. *Atlas of Mitral Valve Repair*. Lippincott Williams & Wilkins. Philadelphia, PA. 2005.
- [3] Roger VL, Go AS, Lloyd-Jones DM et al. AHA Statistical Update: Heart Disease and Stroke Statistics—2011 Update: A report from the American Heart Association. *Circulation* 2011; 123:e18-e209.
- [4] Borger MA, Alam A, Murphy PM et al. Chronic ischemic mitral regurgitation: repair, replace or rethink? *The Annals of Thoracic Surgery* 2006; 81:1153-1161.
- [5] Acker MA, Parides MK, Perrault LP et al. Mitral-valve repair versus replacement for severe ischemic mitral regurgitation. *New England Journal of Medicine* 2014; 370: 23-32.
- [6] Mirabel M, Iung B, Baron G et al. What are the characteristics of patients with severe, symptomatic, mitral regurgitation who are denied surgery? *European heart journal* 2007; 28:1358-1365.
- [7] Chiam PT, Ruiz CE. Percutaneous Transcatheter Mitral Valve Repair: A Classification of the Technology. *JACC: Cardiovascular Interventions* 2011; 4:1-13.
- [8] Mack MJ. Percutaneous treatment of mitral regurgitation: So near, yet so far! *The Journal of Thoracic and Cardiovascular Surgery* 2008; 135:237-239.
- [9] Piazza N, Asgar A, Ibrahim R et al. Transcatheter Mitral and Pulmonary Valve Therapy. *Journal of the American College of Cardiology* 2009; 53:1837-1851.
- [10] Lam Y, Lee P, Yong G et al. Investigational devices for mitral regurgitation: state of the art. *Expert Reviews Medical Devices* 2011; 8:105-114.
- [11] Aggarwal G, Schlosshan D, Mathur G et al. Recurrent Ischaemic Mitral Regurgitation Post Mitral Annuloplasty due to Suture Dehiscence Evaluated Using Real Time Three Dimensional Transoesophageal Echocardiography. *Heart, Lung and Circulation* 2012; 21:844-846.
- [12] Ghadimi K, Gosalia AR, Troianos CA. Intraoperative Delineation of Mitral Annuloplasty Dehiscence Using Three-Dimensional Transesophageal Echocardiography. *Anesthesia & Analgesia* 2011; 113:1013-1015.

- [13] Levack MM, Vergnat M, Cheung AT et al. Annuloplasty Ring Dehiscence in Ischemic Mitral Regurgitation. *The Annals of Thoracic Surgery* 2012; 94:2132.
- [14] Piatkowski R, Janusz K, Scislo P et al. Usefulness of Live/Real Time Three-Dimensional Transesophageal Echocardiography in the Assessment of Severe Mitral Annuloplasty Ring Dehiscence. *Echocardiography* 2012; 29: e80-e81.
- [15] Shapira AR, Stoddard MF, Dawn B et al. Dehiscence of Mitral Annuloplasty Ring. *Circulation* 2005; 112:e305-e305.
- [16] Kronzon I, Sugeng L, Perk G et al. Real-time 3-dimensional transesophageal echocardiography in the evaluation of post-operative mitral annuloplasty ring and prosthetic valve dehiscence. *Journal of the American College of Cardiology* 2009; 53:1543-1547.
- [17] Lange R, Guenther T, Kiefer B et al. Mitral valve repair with the new semirigid partial Colvin–Galloway Future annuloplasty band. *The Journal of Thoracic and Cardiovascular Surgery* 2008; 135:1087-1093.
- [18] Swaans MJ, Braam RL, Heijmen RH et al. Three-Dimensional Transesophageal Echocardiography in a Patient With Early Failure of Mitral Valve Repair Why Are We Still Looking at a Three-Dimensional Structure in 2 Dimensions? *Circulation: Cardiovascular Imaging* 2008; 1:282-283.
- [19] Ramakrishna H. Incidental TOE finding-Carpentier mitral annuloplasty ring dehiscence during heart transplantation. *Annals of Cardiac Anaesthesia* 2008; 11:49.
- [20] Tsang W, Wu G, Rozenberg D et al. Early mitral annuloplasty ring dehiscence with migration to the descending aorta. *Journal of the American College of Cardiology*, 2009; 54:1629-1629.
- [21] Gillinov AM, Cosgrove III DM, Shiota T et al. Cosgrove-Edwards annuloplasty system: midterm results. *The Annals of Thoracic Surgery* 2000; 69:717-721.
- [22] Cerfolio RJ, Orszulak TA, Pluth JR et al. Reoperation after valve repair for mitral regurgitation: early and intermediate results. *The Journal of Thoracic and Cardiovascular Surgery* 1996; 111:1177-1184.
- [23] Bax JJ, Braun J, Somer ST et al. Restrictive Annuloplasty and Coronary Revascularization in Ischemic Mitral Regurgitation Results in Reverse Left Ventricular Remodeling. *Circulation* 2004; 110:II-103-II-108.

- [24] Braun J, van de Veire NR, Klautz RJM et al. Restrictive mitral annuloplasty cures ischemic mitral regurgitation and heart failure. *The Annals of Thoracic Surgery* 2008; 85:430-437.
- [25] Geidel S, Lass M, Schneider C et al. Downsizing of the mitral valve and coronary revascularization in severe ischemic mitral regurgitation results in reverse left ventricular and left atrial remodeling. *European Journal of Cardiothoracic Surgery* 2005; 129:860-68.
- [26] McGee EC, Gillinov AM, Blackstone EH. Recurrent mitral regurgitation after annuloplasty for functional ischemic mitral regurgitation. *The Journal of Thoracic and Cardiovascular Surgery* 2004; 128:916-924.
- [27] Hung J, Papakostas L, Tahta SA. Mechanism of recurrent ischemic mitral regurgitation after annuloplasty: continued LV remodeling as a moving target. *Circulation* 2004; 110: II85-II90.
- [28] Kuwahara E, Otsuji Y, Iguro Y et al. Mechanism of Recurrent/Persistent Ischemic/Functional Mitral Regurgitation in the Chronic Phase after Surgical Annuloplasty. *Circulation* 2006; 114:I-229-I-534.
- [29] Zhu F, Otsuji Y, Yotsumoto G. Mechanism of recurrent ischemic mitral regurgitation after annuloplasty: importance of augmented posterior mitral leaflet tethering. *Circulation* 2005; 112:I396-401.
- [30] Ormiston JA, Shah PM, Tei CHUWA et al. (1981). Size and motion of the mitral valve annulus in man. I. A two-dimensional echocardiographic method and findings in normal subjects. *Circulation* 1981; 64:113-120.
- [31] Tibayan FA, Rodriguez F, Langer F et al. Annular Remodeling in Chronic Ischemic Mitral Regurgitation: Ring Selection Implications. *The Annals of Thoracic Surgery* 2003; 76:1549-1555.
- [32] Levine RA, Handschumacher MD, Sanfilippo AJ et al. Three-Dimensional Echocardiographic Reconstruction of the Mitral Valve, with Implications for the Diagnosis of Mitral Valve Prolapse. *Circulation* 1989; 80:589-598.
- [33] Gorman III JH, Jackson BM, Enomoto Y et al. The Effect of Regional Ischemia on Mitral Valve Annular Saddle Shape. *The Annals of Thoracic Surgery* 2004; 77:544-548.
- [34] Ryan LP, Jackson BM, Hamamoto H et al. The Influence of Annuloplasty Ring Geometry on Mitral Leaflet Curvature. *The Annals of Thoracic Surgery* 2008; 86:749-760.

- [35] Komoda T, Hetzer R, Oellinger J et al Mitral Annular Flexibility. *Journal of Cardiac Surgery* 2007; 12:102-109.
- [36] Itoh A, Ennis DB, Bothe W et al. Mitral Annular Hinge Motion Contribution to Changes in Mitral Septal-Lateral Dimension and Annular Area. *The Journal of Thoracic and Cardiovascular Surgery* 2009; 138:1090-1099.
- [37] Kaplan Sr. BG, Gaddipatti A. Three-Dimensional Echocardiographic Assessment of Annular Shape Changes in the Normal and Regurgitant Valve. *American Heart Journal* 2000; 139:378-387.
- [38] Timek TA, Green GR, Tibayan FA et al. Aorto-Mitral Annular Dynamics. *The Annals of Thoracic Surgery* 2003; 76:1944-1950.
- [39] Mitral Valve Leaflets. N.d. Photograph. Medscape, Washington. Web. 10 Mar 2014. <<http://emedicine.medscape.com/article/1878301-overview>>
- [40] Annular Saddle. N.d. Photograph. Cardiovascular Research and Training Center, Washington. Web. 10 Mar 2014. <<http://depts.washington.edu/cvrtc/apples.html>>.
- [41] Gorman III JH, Gorman RC, Jackson BM et al. Annuloplasty Ring Selection for Chronic Ischemic Mitral Regurgitation: Lessons from the Ovine Model. *The Annals of Thoracic Surgery* 2003; 76:1556-1563.
- [42] Salgo IS, Gorman III JH, Gorman RC et al. Effect of Annular Shape on Leaflet Curvature in Reducing Mitral Leaflet Stress. *Circulation* 2002; 106:711-717.
- [43] Jimenez JH, Liou SW, Padala M et al. A Saddle-Shaped Annulus Reduces Systolic Strain on the Central Region of the Mitral Valve Anterior Leaflet. *The Journal of Thoracic and Cardiovascular Surgery* 2007; 134:1562-1568.
- [44] Padala M, Hutchison RA, Croft LR et al. Saddle Shape of the Mitral Annulus Reduces Systolic Strains on the P2 Segment of the Posterior Mitral Leaflet. *The Annals of Thoracic Surgery* 2009; 88:1499-1504.
- [45] Jimenez JH, Soerensen DD, He Z et al. Effects of a Saddle Shaped Annulus on Mitral Valve Function and Chordal Force Distribution: An in Vitro Study. *Annals of Biomedical Engineering* 2003; 31:1171-1181.
- [46] Rausch MK, Bothe W, Kvitting JP et al. Characterization of Mitral Valve Annular Dynamics in the Beating Heart. *Annals of Biomedical Engineering* 2011; 39:1690-1702.

- [47] Gorman III JH, Moainie SL, Enomoto Y et al. Influence of Inotropy and Chronotropy on the Mitral Valve Sphincter Mechanism. *The Annals of Thoracic Surgery* 2004; 77:852-858.
- [48] Gorman III JH, Gorman RC, Jackson BM et al. Distortions of the Mitral Valve in Acute Ischemic Mitral Regurgitation. *The Annals of Thoracic Surgery* 1997; 64:1026-1031.
- [49] Madu EC, Baugh D, D’Cruz IA et al. Left Ventricular Papillary Muscle Morphology and Function in Left Ventricular Hypertrophy and Left Ventricular Dysfunction. *Medical science monitor: international medical journal of experimental and clinical research* 2001; 7:1212-1218.
- [50] Joudinaud TM, Kegel CL, Flecher EM et al. The Papillary Muscles as Shock Absorbers of the Mitral Valve Complex: An Experimental Study. *European journal of cardiothoracic surgery* 2007; 32:96-101.
- [51] Rabbah JPM, Saikrishnan N, Siefert, AW et al. Mechanics of healthy and functionally diseased mitral valves: a critical review. *Journal of Biomechanical Engineering* 2013; 135:1-16.
- [52] Badiwala MV, Verma S, Rao V. Surgical Management of Ischemic Mitral Regurgitation. *Circulation* 2009; 120:1287-1293.
- [53] Lung B. Management of ischaemic mitral regurgitation. *Heart* 2003; 89:459-464.
- [54] Gorman RC, Gorman III JH, Edmunds Jr H. Ischemic Mitral Regurgitation, in Cardiac surgery in the adult, L.H. Cohn and J. L. Henry Edmunds, Editors. McGraw-Hill: New York, NY, 2003, pp. 751-769
- [55] Tibayan FA, Rodriguez F, Zasio MK et al. Geometric Distortions of the Mitral Valvular-Ventricular Complex in Chronic Ischemic Mitral Regurgitation. *Circulation* 2003; 108:II-116-II-121.
- [56] Badhwar V, Bolling SF. Nontransplant surgical options for heart failure. Cardiac surgery in the adult. New York: McGraw-Hill, 1515-26, 2003
- [57] Kumanohoso T, Otsuji Y, Yoshifuku S et al. Mechanism of higher incidence of ischemic mitral regurgitation in patients with inferior myocardial infarction: Quantitative analysis of left ventricular and mitral valve geometry in 103 patients with prior myocardial infarction. *The Journal of Thoracic and Cardiovascular Surgery* 2003; 125:135-143.
- [58] Gillinov AM, Wierup PN, Blackstone EH et al. Is repair preferable to replacement for ischemic mitral regurgitation? *The Journal of Thoracic and Cardiovascular Surgery* 2001; 122:1125-1141.

- [59] Hickey MS, Smith LR, Muhlbaier LH et al. Current prognosis of ischemic mitral regurgitation. Implications for future management. *Circulation* 1988; 78(3 Pt 2):I51–I59.
- [60] Vergnat M, Jassar AS, Jackson BM et al. Ischemic mitral regurgitation: a quantitative three-dimensional echocardiographic analysis. *The Annals of Thoracic Surgery* 2011; 91:157-164.
- [61] Veronesi, F, Corsi C, Sugeng L et al. Quantification of mitral apparatus dynamics in functional and ischemic mitral regurgitation using real-time 3-dimensional echocardiography. *Journal of the American Society of Echocardiography* 2008; 21:347-354.
- [62] Langer F, Rodriguez F, Ortiz S et al. Subvalvular Repair The Key to Repairing Ischemic Mitral Regurgitation? *Circulation* 2005; 112:I-383-I-389.
- [63] Siefert AW, JPM Rabbah, Koomalsingh KJ et al. In-Vitro Mitral Valve Simulator Mimics Systolic Valvular Function of Chronic Ischemic Mitral Regurgitation Ovine Model. *The Annals of Thoracic Surgery* 2013; 95:824-829.
- [64] Fedak PWM, McCarthy PM, Bonow RO. Evolving Concepts and Technologies in Mitral Valve Repair. *Circulation* 2008; 117:963-974.
- [65] Grossi EA, Patel N, Woo YJ et al. Outcomes of the RESTOR-MV Trial (Randomized Evaluation of a Surgical Treatment for Off-Pump Repair of the Mitral Valve). *Journal of the American College of Cardiology* 2010; 56:1984-1993.
- [66] Acker MA, Jessup M, Bolling SF et al. Mitral valve repair in heart failure: Five-year follow-up from the mitral valve replacement stratum of the Acorn randomized trial. *Journal of Thoracic and Cardiovascular Surgery* 2011; 142:569-574.
- [67] Cheung A, Webb JG, Wong DR et al. Transapical Transcatheter Mitral Valve-in-Valve Implantation in a Human. *The Annals of Thoracic Surgery* 2009; 87:e18-e20.
- [68] Shofer J, Siminiak T, Haude M et al. Percutaneous Mitral Annuloplasty for Functional Mitral Regurgitation: Results of the CARILLON Mitral Annuloplasty Device European Union Study. *Circulation* 2009; 120:326-333.
- [69] Webb JG, Harnek J, Munt BI et al. Percutaneous Transvenous Mitral Annuloplasty: Initial Human Experience with Device Implantation in the Coronary Sinus. *Circulation* 2006; 113:851-855.

- [70] Harnek J, Webb JG, Kuck, KH et al. Transcatheter Implantation of the MONARC Coronary Sinus Device for Mitral Regurgitation: 1-Year Results From the EVOLUTION Phase I Study (Clinical Evaluation of the Edwards Lifesciences Percutaneous Mitral Annuloplasty System for The Treatment of Mitral Regurgitation). *Journal of the American College of Cardiology* 2011; 4:115-122.
- [71] Purser MF, Richards AL, Cook RC et al. A Novel Shape Memory Alloy Annuloplasty Ring for Minimally Invasive Surgery: Design, Fabrication, and Evaluation. *Annals of Biomedical Engineering* 2010; 39:367-377.
- [72] Jensen H, Simpanen J, Smerup M et al. Medtentia Double Helix Mitral Annuloplasty System Evaluated in a Porcine Experimental Model. *Innovations: Technology and Techniques in Cardiothoracic and Vascular Surgery* 2010; 5:114–117.
- [73] Webb JG, Wood DA, Ye J et al. Transcatheter Valve-in-Valve Implantation for Failed Bioprosthetic Heart Valves. *Circulation* 2010; 121:1848-1857.
- [74] Suri RM, Schaff HV. Reoperation Following Mitral Valve Repair in Redo Cardiac Surgery in Adults 2nd Edition, Editors Machiraju VR, Schaff HV, Svensson LG. 2012.Spring New York Dordrecht Heidelberg London.
- [75] Hasenkam JM, Nygaard H, Paulsen PK et al. What force can the myocardium generate on a prosthetic mitral valve ring? An animal experimental study. *Journal of Heart Valve Disease* 1994; 3:324-329.
- [76] Shandas R, Mitchell M, Conrad C et al. A general method for estimating deformation and forces imposed in vivo on bioprosthetic heart valves with flexible annuli: in vitro and animal validation studies. *Journal of Heart Valve Disease* 2001; 10:495-504.
- [77] Edwards MB, Draper ERC, Hand JW et al. Mechanical testing of human cardiac tissue: some implications for MRI safety. *Journal of Cardiovascular Magnetic Resonance* 2005; 7:835-840.
- [78] Spratt JR, Spratt JA, Beachley V et al. Strength comparison of mitral annuloplasty ring and suturing combinations: an in-vitro study. *The Journal of Heart Valve Disease* 2012; 21:286-292.
- [79] Robb JD, Minakawa M, Koomalsingh KJ et al., Posterior leaflet augmentation improves leaflet tethering in repair of ischemic mitral regurgitation. *European Journal of Cardio-thoracic surgery* 2011; 40:1501-1507.
- [80] Rama A, Praschker L, Barreda E et al. Papillary muscle approximation for functional ischemic mitral regurgitation. *The Annals of Thoracic Surgery* 2007; 84:2130-2131.



- [81] Hvass U, Tapia M, Baron F et al. Papillary muscle sling: a new functional approach to mitral repair in patients with ischemic left ventricular dysfunction and functional mitral regurgitation. *The Annals of Thoracic Surgery* 2003; 75:809-811
- [82] Liel-Cohen N, Guerrero JL, Otsuji Y et al. Design of a new surgical approach for ventricular remodeling to relieve ischemic mitral regurgitation: insights from 3-dimensional echocardiography. *Circulation* 2000; 101:2756-2763.
- [83] Ramadan R, Al-Attar N, Mohammadi S et al. Left ventricular infarct plication restores mitral function in chronic ischemic mitral regurgitation. *Journal of Thoracic and Cardiovascular Surgery* 2005; 129:440-442.
- [84] Langer F, Rodriguez F, Cheng A et al., Posterior mitral leaflet extension: an adjunctive repair option for ischemic mitral regurgitation? *Journal of Thoracic and Cardiovascular Surgery* 2006; 131:868-877.
- [85] de Varennes B, Chaturvedi R, Sidhu S et al. Initial results of posterior leaflet extension for severe type IIIb ischemic mitral regurgitation. *Circulation* 2009; 119:2837-2843.
- [86] Fattouch K, Lancellotti P, Castrovinci S et al. Papillary muscle relocation in conjunction with valve annuloplasty improve repair results in severe ischemic mitral regurgitation. *Journal of Thoracic and Cardiovascular Surgery* 2012; 143:1352-1355.
- [87] Braun J, Klautz JM. Mitral valve surgery in low ejection fraction, severe ischemic mitral regurgitation patients: should we repair them all? *Current Opinions in Cardiology* 2012; 27:111-117.
- [88] Ciarka A, Braun J, Delgado V et al. Predictors of mitral regurgitation recurrence in patients with heart failure undergoing mitral valve annuloplasty. *The American Journal of Cardiology* 2010; 106:395-401.
- [89] Mange J, Pibarot P, Dagenais F et al. Preoperative posterior leaflet angle accurately predicts outcome after restrictive mitral annuloplasty for ischemic mitral regurgitation. *Circulation* 2007; 115:782-791.
- [90] Lee A, Acker M, Kubo S et al. Mechanisms of recurrent functional mitral regurgitation after mitral valve repair in non-ischemic dilated cardiomyopathy: importance of distal anterior leaflet tethering. *Circulation* 2009; 119:2606-2614.
- [91] Buckley O, Di Carli M. Predicting benefit from revascularization in patients with ischemic heart failure: imaging of myocardial ischemia and viability. *Circulation* 2011; 123:444-450.

- [92] Burlina P, Sprouse C, Mukherjee R et al. Patient-Specific Mitral Valve Closure Prediction Using 3D Echocardiography. *Ultrasound in Medicine & Biology* 2013; 39:769-783.
- [93] Ionasec RI, Voigt I, Georgescu B et al. Patient specific modeling and quantification of the aortic and mitral valves from 4D cardiac CT and TEE. *IEEE Transactions on medical imaging* 2010. 29:1636-1651.
- [94] Lau KD, Diaz V, Scrambler P et al. Mitral valve dynamics in structural and fluid-structure interaction models. *Medical Engineering Physics* 2010; 32:1057-1064.
- [95] Mansi T, Voight I, Mengue A et al. Towards Patient-Specific Finite-Element Simulation of MitraClip Procedure. *Medical Image and Computer-Assisted Intervention-MICCAI* 2011; 14:452-459.
- [96] Pouch AM, Xu C, Yushkevich PA et al. Semi-automated mitral valve morphometry and computational stress analysis using 3D ultrasound. *Journal of Biomechanics* 2012; 45:903-907.
- [97] Rim Y, McPherson DD, Chandran KB et al. The effect of patient-specific annular motion on dynamic simulation of mitral valve function. *Journal of Biomechanics* 2013; 46:1104-1112.
- [98] Stevanella MF, Maffessanti CA, Conti E et al. Mitral valve patient specific finite element modeling from cardiac MRI: application to an annuloplasty procedure. *Cardiovascular Engineering and Technology* 2011; 2:66-76.
- [99] Votta E, Arnoldi A, Invernizzi A et al. Mitral valve patient-specific finite element modeling. *MICCAI Workshop on Cardiovascular Interventional Imaging and Biophysical Modeling* 2009, London: Royaume-Uni.
- [100] Wenk JF, Zhang Z, Cheng G et al. First finite element model of the left ventricle with mitral valve: insights into ischemic mitral regurgitation. *The Annals of Thoracic Surgery* 2010; 89:1546-1553.
- [101] Wang Q, Sun W. Finite element modeling of mitral valve dynamic deformation using patient-specific multi-slices computed tomography scans. *Annals of Biomedical Engineering* 2013; 41: 142-153.
- [102] Hammer PE, Vasilyev NV, Perrin DP et al. Fast image-based model of mitral valve closure for surgical planning. *MIDAS Journal, Computational Biomechanics for Medicine (MICCAI 2008 Workshop)*: 15-26.
- [103] Jensen MØ, Fontaine AA, Yoganathan AP. Improved In Vitro Quantification of the Force Exerted by the Papillary Muscle on the Left Ventricular Wall: Three-

- Dimensional Force Vector Measurement System. *Annals of Biomedical Engineering* 2001; 29: 406-413.
- [104] Jimenez JH, Soerensen DD, He Z et al., Effects of Papillary Muscle Position on Chordal Force Distribution: an in-vitro study. *The Journal of Heart Valve Disease* 2005; 14:295-302.
- [105] Jimenez JH, Soerensen DD, He Z et al. Mitral Valve Function and Chordal Force Distribution Using a Flexible Annulus Model: An In Vitro Study. *The Annals of Biomedical Engineering* 2005; 33: 557-566.
- [106] Jimenez JH, Soerensen DD, He Z et al., Effects of a Saddle Shaped Annulus on Mitral Valve Function and Chordal Force Distribution: An In-Vitro Study. *Annals of Biomedical Engineering* 2003; 31:1171-1181.
- [107] Nielsen SL, Nygaard H, Mandrup L et al., Mechanism of Incomplete Mitral Leaflet Coaptation-Interaction of Chordal Restraint and Changes in Mitral Leaflet Coaptation Geometry Insight from In Vitro Validation of the Premise of Force Equilibrium. *Journal of Biomechanical Engineering* 2002; 124:596-608.
- [108] Nielsen SL, Nygaard H, Fontaine AA et al. Chordal force distribution determines systolic mitral leaflet configuration and severity of functional mitral regurgitation. *Journal of the American College of Cardiology* 1999; 33: 843-853.
- [109] He S, Fontaine AA, Schwammenthal E et al. Integrated Mechanism for Functional Mitral Regurgitation : Leaflet Restriction Versus Coapting Force: In Vitro Studies. *Circulation* 1997; 96:1826-1834.
- [110] He S, Lemmon JD, Weston MW et al. Mitral Valve Compensation for Annular Dilation: In Vitro Study into the Mechanisms of Functional Mitral Regurgitation with an Adjustable Annulus Model. *The Journal of Heart Valve Disease* 1999; 8:294-302.
- [111] He S, Jimenez JH, He Z et al. Mitral Leaflet Geometry Perturbations with Papillary Muscle Displacement and Annular Dilation: an In-Vitro Study of Ischemic Mitral Regurgitation. *The Journal of Heart Valve Disease* 2003. 12:300-307.
- [112] Nielsen SL, Nygaard H, Fontaine AA et al., Papillary Muscle Misalignment Causes Mitral Regurgitant Jets: an Ambiguous Mechanisms for Functional Mitral Regurgitation. *The Journal of Heart Valve Disease* 1999; 8:551-564.
- [113] Padala M, Hutchison RA, Croft LR et al., Saddle Shape of the Mitral Annulus Reduces Systolic Strains on the P2 Segment of the Posterior Mitral Leaflet. *The Annals of Thoracic Surgery* 2009; 88: 1499-1504.

- [114] Jimenez JH, Liou SW, Padala M et al. A saddle-shaped annulus reduces systolic strain on the central region of the mitral valve anterior leaflet, *Journal of Thoracic Cardiovascular Surgery* 2007; 134:1562-1568.
- [115] He Z, Ritchie J, Grashow JS et al. In-Vitro Dynamic Strain Behavior of the Mitral Valve Posterior Leaflet. *Journal of Biomechanical Engineering* 2005; 127:504-511.
- [116] Marzan GT. 1975. A computer program for direct linear transformation solution of the collinearity condition and some applications of it. Proceedings of the Symposium on Close-range Photogrammetric Systems. 1:420-476.
- [117] Mitral valve replacement. N.d. Photograph. Heart Valve Surgery.comWeb. 10 Mar 2014. <<http://www.heart-valve-surgery.com/heart-surgery-blog/2010/05/10/calcified-mitral-valve-stenosis-replacement-picture/>>.
- [118] Jensen MO, Jensen H, Nielsen SL et al. What forces act on a flat rigid mitral annuloplasty ring? *Journal of Heart Valve Disease* 2008; 17:267-275.
- [119] Jensen MO, Jensen H, Smerup M et al. Saddle-shaped mitral valve annuloplasty rings experience lower forces compared with flat rings. *Circulation* 2008; 118:S250-S255.
- [120] Window AL. Strain Gage Technology 2nd Ed. Essex, England :Springer, 1989.
- [121] Jensen H, Jensen MO, Smerup MH et al. Does down-sized ring annuloplasty induce papillary muscle relocation in ischemic mitral regurgitation? *Journal of Heart Valve Disease* 2010; 19:692-700.
- [122] Rausch MK, Tibayan FA, Miller DC et al. Evidence of adaptive mitral leaflet growth. *Journal of the Mechanical Behavior of Biomedical Materials* 2012; 15:208-217.
- [123] Dal-Bianco JP, Aikawa E, Bischoff J et al. Active adaptation of the tethered mitral valve: insights into a compensatory mechanism for functional mitral regurgitation. *Circulation* 2009; 120:334-342.
- [124] Jensen MO, Hønge JL, Benediktsson JA et al. Mitral Valve Annular Downsizing Forces: Implications for Annuloplasty Device Development. *Journal of Thoracic and Cardiovascular Surgery* 2013; DOI: 10.1016/j.jtcvs.2013.07.045.
- [125] Edmunds LH Jr, Gorman JH III, Gorman RC. Sheep models of postinfarction left ventricular remodeling, In Singal PK, Dixon IMC, Kirschenbaum LA, Dhalla NS (eds.). *Cardiac Remodeling and Failure*. Boston, MA, Kluwer Academic Publishers, 2003.

- [126] Gorman JH III, Gorman RC, Plappert T et al. Infarct size and location determine development of mitral regurgitation in the sheep model. *Journal of Thoracic and Cardiovascular Surgery* 1998; 115: 615-622.
- [127] Llaneras MR, Nance ML, Streicher JT et al. Large animal model of ischemic mitral regurgitation. *The Annals of Thoracic Surgery* 1994; 57:432-439.
- [128] Draft Guidance for Industry and FDA Staff: Heart Valves—Investigational Device Exemption (IDE) and Premarket Approval (PMA) Applications, Submitted for Comment, January 20, 2010
- [129] Draft International Standard ISO 5840-3, Cardiovascular implants—Cardiac valve prostheses—Part 3: Heart valve substitutes implanted by minimally invasive techniques, 2011.
- [130] Aguel F, Hillebrenner M, Stewart SF et al. U.S. Regulatory Considerations for Heart Valves Implantation by Minimally Invasive Surgery. *Cardiovascular Engineering and Technology* 2011; 2:62-65.
- [131] Siefert AW, Jimenez JH, Koomalsingh KJ, et al. Dynamic Assessment of Mitral Annular Force Profile in an Ovine Model. *The Annals of Thoracic Surgery* 2012; 94:58-64.
- [132] Guy IV TS, Moainie SL, Gorman JH III et al. Prevention of ischemic mitral regurgitation does not influence the outcome of remodeling after posterolateral myocardial infarction. *Journal of the American College of Cardiology* 2004; 43:377-383.
- [133] Yiu SF, Enriquez-Serano M, Tribouilloy et al. Determinants of the degree of functional mitral regurgitation in patients with systolic left ventricular dysfunction. *Circulation* 2000; 102:1400-1406.
- [134] Rausch MK, Bothe WA, Escobar Kvitting JP et al. Quantitative clinical and mechanical comparison of different annuloplasty devices. *Annals of Biomedical Engineering* 2012; 40:750-761.
- [135] Wappler F, Rossaint R, Baumert J et al. Multicenter randomized comparison of Xenon and Isoflurane on left ventricular function in patients undergoing elective surgery. *Anesthesiology* 2007; 106:463-471.
- [136] Nielsen SL, Hansen SB, Nielsen H et al. Imbalanced chordal force distribution causes acute ischemic mitral regurgitation: Mechanistic insights from chordae tendineae force measurements in pigs. *Journal of Thoracic and Cardiovascular Surgery* 2005; 129:525-531.

- [137] Granier M, Jensen MO, Hong JL et al. Consequences of Mitral Valve Prolapse on Chordal Tension: Ex Vivo and in Vivo Studies in Large Animal Models. *The Journal of Thoracic and Cardiovascular Surgery* 2011; 142:1585-1587.
- [138] Bolling SF, Pagani FD, Deeb GM et al. Intermediate-term outcome of mitral reconstruction in cardiomyopathy. *The Journal of Thoracic and Cardiovascular Surgery* 1998; 115:381-388.